INAUGURAL - DISSERTATION

zur

Erlangung der Doktorwürde

der

Naturwissenschaftlich-Mathematischen

Gesamtfakultät

der

Ruprecht-Karls-Universität

Heidelberg

Vorgelegt von

Dipl.-Chem. Alexander Körner

geboren in Speyer, Deutschland

Tag der mündlichen Prüfung: 13. Dezember 2013

Functionalization and Characterization of Cell Membrane Models towards Controlling Cell Differentiation in Pluripotent Tissue Explants

Gutachter: Prof. Dr. Motomu Tanaka

apl. Prof. Dr. Reiner Dahint

Summary

The major aim of this thesis is to create a novel *in vitro* model substrate for the controlled cell differentiation in pluripotent tissue sheets by fine-tuning the balance between cell-cell (in plane) and cell-matrix (out of plane) interactions. As the model substrate to culture tissue explants, planar lipid membranes deposited on solid substrates (supported membranes) were functionalized with the extracellular domain of *Xenopus* cadherin-11 (Xcad-11), expressed in embryos during the neural crest cell (NCC) differentiation. In Chapter 4, the quantitative functionalization of supported membranes with Xcad-11 was confirmed by the combination of specular X-ray reflectivity (XRR), grazing incidence X-ray fluorescence (GIXF), and quartz crystal microbalance with dissipation (QCM-D). In Chapter 5, "animal cap" tissue sheets isolated from blastula stage embryos of *Xenopus laevis* were placed on membranes functionalized with Xcad-11. Interactions of the isolated tissue sheets with membranes displaying Xcad-11 were investigated by the combination of reflection interference contrast microscopy (RICM) and fluorescence microscopy. The capability of such a model system to induce the NCC differentiation was demonstrated by detecting the activation of the NCC marker gene *slug* by enhanced green fluorescent signal of the fusion protein. In Chapter 6, the two opposite concentration gradients of two recombinant proteins was established by means of "membrane electrophoresis", utilizing the fluidic nature of supported membranes. This allows for the creation of one-dimensional gradients of morphogens (e.g. Wnt and BMP) on supported membranes, which can guide the development of three-dimensional tissues in vitro. The obtained results demonstrated a large potential of supported membranes for controlling the fate of multicellular tissues.

Zusammenfassung

Das Ziel dieser Arbeit war es ein neuartiges *in vitro* Model zu entwickeln, welches in der Lage ist, durch die präzise Einstellung der Zell-Zell und Zell-Matrix Wechselwirkungen, die kontrollierte Zelldifferenzierung in pluripotenten Gewebeschichten zu steuern. Als Oberflächenmodell für die Kultivierung von Gewebeexplantaten wurden planare Lipidmembranen auf feste Substrate platziert. Diese sogenannten Festkörper-gestützten Lipidmembranen wurden mittels der extrazellulären Domäne von Xenopus cadherin-11 (Xcad-11), das im Froschembryo während der Differenzierung von Neuralleistenzellen exprimiert wird, funktionalisiert. Im 4. Kapitel wurde durch die Kombination von spekularer Röntgenstreuung (XRR), Röntgenfluoreszenz mit streiffendem Einfall (GIXF) und Quartzkristall-Mikrowaage mit Dissipationsmessung (QCM-D) die quantitative Funktionalisierung der Festkörper-gestützen Lipidmembranen mit Xcad-11 charakterisiert. Im 5. Kapitel wurden sogenannte “animale Kappen” (Gewebeschichten aus dem Embryo des afrikanischen Krallenfrosch (*Xenopus leavis*)) auf den Xcad-11 funktionalisierten Membranen platziert. Die Wechselwirkungen der isolierten Gewebeschicht mit solchen Membranen wird durch die kombinierte Anwendung von Reflektions-Interferenz-Kontrast Mikroskopie (RICM) und Fluoreszenz Mikroskopie untersucht. Die Induktion der Differenzierung von Neuralleistenzellen durch solch ein Modellsystem konnte mit Hilfe der Expression des Fusionsproteins Slug-GFP, ein Indikator der Neuralleistenzell-Differenzierung, dargestellt werden. Im 6. Kapitel wurde unter Anwendung der Membranelektrophorese ein Model, bestehend aus zwei gegensätzlich gerichteten Konzentrationsgradienten zweier rekombinanter Proteine, gebildet. Dies erlaubt die Bildung eindimensionaler Morphogengradienten (z.B. Wnt und BMP) auf Festkörper-gestützen Membranen, die letztlich zur Entwicklung dreidimensionaler Gewebe *in vitro* führen kann. Die hier dargestellten Ergebnisse zeigen eindeutig das großartige Potential Festkörper-gestützer Lipidmembranen um die Zell-Differenzierung in mehrzelligen Organismen zu regulieren.

Acknowledgments

I would like to thank…

Prof. Motomu Tanaka for giving me the possibility to work in his group, all his helpful ideas and his guidance throughout my thesis,

Apl. Prof. Reiner Dahint for kindly refereeing this thesis,

Prof. Doris Wedlich, **Dr. Christina Deichmann** and **Dr. Almuth Köhler** for the fruiful cooperation and the contribution to the biological part,

Dr. Oleg Konovalov and **Dr. Alexei Vorobiev** for their guidance during scattering experiments,

Dr. Fernanda Rossetti and **Wasim Abuillan** for continous scientific exchange and discussions,

Dr. Stefan Kaufmann, **Dr. Cornelia Monzel**, **Dr. Emanuel Schneck**, **Dr. Ali Makky**, **Mariam Veschgini** and **Florian Gebert** for suffering through proofreading,

Hao Zang and **Vasha Liluashvili** for their contributions to membrane electrophoresis,

Dr. Timo Maier and **Sebastian Rausch** for guiding me through my first steps of photolithography,

Dr. Thomas Kaindl, **Dr. Hiroshi Yoshikawa**, **Alexandra Burk**, **Agatha Korytowski**, **Harden Rieger**, **Nataliya Frenkel**, **Victoria Frank**, **Rami Mandow**, **Akihisa Yamamoto**, **Moritz Herrmann** and **Shigeto Inoue** for the enrichment of my everyday lab life in Heidelberg or at beamtimes in Grenoble.

Heidelberg Academy of Sciences for their financial support within the WIN-Kolleg project "Formgebung in der Biologie".

Zuletzt möchte ich meiner Familie, meinen Eltern, meinen Geschwistern und vor allem meiner Frau Angela danken, die mich jederzeit liebevoll unterstützten.

Table of contents

1. Introduction

Development of multicellular organisms in biological systems includes a multitude of processes. How do different cells determine their fate to differentiate into certain cell types? How do cells establish orientational orders into complex, structured organs, such as hearts and livers? One of the key processes in the development of vertebrates is the change in cell polarity that results in the formation of three-dimensional structures from planar cell sheets. A prominent example of such a process, often described as "a symmetry break", is the neural crest cell (NCC) differentiation that occurs in the embryonic ectoderm. NCCs are migratory, multipotent cells which give rise to different cell lineages including craniofacial cartilage, smooth muscle, peripheral and enteric neurons and glia.[1] From the mechanistic point of view, such changes in cell polarity should be driven by the dynamic balance between cell-matrix (out of plane) and cell-cell (in plane) interactions.

To date, connective tissue sheets explanted from embryos of *Xenopus laevis* (South African clawed frog), so-called animal caps, have been used as animal model systems, to follow the NCC development in vertebrates due to their amenability to experimental manipulations.[2,3]

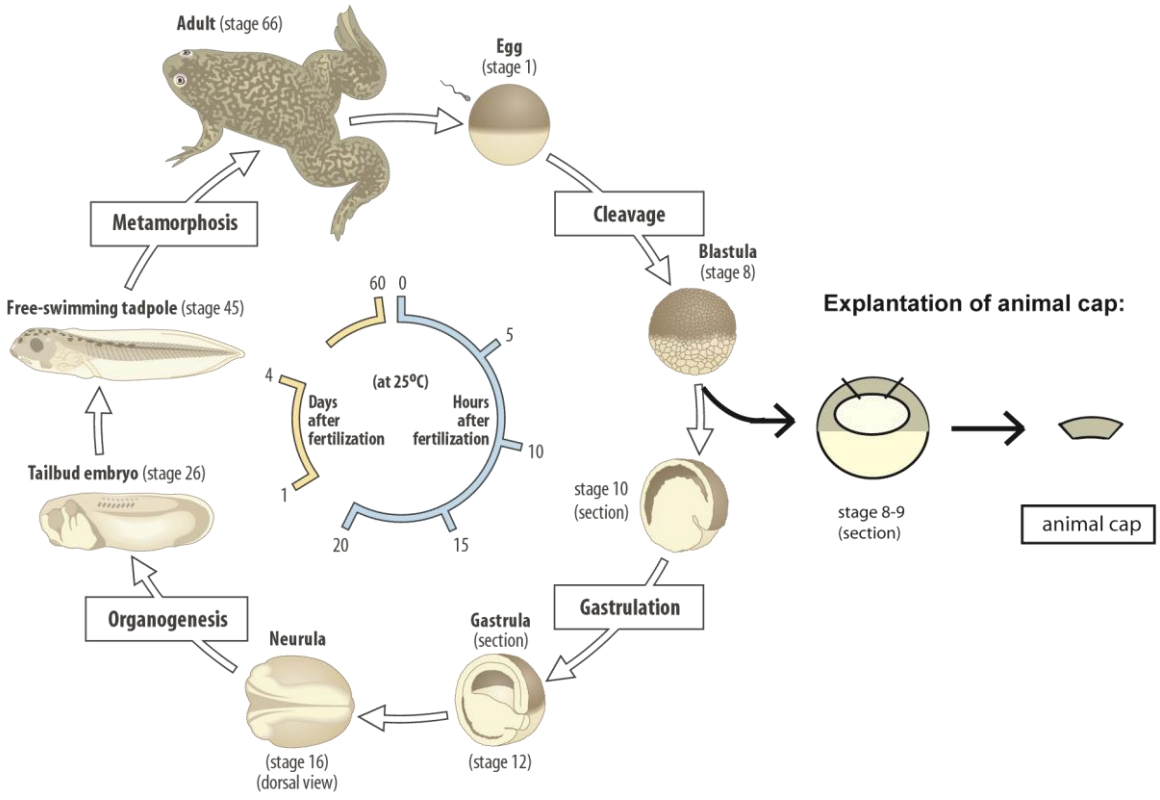

Fig. 1-1: Schematic illustration of the different developmental stages of *Xenopus* laevis and the explantation of the animal cap.[4]

An animal cap, explanted from the blastocoel roof at the early blastula stage (Fig. 1-1), is destined to form the neural system and skin. Interestingly, these explants can be diverted from their epidermal fate to others by (a) juxtaposition with other tissues, (b) addition of soluble growth factors to the medium, or (c) by pre-injecting the embryo with RNA or DNA encoding developmental active genes.[5] In this sense, the cohesive cell sheet of the animal cap exhibits pluripotency and can be forced to differentiate to NCCs, which finally segregate out of the neuroectodermal tissue (Fig. 1-2).[6]

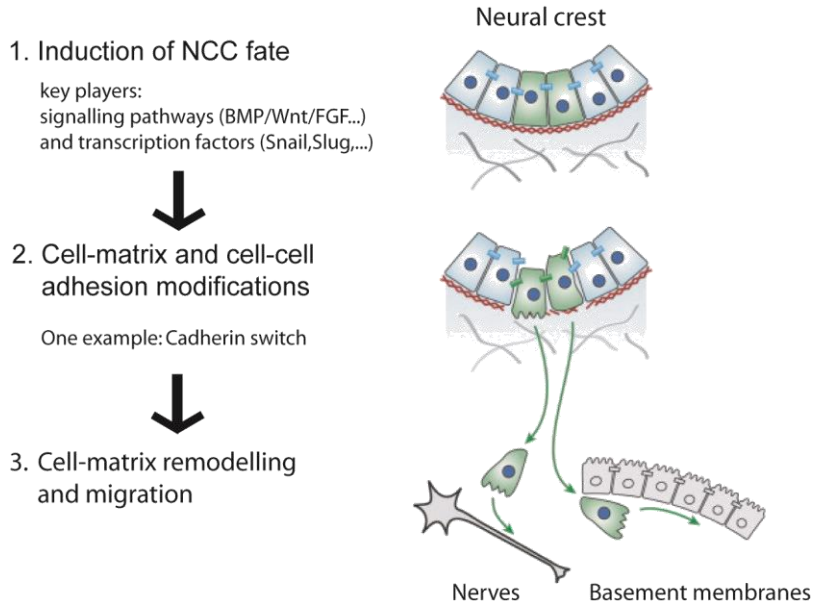

Fig. 1-2: Illustration of the NCC fate induction and migration. The figure was taken from Thevenau et al.[7] and modified. After the induction of the NCC fate (1) by different signal pathways (BMP,Wnt,etc…), NCCs are assumed to undergo an epithelial-to-mesenchymal transition (EMT), in which they express transcriptional regulators (Snail,Slug,etc…). Furthermore, during EMT a cadherin switch leads to modifications of cell-matrix and cell-cell adhesion (2) and finally yields the segregation of NCC out of the neuroectodermal tissue (3).[6]

If one considers the break of symmetry in biological systems, this must be induced by concentration gradients of determinants, including growth factors, such as bone morphogenic protein (BMP), Wnt and fibroblast growth factor (FGF). For the temporal control of the balance between cell-cell and cell-matrix interactions, embryos express different adhesion molecules, such as cadherins, during development. Cadherin undergoes calcium-dependent, homophilic-binding via repeating extracellular (EC) domains.[8-12]

For example, Cadherin-11 (Cad-11) has been shown to be expressed before and throughout migration in the NCC as consequence of an activation by Xwnt-8 (Wnt signalling pathway) and an repression by BMP-4 (BMP signalling pathway).[13,14] However, despite several studies utilizing physisorbed fibronectin on plastic dishes,[13,15] there has been no quantitative study demonstrating crucial roles of the balance between "in plane" and "out of plane" adhesion.

Thus, the primary aim of this thesis is to develop a novel *in vitro* model system that enables one to quantitatively guide NCC differentiation. Amongst various models of biological interfaces, planar lipid membranes, so-called "supported membranes", functionalized with recombinant proteins have been used in this study. Supported membranes sustain a fluid character and serve as two-dimensional matrices to accommodate membrane-associated proteins.

In this study, supported membranes have been functionalized by coupling extracellular domains of cadherins (cadherin-11 and E-cadherin) with oligohistidine tags to 'anchor' lipids with nitrilotriacetic acid (NTA) head groups (Fig. 1-3).[16,17] Though this method allows for creating complex experimental cell-surface models that had been used to study adhesion of T-cells [18] and immunological synapsis,[19] they have never been used to regulate the fate of tissue models.

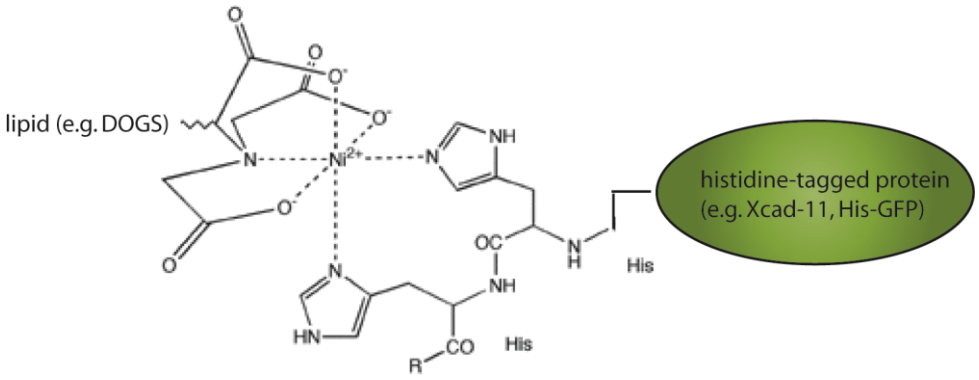

Fig. 1-3: Coupling of a histidine-tagged protein to a Ni^{2+}-NTA complex of an anchor lipid.

Supported membranes functionalized with histidine-tagged, adhesive part (EC1-3) of *Xenopus* cadherin-11 (Xcad-11) have been used to modulate cell-substrate interactions to guide the NCCs differentiation. In the first step (Chapter 4), quantitative functionalization of supported

membrane with Xcad-11 was confirmed by the combination of surface sensitive techniques, such as specular X-ray reflectivity (XRR),[20,21] gracing incidence X-ray fluorescence (GIXF)[22-24] and quartz crystal microbalance with dissipation (QCM-D).[25,26]

In the next step (Chapter 5), *Xenopus* animal cap explants were placed on supported membranes displaying Xcad-11. Here, the explants that had already been induced by the pre-injection of mRNA encoding truncated bone morphogenetic protein receptor (tBR) and *Xenopus* Frizzled 7 (XFz7) have been used in order to unravel the interplay of in plane and out of plane interactions by fine-adjustment of the surface density of Xcad-11.

The interaction between animal cap explants and supported membranes have been monitored by the combination of fluorescence microscopy and reflection interference contrast microscopy (RICM). RICM is a label-free, live cell imaging technique to visualize the height profiles of cell near the contact surface, which has been used to identify the difference in height fluctuation as a function of the surface density of Xcad-11. After careful optimization of the surface density of Xcad-11, it has been demonstrated that supported membranes can stably host tissue explants over days and support the targeted cell differentiation into NCCs.

As the further step, to create concentration gradients of morphogens on supported membranes, one-dimensional gradients of recombinant proteins have been fabricated by applying tangential electric fields (Chapter 6). This method, called "membrane electrophoresis", utilizes the fluidic nature of supported membranes. To create opposite concentration gradients of two proteins, two recombinant proteins possessing opposite signs of net charges have been coupled to supported membranes. The obtained results demonstrated the proof of principles to generate gradients of BMP and Wnt, which is required for NCC differentiation.

Details of the received results are presented and discussed in the following chapters.

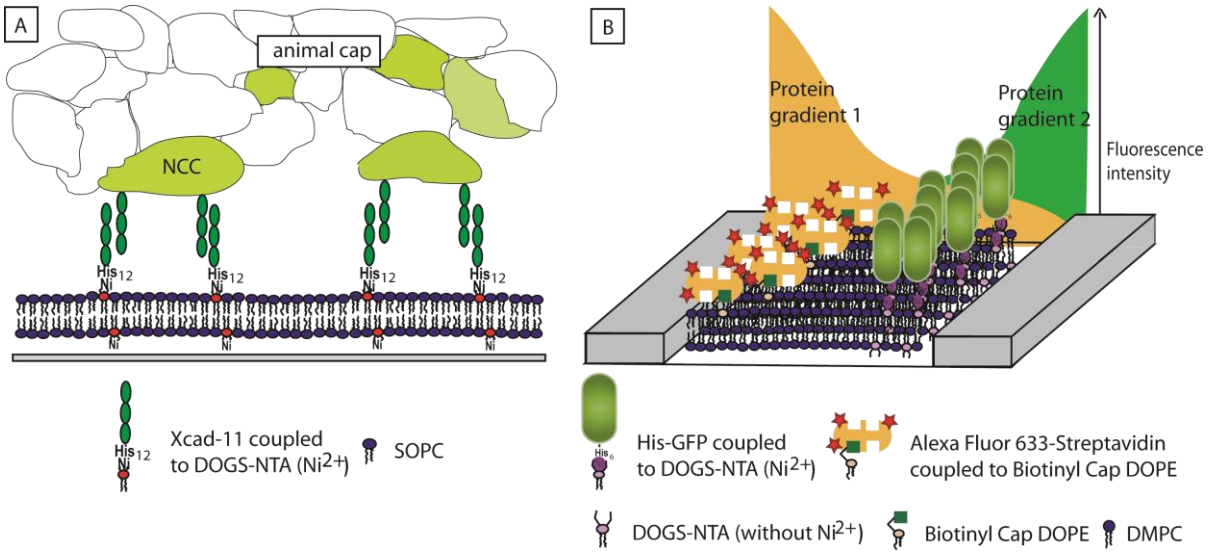

Fig. 1-4: Scheme of the different supported membrane models used in this thesis. (A) Supported membrane functionalized with the histidine-tagged adhesive part (EC1-3) of the recombinant protein *Xenopus* cadherin-11 (Xcad-11). After immobilization of the so-called "animal cap" on this lipid membrane, the targeted cell differentiation of cohesive pluripotent tissue sheets can be monitored by the activation of an additional reporter (*slug*-promoter-GFP). (B) Supported membrane with two different proteins, exhibiting oppositely oriented gradients. Here, the lipid membrane was composed of matrix lipids (DMPC), and two lipid anchors: One lipid with biotin head group (Biotinyl Cap DOPE) and one with NTA head group (DOGS-NTA). The supported membrane was used to generate two oppositely oriented gradients of Alexa Fluor 633 streptavidin and His-GFP by the application of a tangential electric field.

2. Materials and Preparation Methods

2.1. Materials

2.1.1. Chemicals

NaCl, KCl, EDTA, $CHCl_3$ were purchased from Sigma-Aldrich (Germany) and Hepes, $NiCl_2$, $CaCl_2$ from Carl Roth GmbH (Germany). All the chemicals were used without further purification.

2.1.2. Buffers

For all buffers, double deionized water (TKA GenPure, Niederelbert, Germany) with a specific resistance of $\rho > 18$ MΩcm was used.
The following buffers were used for the experiments:

- Hepes buffered saline (HBS) containing 150 mM NaCl, 10 mM Hepes, pH 7.4
- Ni^{2+}-HBS: HBS containing in addition 10 mM $NiCl_2$, pH 7.4
- "Ni^{2+}-free buffer": HBS containing 100 mM KCl, 5 mM Hepes, pH 7.4
- "Ni^{2+}-loaded buffer": HBS containing 100 mM KCl, 5 mM $NiCl_2$, 5 mM Hepes, pH 7.4
- 1 mM citrate buffer containing 0.33 mM citric acid, 0.67 mM sodium citrate, pH 5.2

2.1.3. Lipids

The following lipids were obtained from Avanti Polar Lipids (Alabaster, AL, USA), dissolved in $CHCl_3$ at a concentration of 1 mg/ml and stored at -20 °C:

<u>Lipids without modified head group:</u>

- 1- Stearoyl-2-oleoyl-sn-glycero-3-phosphocholine (SOPC; Fig. 2-1A)
- 1,2-Dimyristoyl-sn-glycero-3-phosphocholine (DMPC; Fig. 2-1B)

Head group modified lipids:

- 1,2-Dioleoyl-sn-glycero-3-[(N-(5-amino-1-carboxypentyl)-iminodiacetic acid)succinyl] (nickel salt) (DOGS-NTA (Ni^{2+}); Fig. 2-1C)
- 1,2-Dioleoyl-sn-glycero-3-phosphoethanolamine-N-(cap biotinyl) (Biotinyl Cap DOPE; Fig. 2-1D)
- N-(7-nitrobenz-2-oxa-1,3-diazol-4-yl)-1,2-dihexadecanoyl-sn-glycero-3-phosphoethanolamine (NBD-DHPE; Fig. 2-1E)

The structures of the lipids are shown in Fig. 2-1.

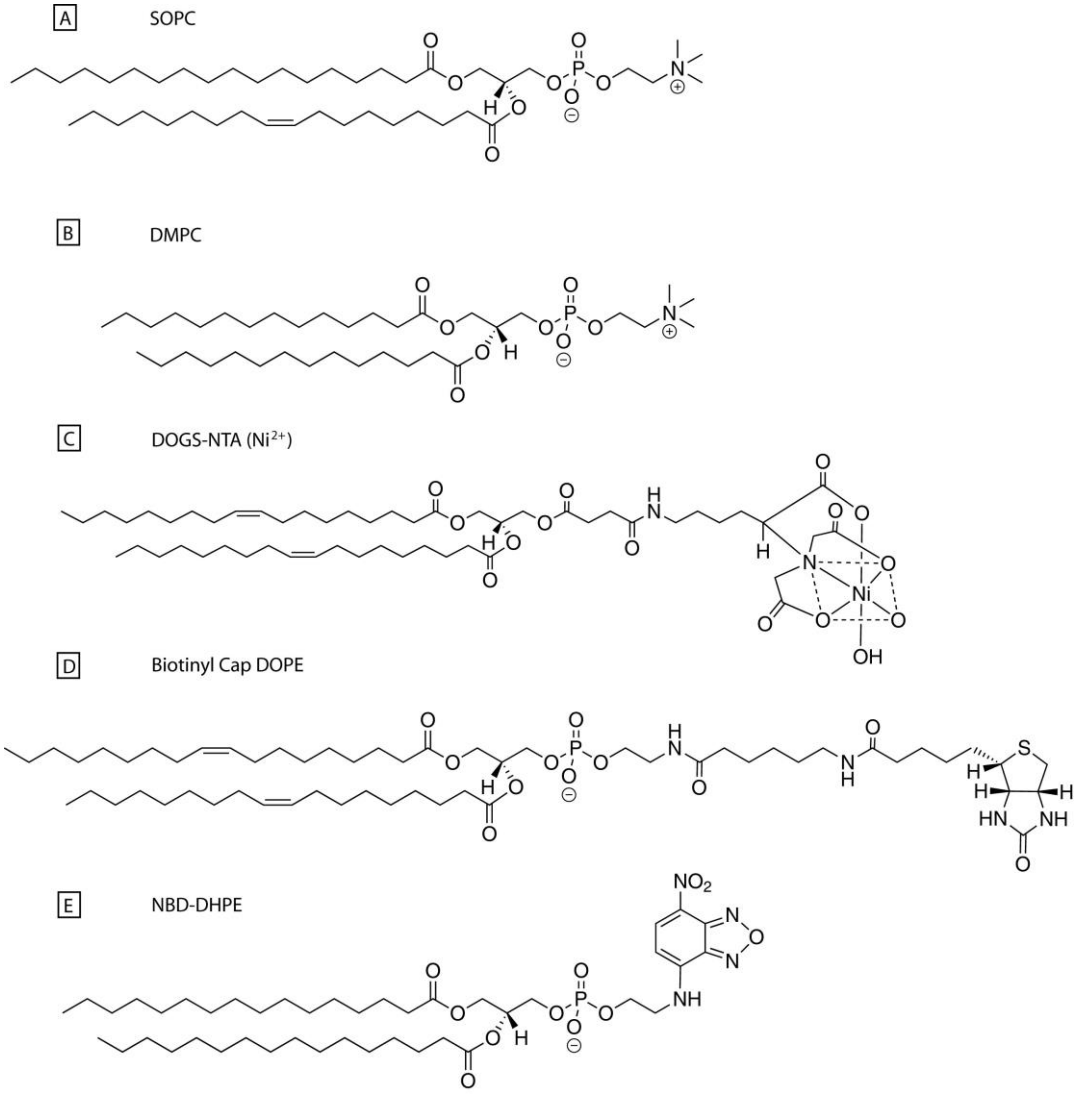

Fig. 2-1: Structures of lipids used in this thesis.

2.1.4. Proteins

Xenopus cadherin 11 EC 1-3 Snap His12 (Xcad-11)[27,28] and human epithelial cadherin EC 1-5 Snap His12 (E-cad) was synthesized by Dr. Christina Deichmann (Cell and Developmental Biology, Karlsruhe Institute of Technology, Germany). In brief, the extracellular domain 1-3 (EC1-3) of Xcad-11 and the extracellular domain 1-5 (EC1-5) of epithelial cadherin (E-cadherin), both subcloned in pSEMS1-26m (Covalys, Germany), were fused to a mutated hAGT protein.[29] Additionally, a PCR amplified His12-tag was inserted with specific primers.
Alexa Fluor 633 streptavidin (streptavidin covalently attached to Alexa Fluor® 633), was purchased from Life technologies (Darmstadt, Germany). The far-red fluorescent Alexa Fluor 633 streptavidin conjugate has its excitation maximum at 632 nm and its emission maximum at 647 nm.
Green fluorescent protein (GFP) was inserted in pQE-31 vector (Qiagen, Hilden, Germany) with specific primers. The resulting histidine-tagged GFP (His-GFP) was expressed in Escherichia coli (E. coli). His-GFP has two excitation maxima one at 395 nm and the second at 475 nm. The emission maximum is located at 647 nm.

2.1.5. Preparation of pluripotent tissue sheets from *Xenopus laevis*

Breeding and micromanipulation of *Xenopus laevis* embryos as well as the preparation of the tissue sheets (so-called animal caps) was done in cooperation with Dr. Christina Deichmann (Cell and Developmental Biology, Karlsruhe Institute of Technology, Germany). *Xenopus laevis* embryos were obtained by in vitro fertilization and staged according to Nieuwkoop and Faber.[30] To induce the formation of neural crest cells (NCC) in the animal caps, truncated bone morphogenetic protein receptor (300 pg; tBR) and *Xenopus* Frizzled 7 (500 pg; XFz7), a kind gift of H. Steinbeisser (Division of developmental genetics, Heidelberg university hospital, Germany) was injected as mRNA into one blastomere of a two-cell stage embryo. Furthermore a cell membrane tracer (500 pg; GAP43-mCherry RNA) to visualize cell membranes as well as an additional reporter (150 pg; slug-promoter-GFP DNA) to gain experimental evidence of neural crest induction were co-injected.
The transformed embryos were cultivated in 0.1x modified Barth solution holding (MBSH) at 14 °C. When the embryos reached blastula stage (stage 8 to 9), the vitelline membrane was manually removed with fine forceps. The presumptive ectodermal sheets (approximately

0.4 x 0.4 mm) were cut from the blastocoel roof of the embryo prior to place them on supported membranes. The explants were seeded with their inner blastocoelic surface facing to the substrate and fixed by a cover glass to prevent the rolling up.

2.2. Substrates

2.2.1. Substrate and cleaning procedure

As solid substrates, silicium wafers with native oxide (cut to 25 x 25 mm, Si-Mat, Landsberg am Lech, Germany) were used for specular X-ray reflectivity (XRR) at solid/water interface, AT cut quartz crystals (5 MHz) coated with SiO_2 (QSX 303, Q-Sense, Gothenburg, Sweden) were used for quartz crystal microbalance with dissipation (QCM-D) experiments, and glass cover slips with a thickness of 0.17 ± 0.01 mm (24 x 24 mm, 50 x 24 mm or 75 x 24 mm, Carl Roth GmbH, Germany) were used for fluorescence microscopy, reflection interference contrast microscopy (RICM) and electrophoresis experiments.

If not stated otherwise, all substrates were cleaned by using a modified RCA protocol:[31] The samples were sonicated for 5 min in acetone, ethanol, methanol, and water, then immersed in a solution of H_2O_2 (30%) / NH_4OH (30%) / H_2O (1:1:5 by volume) and sonicated for 5 min at room temperature before soaking them for another 30 min at 60 °C. Afterwards, they were intensively rinsed with water, dried at 70 °C and stored in a vacuum chamber.

2.2.2. Fabrication of patterned glass substrates

To pattern the glass substrate with specific lipid bilayers a scaffold of Cr/Ni (20:80)-barrier was implemented to inhibit the thermal diffusion and electrical drift. The barriers were made by patterning a cleaned glass substrate by photolithography and a subsequent metal lift-off process (schematically illustrated in Fig. 2-2). In details:

- Photolithography:

  - Cleaning the glass substrate with the modified RCA protocol
  - Heating the substrate up to 200 °C for 30 min, then 15 min to 100 °C
  - Cooling and cleaning the sample with a nitrogen stream for 2 min
  - Spin-coating of the positive photoresist ma-p 1205 (micro resist technology, Berlin, Germany) at 500 rpm for 3 sec, then 3000 rpm for 30 sec
  - Performing a pre-exposure bake on a hotplate at 100 °C for 1 min
  - Exposing the spin-coated sample with a HBO 350 mercury lamp for 1 sec (dose rate = 35 $mJcm^{-2}$)
  - Developing the exposed sample for 25 sec in the developer ma-D 331 (micro resist technology, Berlin, Germany)
  - Washing the developed sample with water

- Lift-off procedure:

  - Heating up the patterned glass substrate by photolithography to 80 °C for 1h
  - Depositing of a 10 nm thick layer of Cr/Ni (20:80 alloy) all over the sample by metal sputtering (Leica EM ACE 600, Leica Microsystems, Wetzlar, Germany) to cover the photoresist and areas in which the photoresist has been cleared
  - Removing the photoresist (and the metal on top) by rinsing the sample with the remover mr-Rem 660 (micro resist technology, Berlin, Germany) for 2 min
  - Washing the sample with water to ensure that no photoresist remover is left on the substrate
  - Cleaning the resulting patterned sample by sonication for 5 min in acetone, ethanol, methanol and water
  - Treating the substrate for 30 min with UV/O_3 (UV/Ozone ProCleaner™220, Bioforce NanoSciences INC., Ames, USA) prior to use

The patterns displayed squares with 200 µm, 300 µm, 400 µm and 500 µm edge length (appendix A.1). The width and height of the barrier are demonstrated to be 10 µm and 13 ± 2 µm, respectively (appendix A.2).

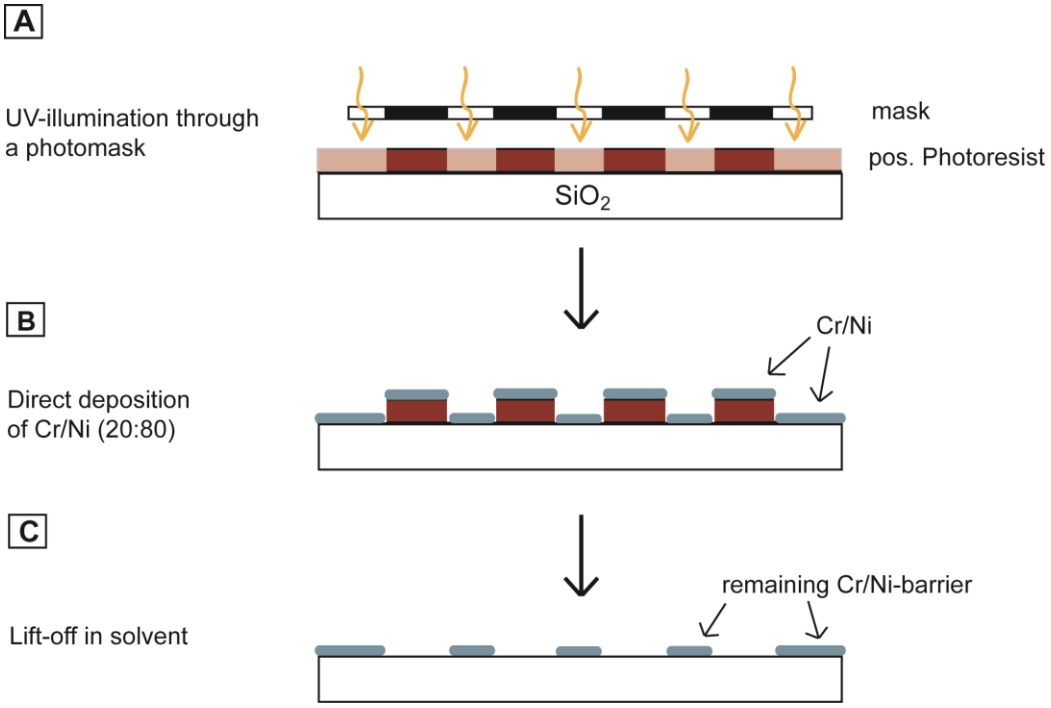

Fig 2-2: Schematic illustration of the Cr/Ni-barrier fabrication.

2.3. Measurement chambers

In this thesis three types of chambers were used. The first kind of chamber is a self-built liquid cell used for high energy specular X-ray reflectivity (XRR) at the solid/water interface and is described in Chapter 3.1.2.

Second, as observation chamber for animal cap cell experiments (Chapter 5) a 2-well chamber (Nunc® Lab-Tek® II ™ Chamber Slide™ system, Sigma-Aldrich, Germany) without bottom and adhered to a RCA-cleaned 75 x 24 mm glass cover slip was utilized. Here, as adhesive Delo®-Photobond 4442 (Delo, Windach, Germany) was used and cured under UV-light for 12 hours.

Third, a “preparation” chamber was utilized to prepare the patterned supported membranes on RCA-cleaned 24 x 24 mm glass cover slip before mounting the substrate to the membrane electrophoresis chamber (Chapter 3.6.2). The preparation chamber is shown in Fig. 2-3 and consisted of two steel rings (A, E), which were screwed together, and encased a cover slip (B) and a Teflon inset (C) with o-ring (D). The main advantage of this chamber is the possibility

to unscrew the two steel rings in order to place the cover slip, exhibiting the prepared surface, in another experimental setup (e.g. electrophoresis chamber, described in Chapter 3.6.2).

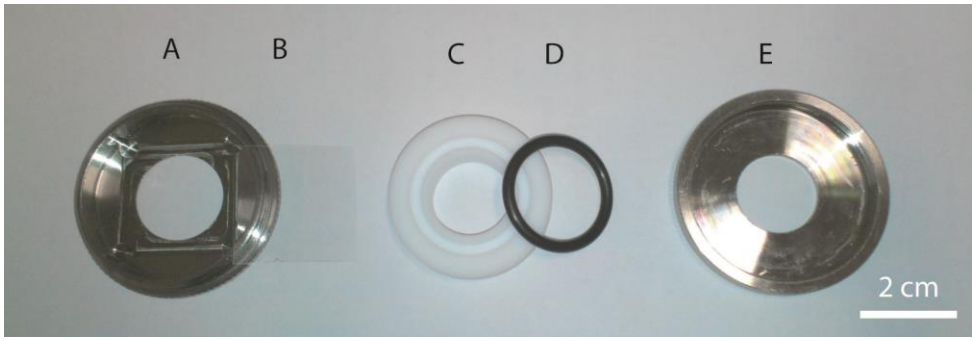

Fig. 2-3: Components of the "preparation" chamber. (A) Lower metal ring with indentation for the cover slip. (B) RCA-cleaned 24 x 24 mm glass cover slip. (C) Teflon inset. (D) O-ring. (E) Upper metal ring.

2.4. Preparation methods

2.4.1. Lipid monolayer at the air/water interface

Lipid monolayers at the air/water interface were created by deposition of SOPC solutions containing different molar ratios of DOGS-NTA (5, 25, and 50 mol%) onto Ni^{2+}-free or Ni^{2+}-loaded buffer in a trough of a Langmuir film balance provided by the beamline ID10B (ESRF, Grenoble, France). After 20 min of solvent evaporation the film was compressed to a surface pressure of π = 20 mN/m. The coupling of Xcad-11 to lipid monolayer was achieved by the injection of protein solution (40 µg/ml in Ni^{2+}-free buffer) underneath the monolayer and incubation for at least 6 hours.

2.4.2. Preparation of small unilamellar vesicles (SUV)

Lipid solutions with different molar ratios of DOGS-NTA in SOPC (0, 1, 2, and 5 mol%) were prepared for XRR, RICM, and QCM-D experiments (Chapter 4.3.2.1, Chapter 5 and

Chapter 4.3.2.2, respectively) and mixtures of Biotinyl Cap DOPE and DOGS-NTA in DMPC for electrophoresis experiments (Chapter 6) by mixing appropriate amounts of the stock solutions. After evaporating the solvents under a stream of nitrogen, the samples were placed in a vacuum oven for 24 h in order to remove all traces of solvent. The dry lipid films were re-suspended in HBS at a total concentration of 1 mg/ml. Small unilamellar vesicles (SUVs) were obtained by sonicating lipid solutions with a titanium tip sonicator (Misonix, New York, USA) for 30–60 min, followed by centrifugation in an Eppendorf centrifuge (10 min at 13200 x *g*) to separate titanium particles. After the preparation, SUV suspensions were diluted to a final concentration of 0.5 mg/ml and were stored at 4 °C. SUV suspensions for electrophoresis experiments were incubated for 30 min at 40 °C before use.

2.4.3. Vesicle fusion

The small unilamellar vesicles (SUVs) rupture if they come in contact with a hydrophilic surface and spread homogenously over the surface. This process is called vesicle fusion and yields, under appropriate conditions, solid supported membrane exhibiting self-healing and a high fluidity. A schematic illustration of the vesicle fusion is shown in Fig. 2-4.

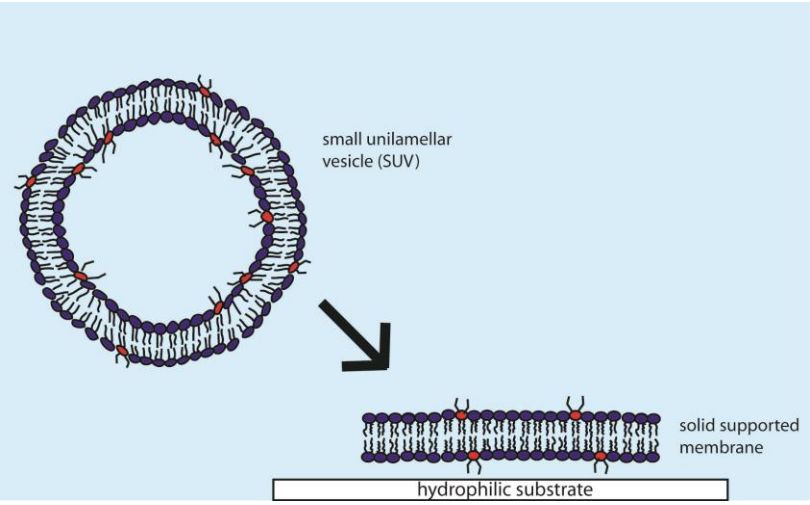

Fig. 2-4: Schematic illustration of the vesicle fusion yielding solid supported membranes.

2.5.4. Preparation of functionalized solid supported membranes

Supported membranes were prepared by deposition of SUV suspensions on cleaned substrates as described before. After removing excess vesicles by rinsing with buffer, the supported membranes were functionalized with the following preparation procedures:

- For Xcad-11 functionalization:

  - Incubation of supported membrane with Ni^{2+}-HBS for 20 min
  - Intensive rinsing with HBS
  - Incubating with Xcad-11 in HBS buffer (~ 20 µg/ml) for 1 h
  - Rinsing with HBS

- For Alexa Fluor 633 streptavidin functionalization (before electrophoresis; Chapter 6):

  - Incubation of patterned supported membrane with Alexa Fluor 633 streptavidin in HBS buffer (~ 5 µg/ml) for 20 min
  - Intensive rinsing with HBS
  - Exchange the buffer to citrate buffer

  It has to be noted that all these steps were done at 40 °C

- For His-GFP functionalization (after electrophoresis):

  - Incubation of patterned supported membrane with Ni^{2+}-HBS for 20 min
  - Intensive rinsing with HBS
  - Incubating with His-GFP in HBS buffer (~ 10 µg/ml) for 2 h
  - Rinsing with HBS

  It has to be noted that all these steps were done below the transition temperature of DMPC (T_m DMPC = 23°C).

3. Instrumental Techniques

3.1. Specular X-ray reflectivity (XRR)

3.1.1. Principle of the technique

X-ray reflectivity (XRR) is a non-destructive technique used to study buried structures/interfaces in very high spatial resolution (Å-resolution). In this paragraph the basics of x-ray reflectivity will be explained.

The refractive index n of a medium depends on the frequency of the incident beam and therefore on its energy. X-rays usually possess energies much higher than the binding energies of most electrons in atoms. In other words, the frequency of the X-ray waves is much higher than the resonance frequencies of the electron thus they can be considered as free electrons. As consequence, the refractive index of matter is for X-rays slightly lower than 1 and *n* can be written as following:

$$n = 1 - \delta + i\beta \tag{3.1}$$

Here δ considers the dispersion and β the absorption of the incident beam. These parameters correlate with the electron density ρ_e and the linear absorption coefficient μ of the investigated material:

$$\delta = \frac{\lambda^2}{2\pi}\rho_e r_0 = \frac{\lambda^2}{2\pi} SLD \tag{3.2}$$

$$\beta = \frac{\lambda}{4\pi}\mu \tag{3.3}$$

with λ corresponding to the wave length of the incident X-ray beam and the scattering length density (SLD) as product of the electron density ρ_e multiplied with the classical electron radius r_0 (2.82 x 10^{-12} cm).

The values for δ are typically in the order of 10^{-5} - 10^{-6} and for β in the order of 10^{-8} - 10^{-9}.[32] Thus β can be ignored without introducing significant errors in many cases.

For X-rays the well-known Snell's law can be applied. Here, at the interface between two media with refractive index n_0 and n_1, the angle at which radiation is refracted (α_1), is given by the ratio of the refractive indices and the incident angle α_0:

$$\cos(\alpha_1) = \frac{n_0}{n_1}\cos(\alpha_0) \tag{3.4}$$

If the first medium is considered to be vacuum ($n_0 = 1$) and the second medium to be a liquid which has for X-rays a refractive index n_1 slightly lower than 1 (according to equation 3.1), it follows $\alpha_1 < \alpha_0$. At a certain incident angle α_0 (the so-called critical angle α_c) the angle of refraction α_1 equals 0°. Below the critical angle α_c total reflection will be obtained and only an evanescent field penetrates into the medium 1 with a decay length of several nanometers. If $n_0 = 1$ (air), $n_1 = 1 - \delta$ is inserted into Snell's law and the cosine is expanded in a Taylor series, then α_c can be written as:

$$\alpha_c = \sqrt{2\delta} \tag{3.5}$$

Fresnel reflectivity

A plane X-ray wave can be expressed as $\Psi_j = E_j e^{i(\omega t - kjr)}$, where ω is the angular frequency, r the position vector, E_j corresponding to the amplitude and k_j to the wavenumber for incident (j=I), reflected (j=R) or transmitted (j=T) waves as indicated in Fig. 3-1.

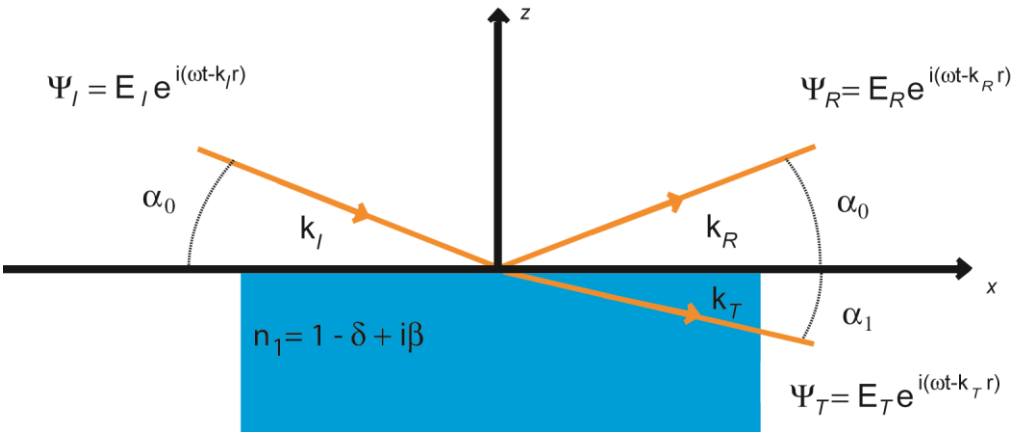

Fig. 3-1: Illustration of the reflection (R) and transmission (T) of an incoming (I) X-ray wave.

By imposing the boundary conditions that the wave and its derivative at the interface (z = 0) must be continuous the relationship between the amplitudes is:

$$E_I + E_R = E_T \tag{3.6}$$

and

$$E_I k_I + E_R k_R = E_T k_T \tag{3.7}$$

Considering the first medium to be vacuum ($n_0 = 1$), than the wavenumber is denoted by $k = |k_I| = |k_R|$ and the transmitted wavenumber $|k_T|$ in the second medium ($n_1 < 1$) equals $n_1 k$ (with $k = 2\pi/\lambda$). Using the components of k parallel to the surface results in:

$$E_I k \cos(\alpha_0) + E_R k \cos(\alpha_0) = E_T (n_1 k) \cos(\alpha_1) \tag{3.8}$$

The combination of this equation with equation 3.6 leads to Snell's law (see equation 3.4):

$$\cos(\alpha_0) = n_1 \cos(\alpha_1) \tag{3.9}$$

From equation 3.6 and together with the components of k perpendicular to the surface it follows:

$$-(E_I - E_R) k \sin(\alpha_0) = -E_T (n_1 k) \sin(\alpha_1) \tag{3.10}$$

that further yields to

$$\frac{E_I - E_R}{E_I + E_R} = n_1 \frac{\sin(\alpha_1)}{\sin(\alpha_0)} \cong \frac{\alpha_1}{\alpha_0} \tag{3.11}$$

For reflectivity measurements the used incident angle is in most cases very small ($\alpha_0 < 5°$). Therefore, it will not be distinguished between the two different (parallel and perpendicular) polarisations and equation 3.11 is used to obtain the reflection coefficient $r_{0,1}$:

$$r_{0,1}(\alpha) \equiv \frac{E_R}{E_I} = \frac{\alpha_0 - \alpha_1}{\alpha_0 + \alpha_1} \tag{3.12}$$

and for the transmittance coefficient t_0

$$t_{0,1}(\alpha) \equiv \frac{E_T}{E_I} = \frac{2\alpha_0}{\alpha_0 + \alpha_1} \tag{3.13}$$

Equation 3.12 and 3.13 are the so-called Fresnel equations. The corresponding coefficients for the reflected $R(\alpha)$ and transmitted $T(\alpha)$ intensity is given by:

$$R(\alpha) = \frac{I_R}{I_I} = \left|r_{0,1}\right|^2 \quad ; \quad T(\alpha) = \frac{I_T}{I_I} = \left|t_{0,1}\right|^2 \tag{3.14}$$

Penetration depth

For small angles α_0 and α_1 the cosines in Snell's law (equation 3.4) can be expanded to yield

$$\alpha_0^2 = \alpha_1^2 + 2\delta - 2i\beta \tag{3.15}$$

and after implementing of equation 3.5:

$$\alpha_0^2 = \alpha_1^2 + \alpha_c^2 - 2i\beta \tag{3.16}$$

From this equation, the complex number for α_1 can be derived for a given incident angle α_0. Furthermore, α_1 can be split into its real and imaginary parts.

$$\alpha_1 = \mathrm{Re}(\alpha_1) + i\,\mathrm{Im}(\alpha_1) \tag{3.17}$$

The decay of the transmitted wave depends on the z position in the reflecting material:

$$E_T e^{i(k\alpha_1)z} = E_T e^{i\,\mathrm{Re}(\alpha_1)z} e^{-k\,\mathrm{Im}(\alpha_1)z} \tag{3.18}$$

and therefore the penetration depth Λ of the evanescent wave is given by:

$$\Lambda = \frac{1}{2k\,\mathrm{Im}(\alpha_1)} \tag{3.19}$$

i.e., the point at which the beam intensity has decayed to 1/e of the initial intensity.

Reciprocal space

In the reciprocal space the incident and reflected waves (with wave vectors k_I and k_R) are described by $\left|\vec{k}\right| = 2\pi/\lambda$. As shown in Fig. 3-2 the scattering vector $\vec{q} = \vec{k}_R - \vec{k}_I$ characterizes the scattering process.

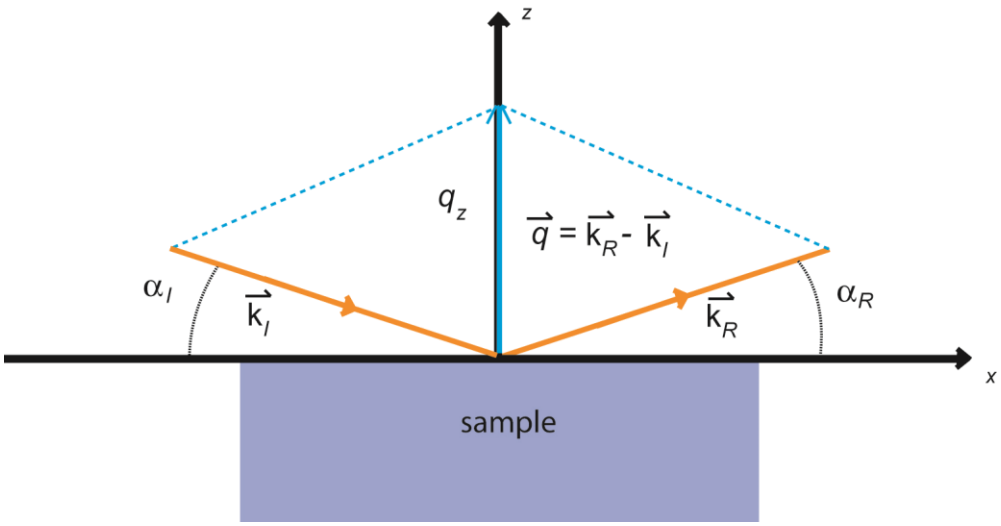

Fig 3-2: Sketch of the scattering geometry. The scattering vector (or momentum transfer) $\vec{q}$ is defined by the incident and reflected wave vector $\vec{k}_I$ and $\vec{k}_R$.

In the case of specular reflectivity ($\alpha_I = \alpha_R = \alpha_0$), the perpendicular component q_z of the scattering vector $\vec{q}$ is used:

$$q_z = \frac{2\pi}{\lambda}\left(\sin(\alpha_I) + \sin(\alpha_R)\right) = \frac{4\pi}{\lambda}\sin(\alpha_0) \tag{3.20}$$

Due to the fact that only the perpendicular wavevector has to be considered, the use of q_z allows efficient calculations. By using equation 3.12, 3.14 and 3.16, the reflectivity in terms of q_z can be written as:

$$R(q_z) = \left| \frac{q_z - \sqrt{q_z^2 - q_c^2 + 2i(2k)^2\beta}}{q_z + \sqrt{q_z^2 - q_c^2 + 2i(2k)^2\beta}} \right|^2 \tag{3.21}$$

In Fig. 3-3, the reflectivity $R(q_z)$ is plotted as a function of q_z. It is evident that (1) below q_c (= the q_z value at the critical angle) there exist a plateau of total reflection, (2) above q_c the reflectivity decreases very fast and (3) at q_z values much higher than q_c ($q_z > 3\ q_c$) the reflected intensity decays as q_z^{-4}.

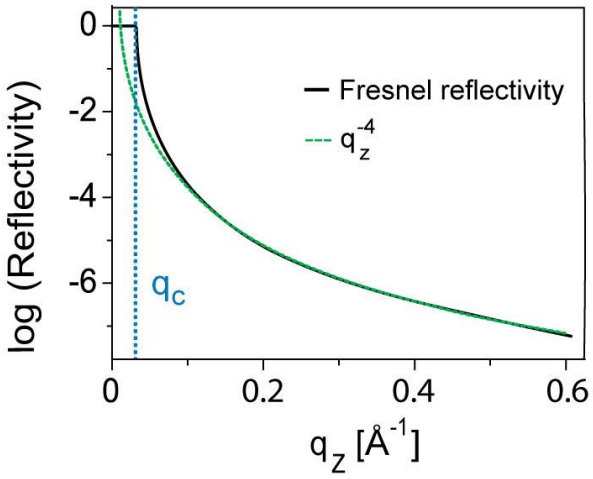

Fig. 3-3: Simulated Fresnel reflectivity from an ideal air/silicon interface (black line). The green dotted line corresponds to the reflected intensity decay of q_z^{-4}.

Reflection from a thin and homogenous layer

In Fig. 3-4, the reflection at one single thin and homogenous layer (1) on an infinitely thick substrate (2) and in contact with air (0) is considered.

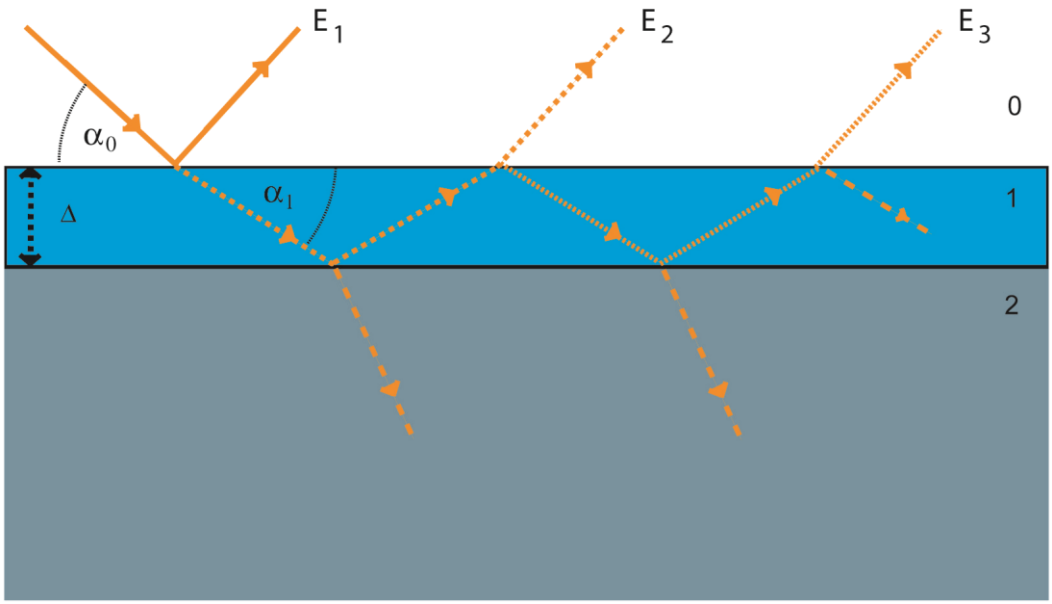

Fig. 3-4: Illustration of the reflection and transmission from a slab of finite thickness (slab 1). Slab 2 corresponds to the substrate with a thickness considered to be infinite.

The Fresnel reflection and transmission coefficients for the air/layer interface and the layer/substrate interface are $r_{0,1}$, $t_{0,1}$ and $r_{1,2}$, $t_{1,2}$, respectively, and introduced with equation 3.12 and 3.13. The total reflectivity is given by:

$$\begin{aligned} r_{layer} &= r_{0,1} + t_{0,1}r_{1,2}t_{1,0}P^2 + t_{0,1}r_{1,0}r_{1,2}^2t_{1,0}P^4 + \ldots \\ &= r_{0,1} + t_{0,1}r_{1,2}t_{1,0}P^2\sum_{n=0}^{\infty}\left(r_{1,0}r_{1,2}P^2\right)^n \\ &= r_{0,1} + \frac{t_{0,1}r_{1,2}t_{1,0}P^2}{1 - r_{1,0}r_{1,2}P^2} \end{aligned} \tag{3.22}$$

with the phase factor $P^2 = \exp(iq_{z,1} \times d) = \exp(i2k_1 \sin\alpha_1 \times d)$, $k_1 = n_1 \times k$ and the thickness of the layer *d*.

By using the conditions $r_{0,1}$ = - $r_{1,0}$ and $r^2_{0,1}$ + $t_{0,1}t_{1,0}$ = 1 (which follow from the Fresnel equations), this equation can be simplified to:

$$r_{layer} = \frac{r_{0,1} + r_{1,2}P^2}{1 + r_{0,1}r_{1,2}P^2} \tag{3.23}$$

Reflection from stratified layers

In general X-ray reflectivity is used to investigate systems with more than one layer. Therefore, the result for a single slab must be extended to a system with N-layers sitting on an infinitely thick substrate (see Fig. 3-5) with an iterative formalism first described by Parrat.[33]

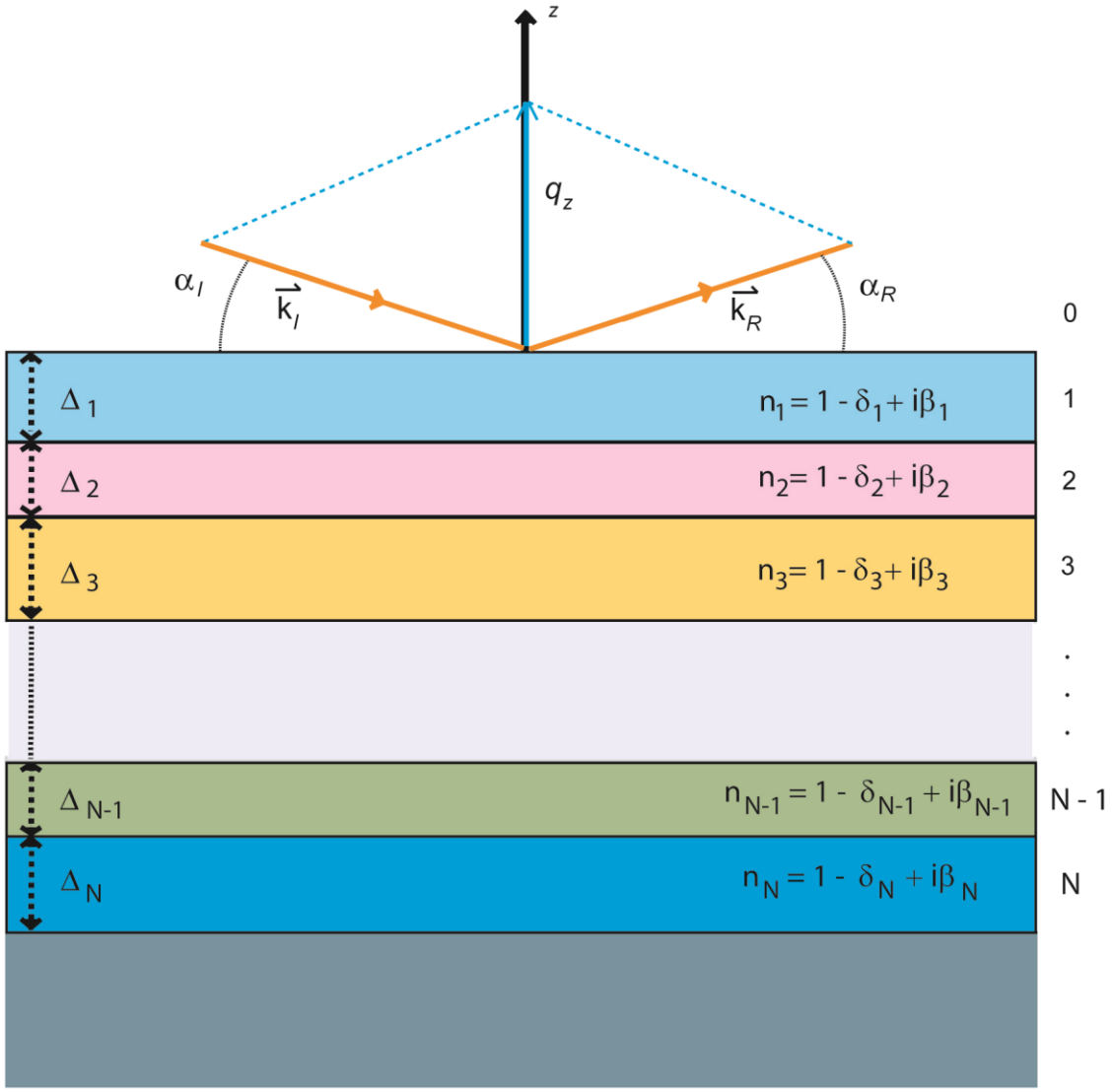

Fig. 3-5: Sketch of a stratified system of homogenous slabs utilized to obtain the effective reflectivity by the Parrat formalism.

Implementing the description for q_z (equation 3.20) into the Fresnel relation (equation 3.12) yield the reflection coefficient of each isolated interface:

$$r'_{j,j+1} = \frac{q_{z,j} - q_{z,j+1}}{q_{z,j} + q_{z,j+1}} \tag{3.24}$$

where the prime denotes the reflectance that does not include multiple internal reflections. The effective reflectivity of the stratified system is calculated in a recursive manner by starting from the interface between the infinitely thick substrate (∞) and the bottom of the N'th layer (*N*). The infinite thickness of the substrate excludes multiple reflections. Therefore, it yields to:

$$r'_{N,\infty} = \frac{q_{z,N} - q_{z,\infty}}{q_{z,N} + q_{z,\infty}} \tag{3.25}$$

For the reflection coefficient of the next interface (*N* to *N*-1), multiple reflections have to be considered. Thus $r'_{N,\infty}$ was implemented in equation 3.23 yielding to:

$$r_{N-1,N} = \frac{r'_{N-1,N} + r'_{N,\infty} P^2}{1 + r'_{N-1,N} r'_{N,\infty} P^2} \tag{3.26}$$

with the phase factor $P^2 = \exp(iq_{z,N} \times d_N)$ and the thickness of the N'th layer d_N. Taking $r_{N-1,N}$ to obtain the next interface (*N*-1 to *N*-2) results in:

$$r_{N-2,N-1} = \frac{r'_{N-2,N-1} + r_{N-1,N} P^2}{1 + r'_{N-2,N-1} r_{N-1,N} P^2} \tag{3.27}$$

This recursion has to be continued until the total reflection coefficient at the air/layer interface $r_{0,1}$ is obtained. Finally the effective reflectivity of the stratified system is given (according to equation 3.14) as:

$$R(q_z) = \left| r_{0,1} \right|^2 \tag{3.28}$$

Roughness of the Interfaces

Up to now only ideal and smooth interfaces were considered. Realistic (non-ideal) interfaces between homogenous layers have a certain degree of roughness. This roughness attenuates the X-ray intensity causing a gradual transition of the refractive index (and therefore, in the scattering length density SLD) and not a sharp jump as expected for ideal interfaces. The observed transition can be described by using an error function containing the transition width (or mean square roughness) σ.

To apply this interfacial roughness to the reflectivity coefficients $r'_{j,j+1}$ a modification of equation 3.24 should be done according to Névot and Croce:[34]

$$\tilde{r}_{j,j+1} = r'_{j,j+1} \exp(-\frac{1}{2} q_z^2 \sigma_{j,j+1}^2) \qquad (3.29)$$

3.1.2. Protocol for XRR at the solid/liquid interface

High energy specular X-ray reflectivity measurements were performed at the ID10B beamline at the European Synchrotron Radiation Facility (ESRF, Grenoble, France) by illuminating the samples at 22 keV, which guarantees approximately 40 % transmission through 1 cm of water.[20,21] The transmission rate allows characterizations of supported biological membranes at the solid/liquid interface. Prior to the membrane deposition, the cleaned Si wafers were placed into a Teflon chamber with Kapton windows (Fig. 3-6). Supported membranes were prepared as described in Chapter 2.5.4.

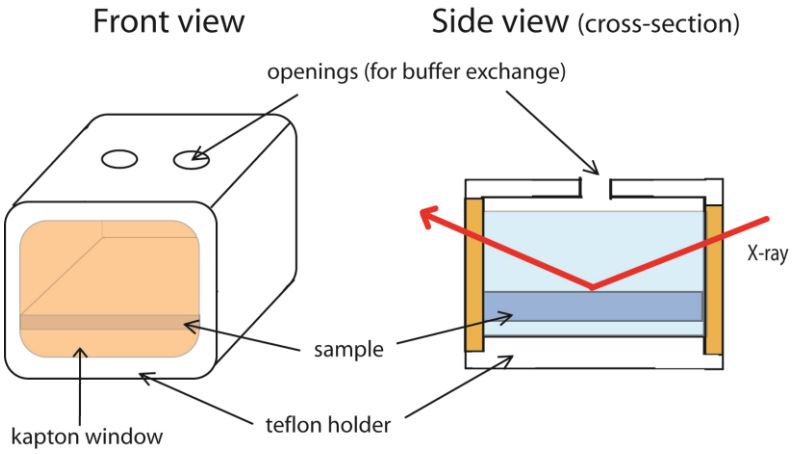

Fig. 3-6: The self-built liquid cell used for high energy XRR.

The reflectivity data is represented as a function of the momentum transfer q_z (equation 3.20). For each measurement point, the reflectivity was corrected for the beam footprint and for the beam intensity with the aid of an in-beam monitor. To minimize the artefacts from radiation damage, the reproducibility of the results was carefully checked by translating the sample position in the direction perpendicular to the scattering plane. In order to interpret the obtained reflectivity data, slab models exhibiting homogenous layers with particular thicknesses d, electron densities ρ and root mean square roughnesses σ were used. The analysis was performed by using the Parrat formalism[33] with a genetic χ^2-minimization algorithm implemented in the Motofit software package.[35]

3.2. Grazing incidence X-ray fluorescence (GIXF)

3.2.1. Principle of the technique

Grazing incidence X-ray fluorescence (GIXF) is a powerful technique to obtain elemental depth-profiles at the air/liquid interface by the measurement of fluorescence signals at various incident angles.

Penetration depth

GIXF takes advantage of the small penetration depth of the evanescent X-ray waves at small angles of incidence. As described in Chapter 3.1.1 the penetration depth Λ of the evanescent wave is given as:

$$\Lambda = \frac{1}{2k\,\mathrm{Im}(\alpha_1)} \tag{3.30}$$

By applying Snell's law for the relation of the angle of refraction α_1 and a given incident angle α_0, one obtains at small angles:[22]

$$\Lambda(\alpha_0) = \frac{\lambda}{\sqrt{8}\pi}\left[\sqrt{\left(\alpha_0^2 - \alpha_c^2\right)^2 + 4\beta^2} - \left(\alpha_0^2 - \alpha_c^2\right)\right]^{-\frac{1}{2}} \tag{3.31}$$

where, the penetration depth of the evanescent field depends on the angle of incidence α_0 and β is the imaginary part of the refractive index $n = 1 - \delta + i\beta$.

A typical example for the X-ray penetration depth as a function of incident angle is shown in Fig. 3-7. The penetration depth below the critical angle (α_c =0.138 °; dotted line) is a few nanometers.

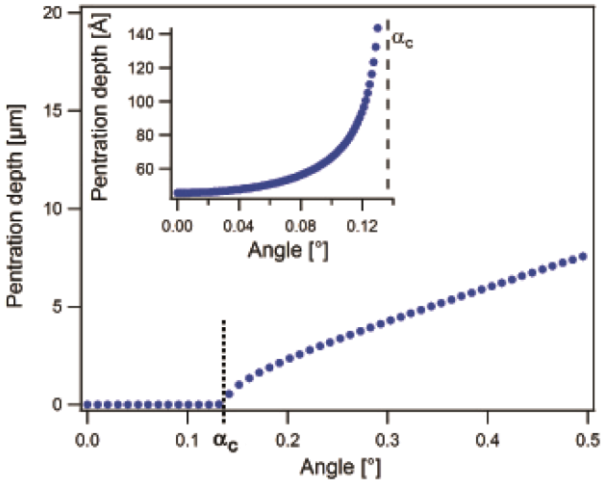

Fig. 3-7: The penetration depth into water sub phase as a function of the incident angle at an X-ray energy of 9 keV. The inset shows the penetration depth below the critical angle (α_c; dotted line).

Fluorescence intensities for stratified interfaces

The fluorescence intensity $I_i^f(\alpha_0)$ from an element *i* (distributed to a depth *z* from the air/water interface) at an incidence angle α_0 can be written as:

$$I_i^f(\alpha_0) = S\int_0^\infty I^{ill}(z,\alpha_0)\, c_i(z) \exp(-z/L_i)\, dz\,. \qquad (3.32)$$

Here, *S* is a proportional constant which is scaled out in our experimental system by the normalization to the fluorescence signal from the corresponding blank buffer, $c_i(z)$ is the concentration of element *i* at a depth *z*. The exponential term represents the attenuation of the fluorescence emission between the position *z* and the air/water interface, where L_i is the attenuation length of water at the characteristic fluorescence line (e.g. $L_{\mathrm{Ni\ K\alpha}}$ = 802.8 µm, $L_{\mathrm{S\ K\alpha}}$ = 24.04 µm). $I^{ill}(z,\alpha_0)$ corresponds to the illumination profile depending on the electronic structure of the interface and on the incident angle α_0. The illumination profile can be determined by a matrix propagation technique using a slab model.[36]

Illumination profile

The illumination profile $I^{ill}(z,\alpha)$ can be determined by using the method of Ohta and Ishida.[37] They calculated the illumination profile intensity in stratified media for a light beam by utilizing the so-called Abeles's matrix formalism[38] and a slabs model. The necessary parameters of the slabs have to be obtained by XRR analysis (described in Chapter 3.1.1). The illumination profile $I^{ill}(z,\alpha)$ is expressed as $\left|E^{+}(z)+E^{-}(z)\right|^{2}$ where $E^{+}(z)$ and $E^{-}(z)$ are the electromagnetic waves, propagating in positive and negative direction with respect to the sample surface, respectively. The way to obtain the exact expression of $E^{+}(z)$ and $E^{-}(z)$ is described in the following. First the electromagnetic wave amplitudes at the boundaries are expressed as:

$$\begin{pmatrix} E_0^+ \\ E_0^- \end{pmatrix} = \frac{C_1 C_2 \ldots C_{N+1}}{t_1 t_2 \ldots t_{N+1}} \begin{pmatrix} E_{N+1}^+ \\ 0 \end{pmatrix} \tag{3.33}$$

with the amplitudes of the incident wave E_0^+, the reflected wave E_0^-, the transmitted wave after N layer E_{N+1}^+, and C_j the propagation matrix with the matrix elements:

$$C_j = \begin{pmatrix} \exp(-ik_{z,j}d_j) & r_{j-1}\exp(-ik_{z,j}d_j) \\ r_{j-1}\exp(ik_{z,j}d_j) & \exp(ik_{z,j}d_j) \end{pmatrix} \tag{3.34}$$

here, $k_{z,j}$ is the z-component of the wavevector at the interface between the (j - 1)-th and j-th layers, and t_j and r_j are the Fresnel transmission and reflection coefficients (introduced in Chapter 3.1.1), respectively.

By using equation 3.33 and 3.34 a convenient formula for the total reflection and transmission coefficients can be obtained. This formula corresponds to the amplitude reflectance $r(\alpha)$ and the transmittance $t(\alpha)$ (introduced in Chapter 3.1.1; equation 3.11 and 3.12) as follows:

$$r(\alpha) \equiv \frac{E_R}{E_I} = \frac{E_0^-}{E_0^+} = \frac{c}{a} \tag{3.35}$$

$$t(\alpha) \equiv \frac{E_T}{E_I} = \frac{E_{N+1}^+}{E_0^+} = \frac{t_1 t_2 \ldots t_{N+1}}{a} \tag{3.36}$$

where the quantities a and c are the matrix elements of the product of all Cj matrices:

$$C_1 C_2 ... C_{N+1} = \begin{pmatrix} a & b \\ c & d \end{pmatrix} \tag{3.37}$$

By considering the equations for the electromagnetic wave amplitudes at the boundaries, the wave amplitudes at an arbitrary depth *z* from the sample surface have to be obtained. Therefore equation 3.33 has to be divided in two parts:

$$\begin{pmatrix} E_0^+ \\ E_0^- \end{pmatrix} = \frac{C_1 C_2 ... C_{N+1}}{t_1 t_2 ... t_{N+1}} \begin{pmatrix} E_j^+ \\ E_j^- \end{pmatrix} \tag{3.38}$$

$$\begin{pmatrix} E_j^+ \\ E_j^- \end{pmatrix} = \frac{C_1 C_2 ... C_{N+1}}{t_1 t_2 ... t_{N+1}} \begin{pmatrix} E_{N+1}^+ \\ 0 \end{pmatrix} \tag{3.39}$$

where E_j^+ and E_j^-, correspond to the amplitudes of forward and backward propagating electromagnetic waves in the j-th layer, respectively. For convenience, the matrix D_j is defined as the product of $C_1 C_2 ... C_{N+1}$ is defined as:

$$D_j = C_{j+1} C_{j+2} ... C_{N+1} = \begin{pmatrix} a_j & b_j \\ c_j & d_j \end{pmatrix} \tag{3.40}$$

E_j^+ is expressed by the (1,1)-element a_j of the D_j matrix and E_{N+1}^+, and E_j^- by the (2,1) element c_j and E_{N+1}^+, as shown in the following equations:

$$E_j^+ = \frac{a_j}{t_{j+1} t_{j+2} ... t_{N+1}} E_{N+1}^+ \tag{3.41}$$

$$E_j^- = \frac{c_j}{t_{j+1} t_{j+2} ... t_{N+1}} E_{N+1}^+ \tag{3.42}$$

Implementing equation 3.36 leads to

$$E_j^+ = t_1 t_2 ... t_j \frac{a_j}{a} E_0^+ \tag{3.43}$$

$$E_j^- = t_1 t_2 ... t_j \frac{c_j}{a} E_0^+ \tag{3.44}$$

and the relationship between E_j^+, E_j^- and E_0^+ is achieved.

Finally, the amplitudes of the electromagnetic waves propagating in positive ($E^+(z)$) and negative ($E^-(z)$) direction with respect to the sample surface are expressed by the amplitudes at the interface E_j^+, E_j^- as

$$E^+(z) = E_j^+ \exp(ik_{z,j}\Delta z) \tag{3.45}$$

$$E^-(z) = E_j^- \exp(-ik_{z,j}\Delta z) \tag{3.46}$$

where Δz corresponds to the distance from the j-th boundary:

$$\Delta z = z - \sum_{i=1}^{j+1} h_i \tag{3.47}$$

Finally, the result can be implemented in the expression $I^{ill}(z,\alpha) = \left|E^+(z) + E^-(z)\right|^2$.

A typical illumination profile $I^{ill}(z,\alpha)$ below and close to the critical angle α_c is shown in Fig. 3-8. It can be observed that the spreading of the illumination profile rises when the incident angle increases and approaches to the critical angle α_c.

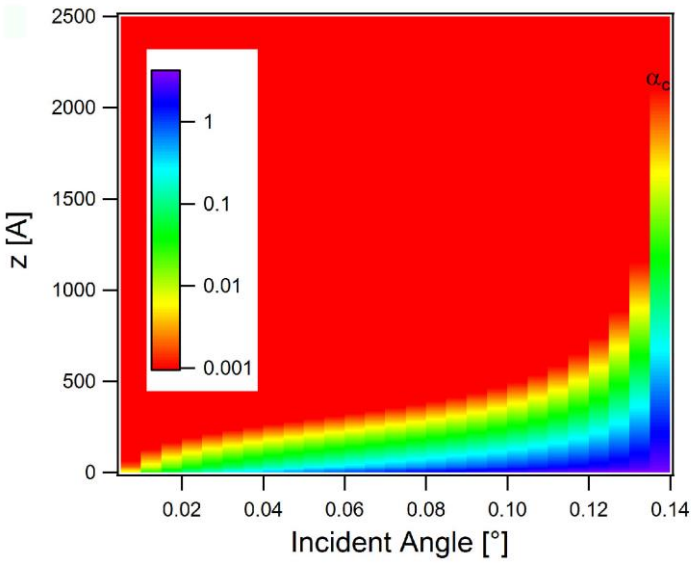

Fig 3-8: A typical illumination profile below and close to the critical angle α_c.

The concentration profile of the ion species

The concentration profile $c_i(z)$ of the ion species *i* at a depth *z* was parameterized as

$$c_i(z) = c_0 + c_{\max} \frac{\sqrt{e}\,(z - z_{HC})}{z_{\max}} \exp\left(-\frac{(z - z_{HC})^2}{2z_{\max}^2} \right), \qquad (3\text{-}48)$$

where c_0 is the bulk concentration, z_{HC} is the total thickness of the monolayer (obtained from XRR measurements, Chapter 3.1.1). Consequently, the ion distributions that possess a concentration maximum can be modeled with a smooth decay to the bulk concentration with only two free parameters: (i) the concentration maximum $c_{\max}$ and (ii) the z-position $z_{\max}$ of this maximum.[24] To refine the experimental results, the Levenberg-Marquardt nonlinear least squares optimization was used in this study.[39]

3.2.2. Protocol for combined XRR and GIXF measurements at the air/water interface

XRR and GIXF experiments were carried out at the beamline ID10B of the European Synchrotron Radiation Facility (ESRF, Grenoble). The lipid monolayers at the air/water interface were created as described in Chapter 2.4.1 and irradiated by a monochromatic synchrotron beam with an energy of 9 keV (λ = 1.38 Å). During the measurement the Langmuir film balance was kept in He atmosphere to reduce the absorption of fluorescence emission from air.

XRR was measured with a linear detector (Vantec-1, Bruker AXS, USA) by integrating the pixels near the specular plane, and the background was subtracted by integrating the intensity out of the specular plane (as described in appendix A.3). The reflectivity was analyzed as described in Chapter 3.1.2.

GIXF measurements were carried out at incident angles α_i below and above the critical angle of total reflection, $\alpha_c = 0.138°$. X-ray fluorescence signals from elements in the illuminated volume were recorded with an energy sensitive detector (Vortex, SII NanoTechnology, USA) and normalized by the detector counting efficiency. Subsequently, the intensities were normalized by the intensity of elastically scattered beam to compensate systematic differences between the experiments. In the last step, the fluorescence signals in the presence of monolayer were normalized by the signals from the blank buffer. This procedure avoids artefacts arising from the experimental geometry, such as the size of beam footprint and the fluorescence detector aperture.

3.3. Quartz crystal microbalance with dissipation (QCM-D)

3.3.1. Principle of the technique

The quartz crystal microbalance (QCM) is a technique using acoustic waves to monitor the mass of attached films with high sensitivity (1 ng/cm²).[40] The setup of QCM consists of a piezoelectric quartz disc, sandwiched between two electrodes (Fig. 3-9A).

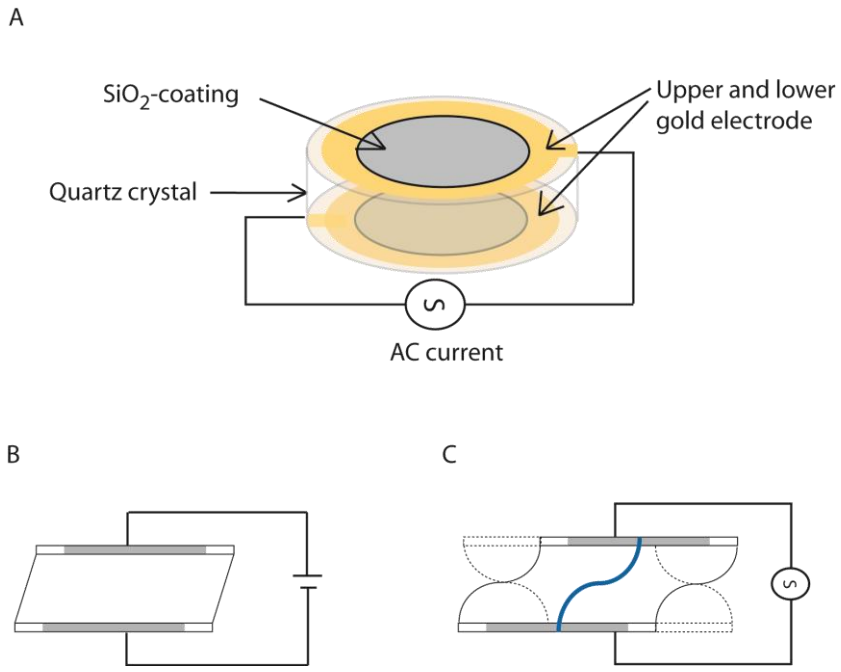

Fig. 3-9: Principle of the quartz crystal microbalance technique. (A) Schematic illustration of a SiO_2-coated quartz crystal sandwiched between two gold electrodes. (B) Application of an electric field leads to crystal deformation caused by its piezoelectricity. (C) Alternating current (AC current) across the AT-cut crystals drives them to oscillate in shear mode. The blue curve corresponds to the standing wave generated by applying the fundamental resonance frequency of the crystal.

By using the inverse piezoelectric effect of the quartz crystal an application of voltage leads to a crystal deformation (Fig. 3-9B) which can be cyclical if the applied voltage is alternating (Fig. 3-9C). Consequently, alternating current can drive the crystal to oscillate at its resonance frequency (or multiples of it, the so-called overtones) and a standing wave is generated inside the crystal (blue curve in Fig. 3-9C). The crystal used in QCM is an AT-cut quartz crystal with oscillation occurring in a thickness shear mode, where the two quartz surfaces are located at the antinodes of a standing wave.

The wavelength of the standing shear wave is defined by the crystal thickness d_q and the overtone order n:

$$\lambda_n = \frac{2d_q}{n} \tag{3.49}$$

This leads to the resonance frequency f_n given as:

$$f_n = \frac{nv_q}{2d_q} \tag{3.50}$$

where v_q is the shear wave velocity in quartz. By implementing the values for v_q = 3340 m/s and d = 0.033 cm in equation 3.50 the calculated fundamental frequency for the quartz crystal f_1 is 5 MHz.

Sauerbrey approximation

The application of QCM as mass-sensitive tool results from the findings of Sauerbrey in 1959 where it is concluded that a thin layer of thickness d_f is going to increase the thickness and the mass per unit area of the quartz crystal by Δd and Δm, respectively.[40]

As consequence the adsorption of a thin layer on the top electrode shifts the antinode of the standing wave further up (Fig. 3-9C). This shift induces a increase in wavelength and therefore a decrease of the frequency. The change in the resonance frequency of the crystal before and after thin layer adsorption, Δf_n, is then directly proportional to the mass of the thin layer Δm:

$$\Delta f_n = -\frac{\Delta d}{d_q} f_n = -\frac{\Delta m}{\rho_q d_q} f_n = -n\frac{2 f_1^2}{\rho_q v_q}\Delta m \tag{3.51}$$

where the density of quartz is given as ρ_q.

Considering the use of an AT-Cut quartz crystal with a fundamental frequency f_1 of 5 MHz, a density ρ_q of 2.65 g/cm^{-3} and a shear wave velocity v_q of 3340 m/s the mass sensitivity constant of quartz C = 17.7 ng/cm²Hz could be obtained and the Sauerbrey equation can be written as:

$$\Delta f_n = -\frac{n}{C}\Delta m \tag{3.52}$$

In Sauerbrey´s approximation the adsorbed thin layer has acoustic properties comparable to the quartz crystal. Therefore equation 3.52 is only valid if (a) there is no slip between the adsorbed layer and the crystal, (b) the distribution of the adsorbed mass at the crystal surface is homogeneous and (c) the attached layer is rigid. An adlayer is defined as rigid if no viscoelastic deformation occurs, independently from the measurement environment (in air or in liquids).

Dissipation factor *D*

The viscoelastic properties of the adlayer can be obtained by investigating the loss of energy originated from the contact of the sensor crystal (or the adsorbed thin layer) with the surrounding medium (air or liquid). In the so-called "ring-down" scheme developed by Rodal et al, the external driving voltage is turned off intermittently which leads to a decay of the shear-wave oscillation caused by the energy loss.[41] This approach is used in quartz crystal microbalance with dissipation (QCM-D) measurements, where the loss of energy (or decay of shear-wave oscillation) is represented as the dissipation factor *D*.
This dissipation factor is defined as the inverse of the quality factor *Q*:[41]

$$D = \frac{1}{Q} = \frac{E_{Diss}}{2\pi E_{stored}} \tag{3.53}$$

where E_{Diss} corresponds to the dissipated energy during one cycle of oscillation and E_{stored} is the total energy stored in the crystal.
If the attached film is highly viscoelastic, it cannot follow the oscillation of the crystal in the medium due to its different viscosity and elasticity. In fact, this viscoelasticity enhances the dissipated energy and therewith the dissipation factor *D*.
In addition, the adsorption of viscoelastic material can change the oscillation frequency *f* which is inversely proportional to the dissipation factor *D*:

$$D = \frac{1}{\pi f \tau} \tag{3.54}$$

where τ corresponds to the decay time constant of the oscillation.
Considering these effects, an adsorbed layer is defined as rigid if the change in dissipation after its adsorption ΔD is $<1 \times 10^{-6}$ for a frequency change Δf of ~ -10 Hz.[25,42,43]

The output signal

In practice, the resonance frequency *f* and the dissipation factor *D* are measured contemporaneously. After the driving voltage is turned off a sinusoidal wave is recorded which decays exponentially with time due to the damping by a medium. The exponentially decay of the amplitude at time *t*, A(t), is given as:

$$A(t) = A_0 e^{-t/\tau} \sin(2\pi ft + \psi) \tag{3.55}$$

where A_0 corresponds to the amplitude at time t=0, τ to the time constant of the oscillation, and ψ the phase angle.
Furthermore equation 3.54 can be implemented in equation 3.55:

$$A(t) = A_0 e^{-\pi Dft} \sin(2\pi ft + \psi) \tag{3.56}$$

Accordingly, the resonance frequency *f* and the dissipation *D* can be extracted simultaneously by fitting the decay curve.

3.3.2 Protocol for QCM-D measurements

The QCM-D data were recorded using a D 300 from Q-Sense (Gothenburg, Sweden). To prevent mechanical damage to the SiO_2-coated QCM-D crystals, the RCA cleaning method was avoided. Instead, the crystals were cleaned in 10 mM sodium dodecyl sulfate (SDS), rinsed in water, and put in a UV/ozone chamber for 20 min prior to use. All measurements were recorded at the third overtone (15 MHz) throughout the study. Furthermore, all the data were normalized to the fundamental frequency (5 MHz) by dividing the result with the overtone number (3). After establishing a baseline in HBS buffer, suspensions of SOPC vesicles incorporating 1, 2 or 5 mol% DOGS-NTA were injected into the measurement chamber. After washing away non-bound vesicles with at least 10 ml HBS, the change in frequency and dissipation reached a steady state at Δf ~ - 26.0 Hz and ΔD ~ 0, respectively. This is in very good agreement with previously reported values,[44] confirming the formation of a planar lipid bilayer. The Xcad-11 functionalization of supported membrane on the QCM-D crystals was done inside the measurement chamber with the procedure described in Chapter 2.5.4.

3.4. Optical techniques

3.4.1. Fluorescence microscopy

Fluorescence microscopy setup

Fluorescence microscopy was used (a) to confirm the viability of animal caps, (b) to gain an experimental evidence of the neural crest induction on supported membranes (Chapter 5) and (c) to observe the lateral movement and accumulation of fluorescently labeled proteins in membrane electrophoresis experiments (Chapter 6).

For animal cap *in vivo* and electrophoresis experiments, an Axiovert 200 inverted microscope (Carl Zeiss, Göttingen, Germany) equipped with either an LD Achroplan 20x/0.40 air objective (Carl Zeiss, Göttingen, Germany) or an ELWD PlanFluor 20x/0.45 air objective (Nikon, Tokio, Japan) and suitable filter sets, was used. The sample was illuminated using a X-cite®120Q PC mercury lamp (EXFO,Mississauga, Canada) and images were recorded with an Orca ER CCD-camera (Hamamatsu Photonics, Herrsching, Germany). The acquisition software was Hokawo version 2.1 (Hamamatsu Photonics, Herrsching, Germany) and the images were analyzed with ImageJ 1.44p (Wayne Rasband, National Institutes of Health, USA).

Confocal microscopy images of animal tissue sheets were taken at the Karlsruhe Institute of Technology (KIT, Karlsruhe, Germany) with an Axio Observer Z1 (Carl Zeiss AG, Jena, Germany) featured with either a C-ApoChromat 63x/1.2 water-immersion objective or an LD LCI Plan-ApoChromat 25x/0.8 water-immersion objective, a spinning disc unit (Yokogawa Electric Corporation, Tokyo, Japan) and an AxioCam MRm camera (Carl Zeiss AG, Jena, Germany).

3.4.2. Principle of the reflection interference contrast microscopy (RICM)

Introduction

Reflection interference contrast microscopy (RICM) is a microinterferometric technique utilizing the local difference in the optical path lengths between interfering waves which have been reflected at different interfaces. This technique is suited to study object-substrate interactions and wetting phenomena such as vesicle or cell adhesion. The first qualitative studies on cell adhesion with RICM were realized by Abercrombie et al. [45] and Curtis et al. [46] in 1958 and 1964, respectively, where quantitative analysis was still limited. Improvements were carried out by Ploem et al., who invented the Antiflex technique in 1975 to increase the contrast.[47] Gingell, Todd and Heavens developed the theoretical analysis further to enable quantitative measurements.[48] Furthermore Sackmann and co-workers were the first to apply RICM extensively to surfaces with defined optical properties (e.g. colloidal beads, supported lipid monolayer and lipid bilayer in vesicles) and achieved a quantitative interpretation of the obtained images.[48,49]

The key principle of the label-free technique bases on recording interference patterns caused by the reflection of polarized light at interfaces with different refractive index. The observed intensity variations correspond directly to the distance $h(x,y)$ between surface-near cell membranes and the sample substrate. The lateral resolution is limited to ~ 0.27 µm whereas the interferometric effect helps to decrease the vertical resolution for optical defined objects down to 5 nm.

Reflection Interference Contrast Microscopy Setup

The adhesion of animal cap tissue sheets was monitored by RICM. Images were recorded with the same Axiovert 200 inverted microscope and camera as used for fluorescence microscopy experiments. Fig. 3-10 illustrates the optical light path and key elements of the RICM technique. To extract a monochromatic wavelength of 546 nm (± 12 nm) from the X-cite®120Q PC mercury lamp an appropriate green band pass filter was used. The microscope was equipped with a PlanNeofluar 63x/1.25 Antiflex oil-immersion objective (Carl Zeiss, Göttingen, Germany) which is features with a built-in lambda quarter plate. In combination with a polarizer and an analyzer in the illumination and detection path, respectively, the

Antiflex setup for contrast enhancement is realized. After the incident beam passes the polarizer, the linearly polarized light passes the objective and subsequently the lambda quarter plate. This changes the polarization from linear to circular and allows for a phase shift of the incident beam at all interfaces in the sample. As the light is reflected in the sample and passes the lambda quarter plate a second time, its polarization is converted from circular to linear again. Yet, this time the polarization direction is perpendicular to the incident beam. The analyzer placed shortly before the detector then transmits only the light being reflected from the sample while blocking almost all of the scattered light.

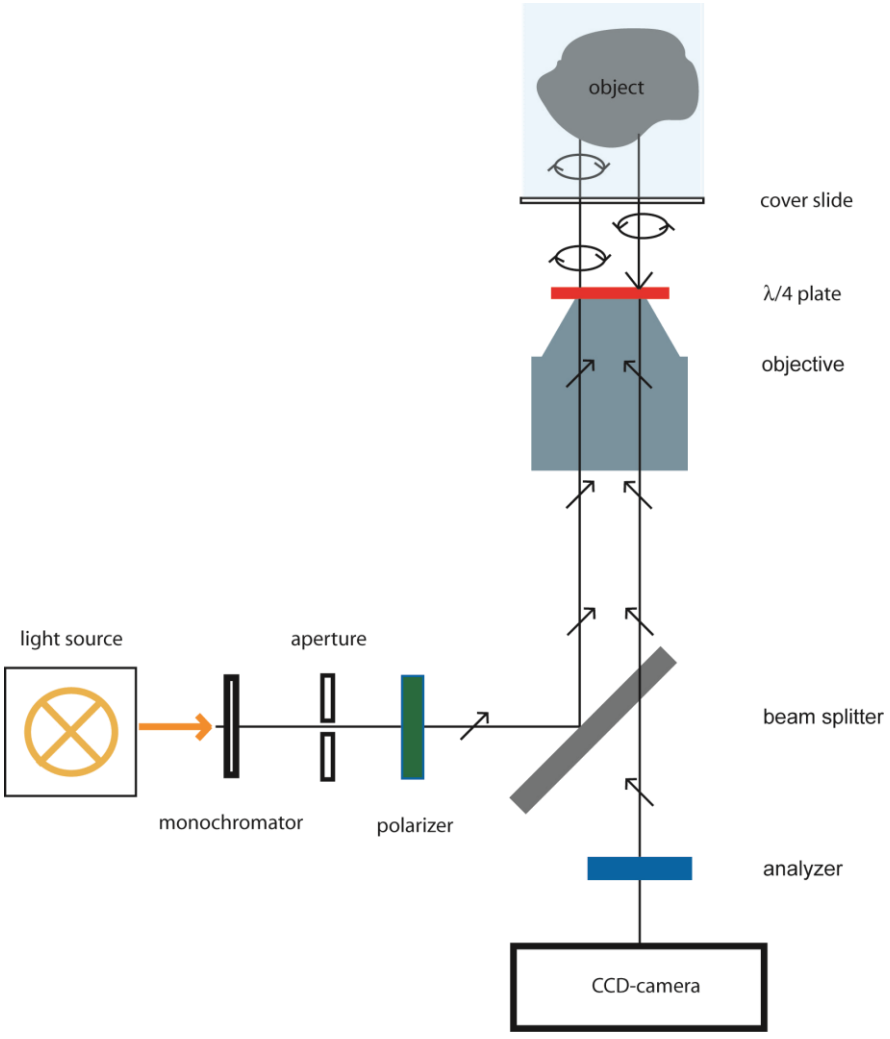

Fig. 3-10: RICM setup containing additional optical elements of the antiflex technique for contrast enhancement. These three elements are: polarizer (green), lambda quarter plate (red) and analyzer (blue).

Measurement of object to substrate distances for perpendicular incident light and two reflecting interfaces.

Fig. 3-11 shows a sketch of the reflection interference geometry for cells close to the surface and two reflecting interfaces.

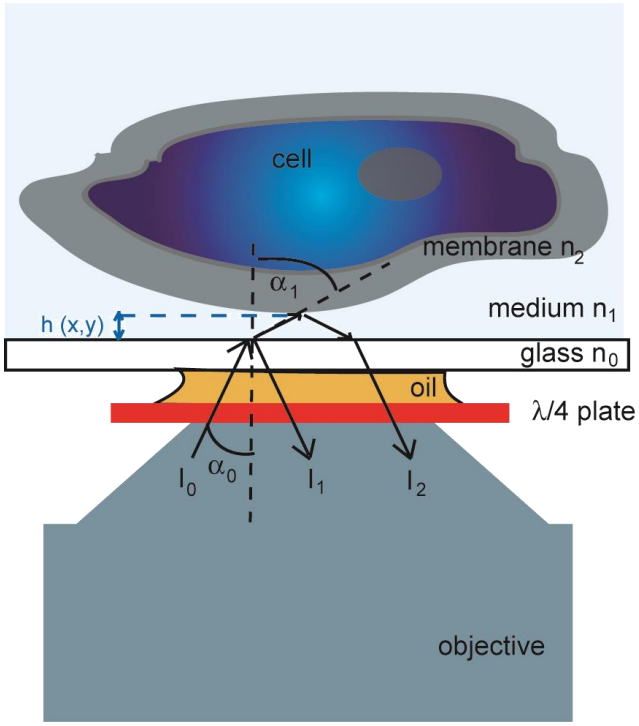

Fig. 3-11: Schematic illustration of the reflection interference geometry for a cell close to the surface and two reflecting interfaces.

A monochromatic incident ray, I_0, is partly reflected at the glass/medium interface resulting in ray I_1 and partly transmitted. The transmitted ray is reflected at the medium/cell membrane interface which leads to ray I_2.

Knowing the refractive indices of all reflecting interfaces, the Fresnel reflection coefficients in the limit of perpendicular light (incident angle $\alpha_0 = 0$) approximate to:

$$r_{i,j} = \frac{n_i - n_j}{n_i + n_j} \text{(i,j = 0,1,2; i} \neq \text{j)} \qquad (3.57)$$

These reflection coefficients also define the intensities I_1 and I_2 for the incoming light I_0:

$$I_1 = r_{01}^2 I_0 \,;\; I_2 = \left(1 - r_{01}^2\right)^2 r_{12}^2 I_0 \tag{3.58}$$

These rays interfere constructively or destructively depending on the optical path difference $\Delta = h(x,y)n_1$, where $h(x,y)$ is the cell membrane to substrate distance and n_1 corresponds to the refractive index of the medium. With $I(x,y) = R^* R I_0$, the reflection coefficient $R = r_{01} + (1 - r_{01}^2) r_{12} \exp(-i2k\Delta_i)$ and $k = 2\pi/\lambda$ this yields: [50]

$$I(x,y) = I_1 + I_2 + 2\sqrt{I_1 I_2}\cos\left[\frac{4\pi n_1}{\lambda} h(x,y) + \varphi\right] \tag{3.59}$$

where λ is the wavelength of the incident ray, n_1 the refractive index of the medium, and φ the phase shift, which is close to π.

Equation 3.59 can be simplified by implementing the sum S and difference D of the maximal intensity $I_{max} = I_1 + I_2 + 2\sqrt{I_1 I_2}$ and the minimal intensity $I_{min} = I_1 + I_2 - 2\sqrt{I_1 I_2}$ to:

$$I(x,y) = \frac{1}{2}\left[S + D\cos\left[\frac{4\pi n_1}{\lambda} h(x,y) + \varphi\right]\right] \tag{3.60}$$

Rearranging this equation and using $\varphi = \pi$, the simplified height profile can be calculated according to:

$$h(x,y) = \frac{\lambda}{4\pi n_1}\arccos\left[\frac{S - 2I(x,y)}{D}\right] \tag{3.61}$$

Measurement of object to substrate distances for partially coherent incident light

Up to now, only perpendicular incident light has been considered and any incoherence from the divergence of the incident beam was not accounted for. But since cell adhesion experiments are usually recorded with an open aperture (see below) and therefore higher beam divergence, different degrees of coherence arise which modify the recorded interferogram. In the theory of partial coherence the mutual degree of coherence, $\Gamma_{12}(x,y)$, is introduced and equation 3.61 changes to:

$$h(x,y) = \frac{\lambda}{4\pi n} \arccos\left[\frac{S - 2I(x,y)}{D\Gamma_{12}(x,y)}\right] \tag{3.62}$$

The shape and width of the mutual degree of coherence $\Gamma_{12}(x,y)$ is given by the point spread function parallel to the optical axis. According to Debye the three-dimensional intensity function near the focus can be written as an Airy pattern Γ_{12}:[51]

$$\Gamma_{12} = \frac{\sin(\beta)}{\beta} e^{i\beta}, \text{ with } \beta = \frac{4\pi}{\lambda} h(x,y) \sin^2\left(\frac{\alpha}{2}\right) \tag{3.63}$$

where α is the illumination aperture angle. For fully coherent light $\Gamma_{12}(x,y) > 0.88$, while partially coherent light is defined for $0.88 > \Gamma_{12}(x,y) > 0.15$.

From this relation, it is clear that the degree of coherence Γ_{12} can be directly modulated with the aperture diaphragm. As the aperture is opened the illumination numerical aperture INA = $n_1 \times \sin(\alpha)$ is increased and higher lateral resolution is achieved. At the same time, an open aperture reduces the depth of focus and thereby the contrast.

In other words, the degree of coherence limits the lateral resolution Δx, either due to the Rayleigh criterion (given by $0.61\,\lambda$ / NA; NA = numerical aperture) for a closed aperture (more coherent light), or due to an the INA for an open aperture (rather incoherent light): [52]

$$\frac{0.61\lambda}{NA} \geq \Delta x \geq \frac{0.5\lambda}{INA} \tag{3.64}$$

In this thesis an open aperture was used due to its advantages in cell adhesion measurements. The main advantages are the improvement of the lateral resolution and the avoidance of reflections at multiple interfaces caused by the heterogeneity of refractive indices inside the cell. This heterogeneity of the refractive index is due to cell organelles with unknown optical properties and makes it difficult to measure the distances between cells and substrate in a quantitative manner. Furthermore, in the study of animal cap cell adhesion, cohesive cell layers were observed which did not allow for the determination of the background intensity. Thus the real intensity of the first maximum (I_{max}) and the first minimum (I_{min}) could not be determined. A calculation of the membrane-substrate distance was hence not possible.

Instead, cell-substrate contact areas, i.e. darker regions which were enclosed by interference fringes, were analyzed. Such fringes were typically observed at the curved region toward the cell edge. Within this region the intensity was usually very low whenever an apparently strongly adhering cell was monitored. Therefore, it was assumed that the detection of low intensities corresponded to small cell-substrate distances. The detailed definition of adhesion is described in Chapter 5.2.1.

3.4.3. Protocol for RICM experiments

In order to model developmental processes, animal caps explanted from African clawed frog (*Xenopus laevis*) embryos placed on functionalized supported membranes were investigated. For this, the formation of neural crest cells (NCC) was chosen as the developmental process to be monitored. The NCC formation was induced by injection of truncated bone morphogenetic protein receptor (300 pg; tBR) and *Xenopus* Frizzled 7 (500 pg; XFz7) as mRNA into one blastomere of a *Xenopus laevis* embryo at the two-cell stage. At the same stage, a cell membrane tracer (500 pg; GAP43-GFP RNA (Chapter 5.3 and 5.4) or GAP43-mCherry RNA (Chapter 5.5)) to visualize cell membranes, as well as an additional reporter (*slug*-promoter-GFP) used to gain experimental evidence of neural crest induction on supported membranes, was co-injected.

Furthermore, for control experiments, induced animal caps without Xcad-11 (Xcad-11 MO animal cap) were created by injecting antisense Xcad-11 morpholinos at two-cell stage, which leads to the blocking of the natural Xcad-11 synthesis in neural crest induced animal caps.

The animal cap (approximately 0.4 × 0.4 mm) was cut from the blastocoel roof of the *Xenopus* embryo when it reached blastula stage (stage 8 to 9), seeded with their inner blastocoelic surface facing to the funcionalized supported membrane and fixed by a cover glass to prevent the rolling up. The supported membrane with or without the adhesion molecule *Xenopus* cadherin 11 (Xcad-11) was built by vesicle fusion (Chapter 2.4.3) in a 2-well chamber (Chapter 2.3).

3.5. Fluorescence recovery after photobleaching (FRAP)

3.5.1. Principle of the technique

Fluorescence recovery after photobleaching (FRAP) is a standard method to investigate the mobility and passive lateral diffusion of molecules in a lipid bilayer.
The lateral diffusion is expressed by the diffusion coefficient, which is generally described by the Einstein relation: [53]

$$D = \frac{k_B T}{f} \tag{3.65}$$

where k_B is the Boltzman constant, T is the absolute temperature and f is the friction coefficient. f depends on the radius of the diffusive molecule R and on the viscosity of the fluid. In case of proteins embeded in a lipid membrane, Saffmann and Delbrück showed that the diffusion coefficient is limited by the effect of the liquid surrounding the membrane.[54] In the so-called Saffman-Delbrück model, a lipid membrane is described as a thin layer of viscous fluid with the viscosity η_m, surrounded by a less viscous bulk liquid with the viscosity η_l. Here, the relation for D is given as: [54]

$$D = \frac{k_B T\left(\ln\left(\frac{\eta_m h}{\eta_l R}\right) - \gamma\right)}{4\pi\eta_m h} \tag{3.66}$$

where h corresponds to the membrane thickness and γ to the Euler-Mascheroni constant (≈ 0.577). In the case of a lipid membrane surrounded by a highly viscous material (e.g. supported membranes), Evans and Sackmann described the diffusion coefficient to be: [55]

$$D = \frac{k_B T}{\pi b_c R^2} \tag{3.67}$$

where b_c is the friction coefficient between the membrane and the support.

To measure the diffusion by FRAP, a strong laser bleaches the fluorescent molecules (e.g. fluorescent labelled lipids) in a well-defined area. In this bleached region, the fluorescence recovers by passive diffusion. Consequently, the diffusion coefficient as well as the mobile fraction of the fluorescent molecules can be determined in a quantitative manner.

If the bleaching beam is circular and homogenous the recovery of the fluorescence intensity $F(t)$ can be described as: [56,57]

$$F(t) = F(\infty) - (F_0 - F(0))\left\{1 - \exp\left(-\frac{2\tau}{t}\right)\left[I_0\left(\frac{2\tau}{t}\right) - I_1\left(\frac{2\tau}{t}\right)\right]\right\} \qquad (3.68)$$

where F_0 is the initial fluorescence intensity, $F(0)$ is the intensity directly after bleaching (t=0), and $F(\infty)$ is the intensity reached in equilibrium state. These three fluorescence intensities are illustrated in Fig. 3-12.

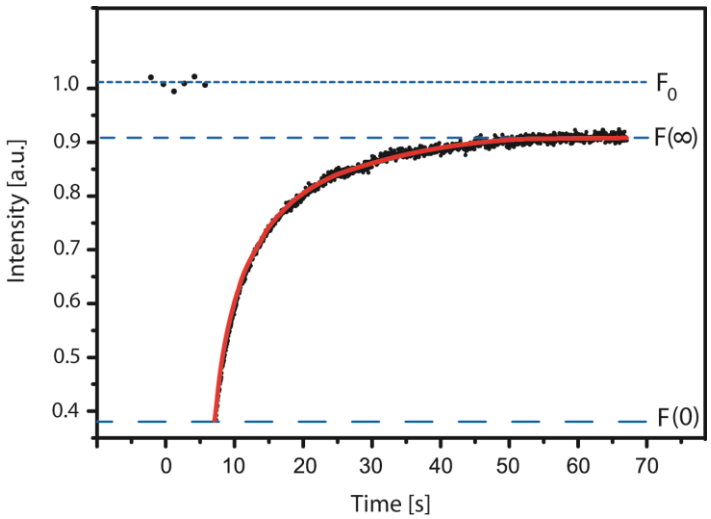

Fig 3-12: Typical example of a fluorescence recovery curve after photobleaching. The blue dashed lines correspond to different fluorescent intensities. Here, F_0 is the initial fluorescence intensity, $F(\infty)$ is the intensity reached in equilibrium state , and $F(0)$ is the intensity directly after bleaching (t=0). The red line corresponds to the fit obtained by using equation 3.68.

I_0 and I_1 are modified Bessel functions of zero and first order. By fitting the expression given in equation 3.68 to the recorded intensities (red line in Fig. 3-12), the characteristic time constant τ can be obtained. By knowing τ and the diameter of the bleached spot r, the diffusion coefficient D can be calculated as following:

$$D = \frac{r^2}{4\tau} \qquad (3.69)$$

The mobile fraction or recovery rate R can be calculated as follows:

$$R = \frac{F(\infty) - F(0)}{F_0 - F(0)} \qquad (3.70)$$

3.5.2. Protocol of FRAP experiments

Fluorescence recovery after photobleaching (FRAP) was utilized to investigate the mobility and the passive lateral diffusion of Alexa Fluor 633 streptavidin, linked to Biotinyl Cap DOPE, and NBD-DHPE in a supported lipid bilayer consisting of 98.5 mol% DMPC, 1 mol% NBD-DHPE, and 0.5 mol% Biotinyl Cap DOPE.

FRAP measurements were performed at Nikon Imaging Center (NIC, Heidelberg, Germany) by utilizing a spinning disk confocal microscope (Perkin Elmer, USA). The microscope includes an inverted microscope (Nikon TE-2000), a confocal scanning unit (Yokagawa CSU-22) and an EMCCD camera (Hamamatsu C9100-02). Furthermore, the setup is equipped with five excitation laser lines (wavelength: 405, 440, 488, 515 and 561 nm) and a 60x oil immersion objective (Nikon Plan Apo VC 60x NA 1.4). Prior to the FRAP experiment, the sample environment temperature was set to 37 °C by an environmental box encasing the microscope. This is important to ensure the experimental temperature to be higher than the transition temperature of the matrix lipid DMPC (T_m DMPC = 23 °C).

To bleach the fluorescent protein or lipid, the beam was focussed onto the sample through a pinhole with a diameter of 8.9 µm. After a short bleaching pulse (typically 50 - 300 ms) the photoactivity of the molecules in the illuminated area was destroyed and the subsequent fluorescence recovery was monitored by recording a video. In order to exclude bleaching effects during the recovery, the extracted recovery curve was normalized to a reference curve (extracted from a not previously bleached area, see Fig. 3-13A) as illustrated in Fig. 3-13.

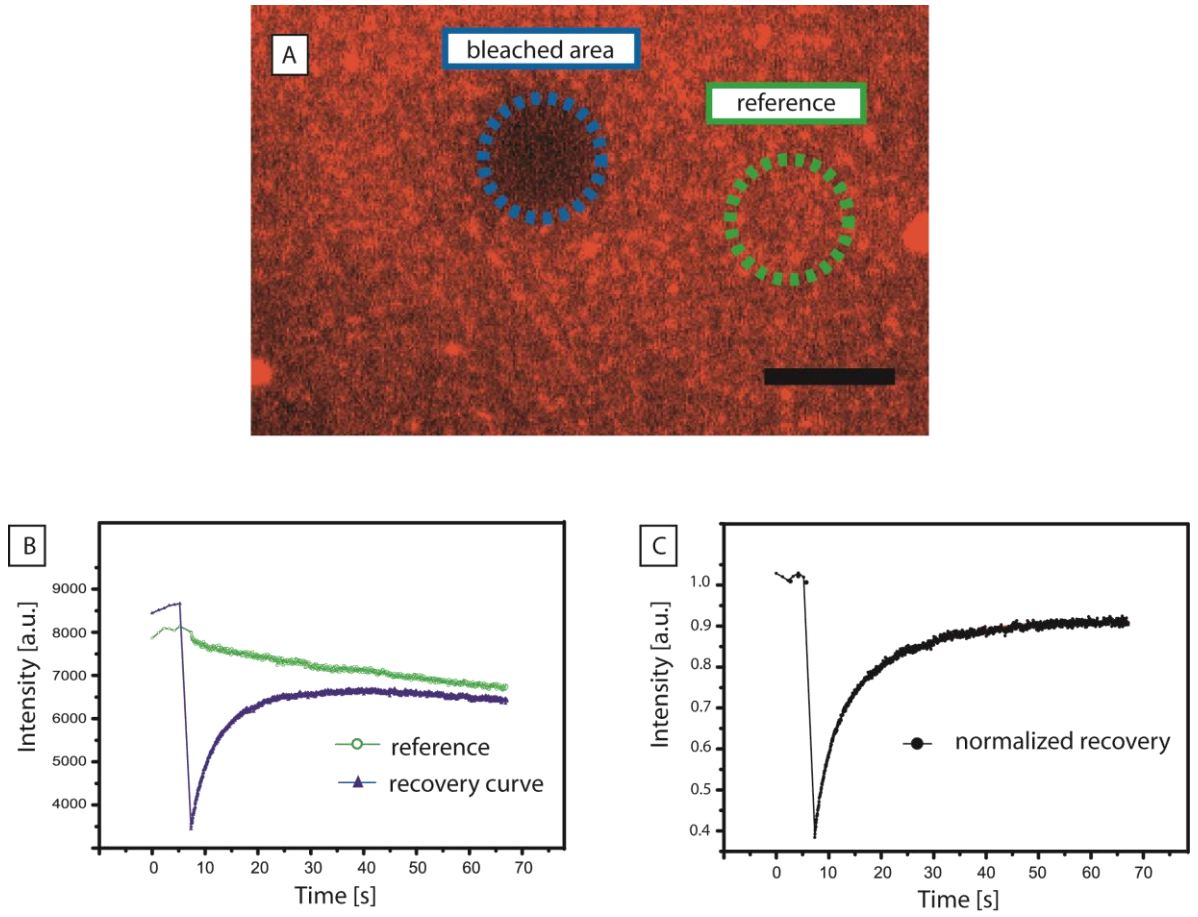

Fig. 3-13: Normalization of the fluorescence recovery after photobleaching curve. (A) Fluorescence microscopy image of the supported membrane functionalized with Alexa Fluor 633 streptavidin. The bleached area is highlighted in blue and the area measured as reference is labelled in green. The scale bar corresponds to 12 µm. (B) The recorded recovery curve (blue) and the reference fluorescence intensity (green) measured at the same time. (C) The normalized recovery curve.

3.6. Membrane electrophoresis

3.6.1. Principle of the technique

Electrophoresis allows for the lateral separation and accumulation of charged amphiphilic molecules (e.g. phospholipids) in a two-dimensional fluid (e.g. supported membrane) by application of an electric field parallel to the surface. Moreover, this method can be utilized to generate electric-field induced concentration gradients of lipids in supported membrane. This is called "membrane" electrophoresis. The electrophoretic mobility of lipids and proteins coupled to lipids moving in a supported membrane is theoretically described in this chapter.

Electrophoretic mobility

Considering a two-dimensional fluid (e.g. supported membrane), the passive diffusion is simply driven by a concentration gradient and can be written as:

$$\frac{\partial c(x,t)}{\partial t} = D\frac{\partial^2 c(x,t)}{\partial x^2} \tag{3.71}$$

where *c(x,t)* is the concentration of the molecule at the position *x* (between two diffusion barriers) and at the timepoint *t*, and *D* corresponds to the passive diffusion coefficient.
If an electric field is applied between the diffusion barriers, this equation is expanded by a term containing the mean drift velocity $<v>$ in the direction of the electric field: [58]

$$\frac{\partial c(x,t)}{\partial t} = D\frac{\partial^2 c(x,t)}{\partial x^2} + < v > \frac{\partial c(x,t)}{\partial x} \tag{3.72}$$

In the steady-state, the time-dependent term can be eliminated leading to a homogenous second order differential equation:

$$0 = D\frac{\partial^2 c(x,t)}{\partial x^2} + < v > \frac{\partial c(x,t)}{\partial x} \tag{3.73}$$

In this equation the diffusional flux of the molecules $D\frac{\partial^2 c(x,t)}{\partial x^2}$ is balanced by the electrical flux in the opposite direction, $< v > \frac{\partial c(x,t)}{\partial x}$. Solving this equation gives the exponential solution:

$$c(x) = A\exp\left(\frac{x}{\xi}\right) + B \tag{3.74}$$

where the constants *A* and *B* are the amplitude and the integration term, respectively. ξ is the characteristic decay length of the exponential accumulation at the barrier. Inserting this result into equation 3.73 yields:

$$< v >= \frac{D}{\xi} \tag{3.75}$$

Consequently, the mean drift velocity caused by the electric field <*v*> can be calculated by using the characteristic decay length ξ and the passive diffusion coefficient *D* (obtained in a separate FRAP measurement).

The mean drift velocity <*v*>, representing the electrophoretic mobility, is not only determined by the net charge per molecule, but in addition by the fact that the application of an electric field leads to a bulk flow of the ions above the substrate (= electroosmosis).

Mobility of proteins linked to a supported membrane

In the following, the mobility of a protein linked to an anchor lipid in a supported membrane is described theoretically. Unlike a lipid, proteins linked to lipids protrude far out from the supported membrane and are hence deeply immersed in the bulk flow. Therefore, the contribution of the electroosmotic effects to the electrophoretic mobility is increased. In general three contributions to the net force acting on the protein are considered, as illustrated in Fig. 3-14.

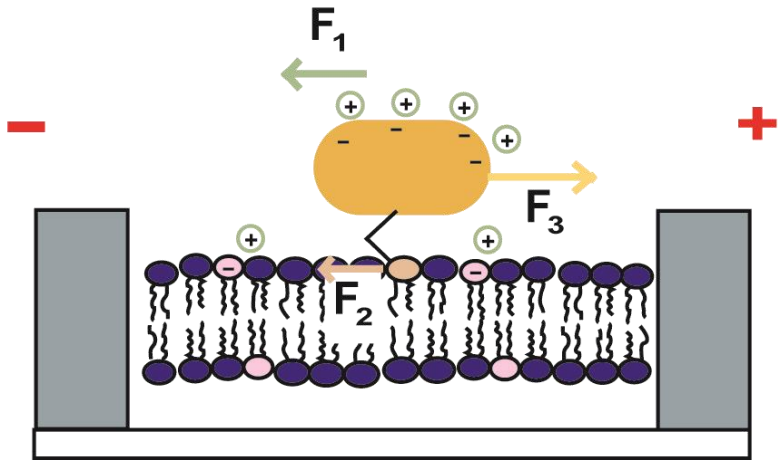

Fig 3-14: Schematic illustration of the forces contributing to the the net force acting on a linked protein. The three forces are the Stokes force (F1), Stokes drag (F2) and the force exerted on the protein by the application of the electric field (F3).

The first one is the Stokes force (F1 in Fig. 3-14), from the ion flow adjacent to the supported membrane and acting on the protein (assumed to be spherical) with the radius R_P:

$$F_1 = 6\pi\mu_{water}R_P(v - v_1) \tag{3.76}$$

here, v_1 corresponds to the velocity of the protein relative to the supported membrane, μ_{water} is the viscosity of water, and v is the ion flow velocity adjacent to the supported membrane surface given by the Helmholtz-Smoluchowski equation: [59]

$$v = \frac{\varepsilon_r \varepsilon_0 \zeta_l E}{\mu_{water}} \tag{3.77}$$

where ε_r is the dielectric constant of the aqueous phase (~ 80), ε_0 is the permittivity of free space, ζ_l is the zeta potential of the supported membrane surface, and E is the strength of the electric field.

The second Force is the Stokes drag (F2 in Fig. 3-14) acting from the anchor lipid:

$$F_2 = -6\pi\mu_l R_l v_1 \tag{3.78}$$

where μ_l is the viscosity of the supported membrane and R_l corresponds to the radius of the anchor lipid in the supported membrane.

Finally the third force (F3 in Fig 3-14), is exerted on the protein by the application of the electric field:

$$F_3 = 6\pi R_P \varepsilon_r \varepsilon_0 \zeta_P E \tag{3.79}$$

with ζ_p corresponding to the zeta-potential of the protein.

In the steady-state the sum of these three forces is zero. Consequently, the drift velocity of the protein relative to the supported membrane v_1 can be written as following: [60]

$$v_1 = \frac{\varepsilon_r \varepsilon_0 R_P (\zeta_P - \zeta_l) E}{R_P \mu_{water} + R_l \mu_l} \tag{3.80}$$

3.6.2. Protocol of membrane electrophoresis experiments

As the first step, a supported membrane, consisting of 98.5 mol% DMPC, 1 mol% DOGS-NTA, and 0.5 mol% Biotinyl Cap DOPE, was built onto glass substrates (see Chapter 2.2.2) by vesicle fusion and functionalized with Alexa Fluor 633 streptavidin (as described in Chapter 2.5.4). Afterwards the patterned, functionalized substrate was transferred from the "preparation" chamber (Chapter 2.3) to a trough filled with 1 mM citrate buffer (pH = 5.2) and placed between two cover slides. This cover slide sandwich was mounted in the membrane electrophoresis chamber shown in Fig. 3-15.

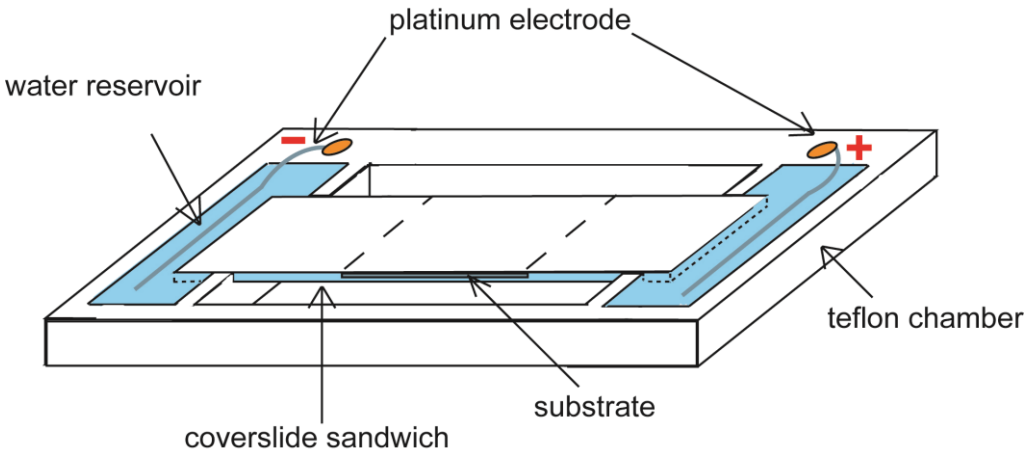

Fig. 3-15: Schematic illustration of the membrane electrophoresis chamber. The patterned substrate (24 x 24 mm, here shown in grey) with the supported membrane is sandwiched between two larger (24 x 50 mm) coverslides.

After the connection between the two water reservoirs and the contact to the buffer layer inside the cover slide sandwich is granted a tangential electric field of 10 V/cm was applied. The observation of the movement and accumulation of fluorescent proteins was done by mounting the membrane electrophoresis chamber on an Axiovert 200 inverted microscope (described in Chapter 3.4). It has to be noted that the temperature of the sample environment was kept around 37 °C to ensure that the experiments were performed above the transition temperature of the matrix lipid DMPC (T_m DMPC = 23 °C) and that the supported membrane exhibits high lateral fluidity.

After approximately 30 min, a static concentration profile was reached, the electric field was turned off , and the sample was immediately transferred to 4 °C cold HBS-buffer in order to freeze the gradient (< 23 °C = T_m DMPC).

In the last step, His-GFP was linked to DOGS-NTA, which moved towards the opposite direction of the Alexa Fluor 633 streptavidin during membrane electrophoresis. The NTA-groups were saturated with Ni^{2+} ions by addition of 20 mM Ni-HBS buffer (pH =7.4), rinsed with HBS buffer, and afterwards incubated with a 10 µg/ml His-GFP solution for at least 2 hours. Finally, after washing the unspecific bound proteins away, the sample was ready to image. Here, it is important that all the steps after membrane electrophoresis are done below the transition temperature, T_m, of DMPC (= 23 °C) in order to keep the gradient stable.

The procedure of developing two oppositely oriented protein gradients on patterned supported membranes is illustrated in Fig. 3-16.

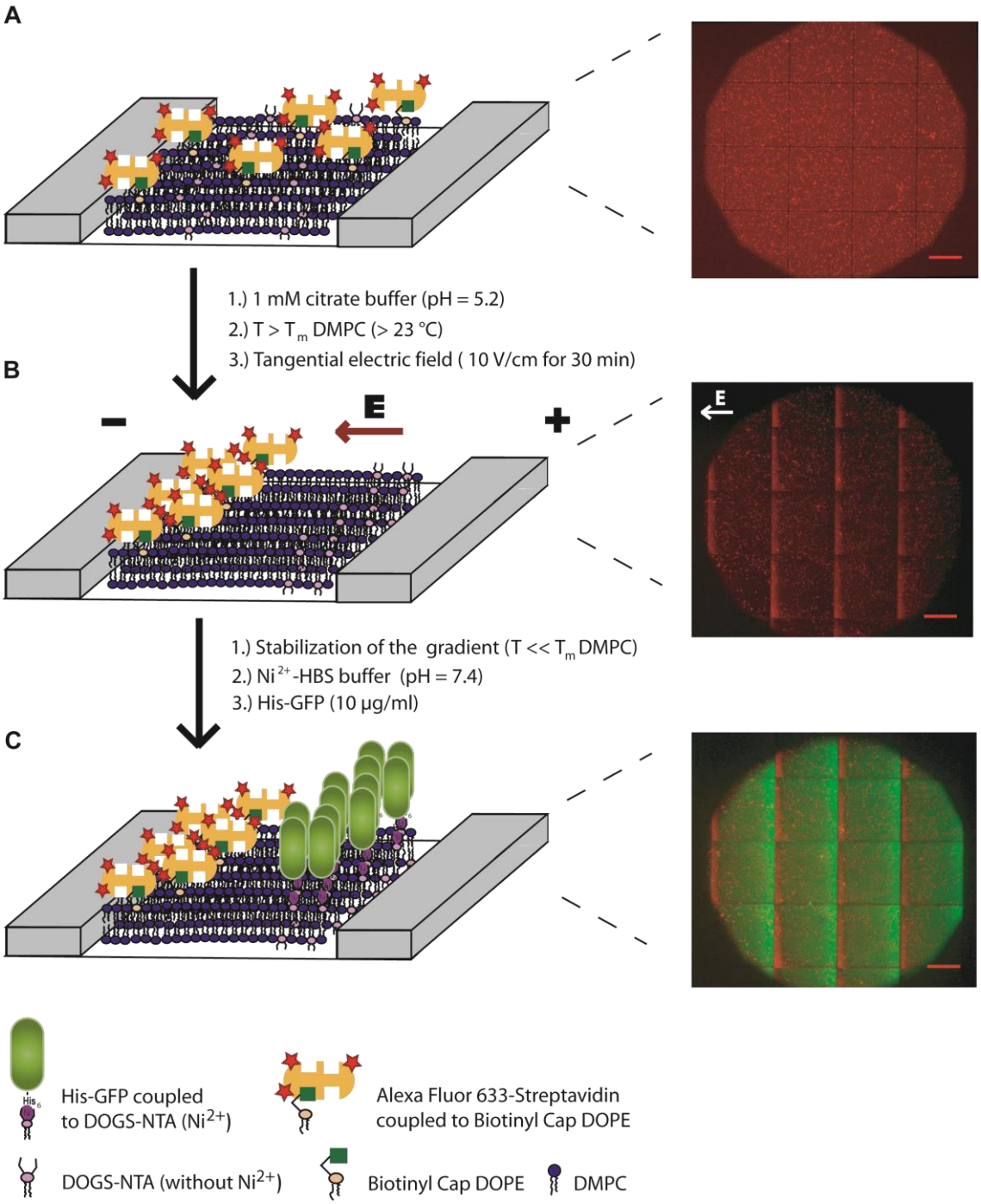

Fig. 3-16: Schematic illustration of the procedure to create two oppositely oriented protein gradients on patterned supported membranes. (A) Patterned supported membrane consisting of 98.5 mol% DMPC, 0.5 mol% Biotinyl Cap DOPE, and 1 mol% DOGS-NTA functionalized with Alexa Fluor 633 streptavidin (B) Patterned supported membrane after applying an electric field of 10 V/cm for 30 min. (C) Two oppositely oriented protein gradients on patterned supported membranes. The insets on the right side are fluorescence microscope images of the sample and each can be correlated to the scheme on its left. The scale bars in the fluorescence microscope images correspond to 250 µm. The area illustrated in the scheme corresponds to one square (500 x 500 µm) and is bordered by Cr/Ni-metal barriers (gray bars) exhibiting a width of 10 µm and a height of 13 ± 2 µm. The schematic illustrations on the left side are not in scale.

4. Characterization of Lipid Monolayers and Supported Membranes Functionalized with a Histidine-Tagged Cell Adhesion Protein

4.1. Introduction

Developmental processes in multicellular organisms are controlled by a multitude of different signaling molecules such as growth factors or hormones. In order to facilitate quantitative investigations, it is necessary to focus on a small amount of participants in these complex processes. Here, one major task is to create a simple biocompatible model system exhibiting one important factor such as the adhesion molecule *Xenopus* cadherin 11 (Xcad-11), which is a fundamental key player in controlling the balance between cell-cell and cell-matrix interactions during the neural crest cell (NCC) development of the African clawed frog *Xenopus laevis*.

To create a suitable model system, planar lipid membranes, so-called "supported membranes", have been used, utilizing their fluid character and their consequent applicability as two-dimensional matrices to accommodate membrane-associated proteins.

In order to functionalize the supported membranes, lipids with biotin head groups[61,62] or lipids with nitrilotriacetic acid (NTA) head groups[16,17] can be incorporated and used to couple various recombinant proteins and carbohydrates with biotin and histidine tags, respectively. In the case of histidine-tagged proteins, divalent metal ions, e.g. Ni^{2+}, Zn^{2+}, or Cu^{2+}, first have to be linked to the chelator nitrilotriacetic acid (NTA) to enable successful coupling.

In this chapter, supported membranes have been functionalized by coupling extracellular domains (EC1-3) of Xcad-11 with oligohistidine tags to ‘anchor’ lipids with nitrilotriacetic acid (NTA) head groups.[16,17] In order to use this approach a precise physicochemical confirmation of the coupling is required.

Thus, in the first part of this chapter, the focus was put on the quantitative confirmation of the Ni^{2+}-NTA complex formation. In the second part the quantitative coupling of the histidine-tagged Xcad-11 to the DOGS-NTA anchor lipids was demonstrated.

4.2. Quantitative characterization of the Ni^{2+}-NTA complex

Prior to the functionalization of supported membranes with incorporated lipids exhibiting NTA head groups with histidine-tagged Xcad-11 the successful complexation of NTA with the divalent Ni^{2+} ion must be confirmed. As the first step, specular X-ray reflectivity (XRR) was used to obtain detailed information about the fine vertical structure of lipid monolayers containing different molar fractions of NTA lipids in the presence of Ni^{2+} ions. In the second step, the results obtained from XRR, combined with those obtained by grazing incidence X-ray fluorescence (GIXF), were utilized to precisely determine the density of Ni^{2+} ions complexed with chelator groups and the consequent Ni^{2+}-NTA binding stoichiometry.
Both techniques are performed simultaneously at the air/water interface as described in Chapter 3.2.2. Fig. 4-1 presents a schematic illustration of the experimental setup.

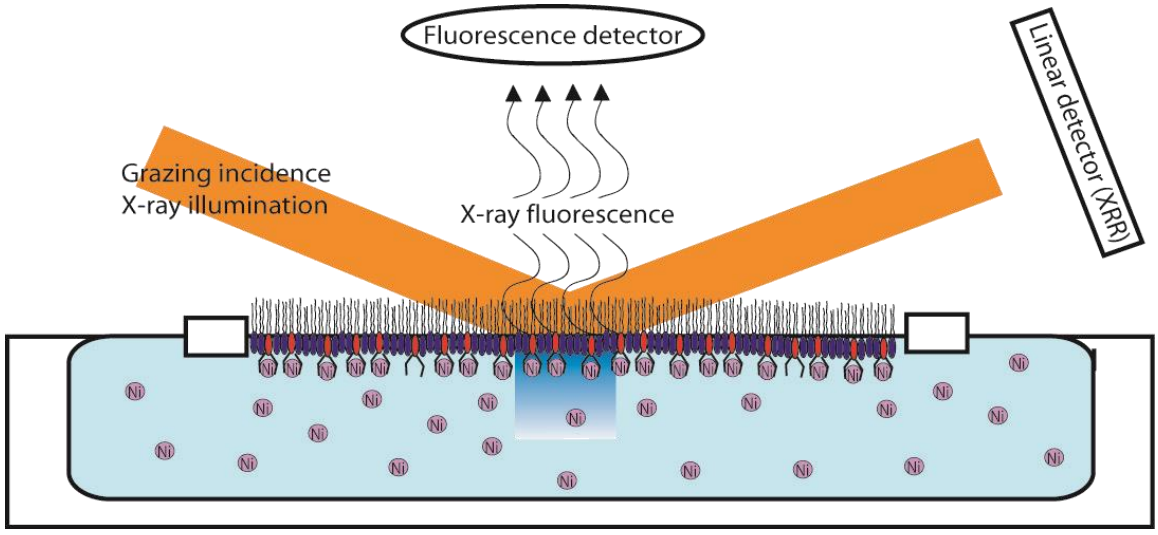

Fig 4-1: Schematic illustration of the experimental setup and the scattering geometry of XRR and GIXF used in this work to determine the Ni^{2+}-NTA complex stoichiometry.

4.2.1. Fine-structure of lipid monolayer with different NTA lipid concentrations

SOPC monolayers incorporating 5 mol%, 25 mol%, and 50 mol% DOGS-NTA on Ni^{2+}-loaded buffer were investigated by XRR. The corresponding curves are shown in Fig. 4.2.

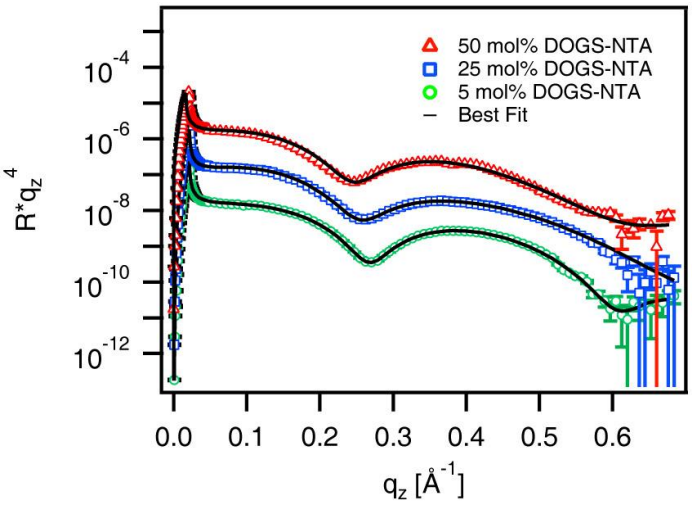

Fig 4-2: XRR results of SOPC monolayers incorporating 5 mol% (open green circles), 25 mol% (open blue squares) and 50 mol% (open red triangles) DOGS-NTA on Ni^{2+}-loaded buffer. The best fits corresponding to the experimental results are presented as solid lines.[63]

To gain information about the thickness, roughness and electron density profile of the lipid monolayer, the measured XRR curves were fitted using the Parrat formalism (Chapter 3.1.1) and by modeling the SOPC/DOGS-NTA monolayer with a two-slab model as shown in Fig. 4-3. Here, the first slab represents the alkyl chains (layer 1) and the second one the head groups (layer 2) of the lipids. Ni^{2+}-loaded buffer (layer 3) and air (layer 0) were both assumed to have a infinite thickness.

This fitting requires an estimation of reasonable values for the model parameters. Here the following results published by Malkova et al.[64] for a SOPC monolayer were used as a starting point for the electron density ρ and thickness d of the alkyl chains (layer 1) and the head groups (layer 2): ρ_1 = 0.423 e × Å^{-3}, d_1 = 10.5 Å, ρ_2 = 0.210 e × Å^{-3} and d_2 = 10.6 Å. The initial value for the root mean square (rms) roughness σ of each interface was estimated to be in the range of 3-6 Å.

The best fit results are presented as solid lines in Fig. 4.2. In addition, the electron density (ρ) profiles in the direction perpendicular to the membrane plane were reconstructed and are presented in Fig. 4-3.

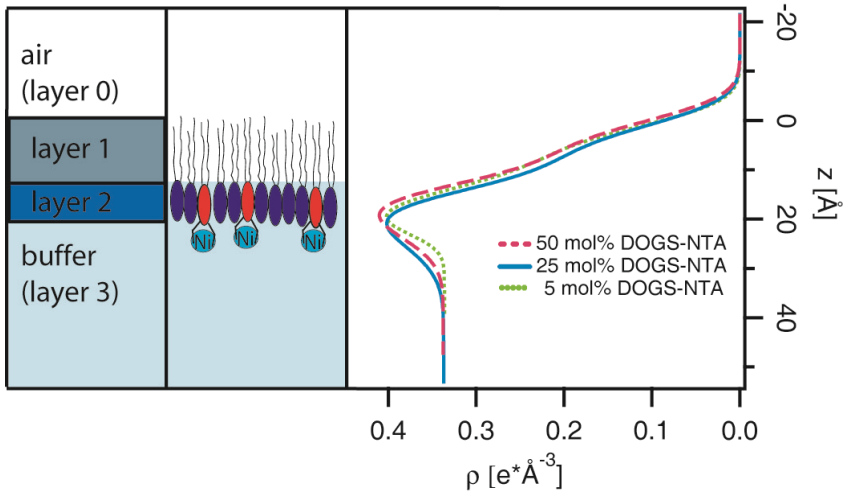

Fig. 4-3: Two-slab model (on the left) and the reconstructed electron density profiles in the direction perpendicular to the air/water interface.[63]

The resulting thickness d, electron density ρ, and root mean square (rms) roughness σ of each interface are summarized in table 4-A.

Table 4-A: Parameter of SOPC/DOGS-NTA monolayers on Ni^{2+}-loaded buffer corresponding to the best fits in Fig. 4-2.

5 mol% DOGS-NTA	d [Å]	ρ [e × Å^{-3}]	σ [Å]
Alkyl chain	12.8	0.222	4.0
Head group	8.6	0.435	4.1
Buffer	-	0.336	2.9

25 mol% DOGS-NTA	d [Å]	ρ [e × Å^{-3}]	σ [Å]
Alkyl chain	12.8	0.206	4.1
Head group	8.7	0.451	3.8
Buffer	-	0.336	5.8

50 mol% DOGS-NTA	d [Å]	ρ [e × Å^{-3}]	σ [Å]
Alkyl chain	13.1	0.213	4.2
Head group	9.7	0.451	3.9
Buffer	-	0.336	5.0

As shown in table 4-A, the thickness (d ~ 12.8 Å), electron density (ρ ~ 0.2 e × Å^{-3}) and roughness (σ ~ 4 Å) of the alkyl chains of mixed monolayers exhibit no significant dependence on the molar fraction of DOGS-NTA. The increase in the molar fraction of DOGS-NTA led to a small increase in the thickness and electron density in the head group region. These changes of the head group parameters can be understood by considering the increase in the lateral density of bulky chelator (nitrilotriacetic acid) head groups with a higher electron density. Furthermore, the two lipid components (SOPC and DOGS-NTA) in the monolayer can be assumed to be ideally mixed as demonstrated by pressure-area isotherms (appendix A.4).

4.2.2. Stoichiometry of the Ni^{2+}-NTA complex

SOPC monolayers incorporating 5 mol%, 25 mol%, and 50 mol% DOGS-NTA were investigated at the air/water interface by XRR and GIXF simultaneously. Fig. 4-4 shows the resulting Ni^{2+}-Kα fluorescence intensities as a function of the incident angle α_i on Ni^{2+}-loaded buffer.

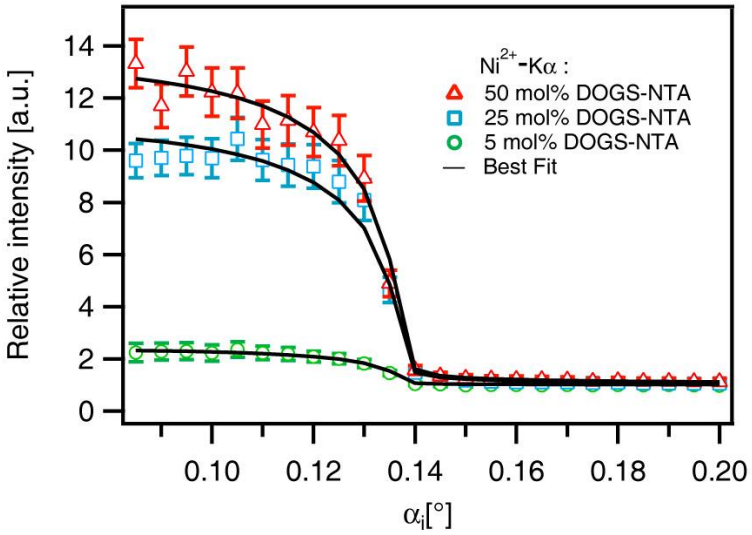

Fig. 4-4: Relative Ni^{2+}-Kα intensities from SOPC monolayers incorporating 5 mol% (green open circles), 25 mol% (blue open squares) and 50 mol% (red open triangles) DOGS-NTA on Ni^{2+}-loaded buffer, measured at α_i below and beyond the critical angle of total reflection. Error bars correspond to standard deviations from Gaussian error propagation during the fitting. The solid lines indicate the best fit results to the experimental data.

In order to exclude the influence of the physical properties of fluorescence lines and other geometrical effects, the fluorescence signals from lipid monolayers were always normalized to the corresponding signals from the blank buffer and modeled accordingly.

As described in the theoretical part (Chapter 3.2.1), GIXF takes advantage of the small penetration depth of the evanescent X-ray waves at small incident angles. In fact, the penetration depth below the critical angle is a few nanometers and above it is in the micrometer range.

Consequently, the fluorescence intensity below the critical angle is dominated by the fluorescence of elements that were located close to the surface, while above it is dominated by

the fluorescence of elements in the bulk. The buffer-normalized fluorescence signal of Ni^{2+}-Kα collected below the critical angle (α_c) is stronger than that measured at angles higher than α_c for all molar fractions of NTA lipids. This observation clearly indicates the enrichment of Ni^{2+} ions near the air/water interface. Moreover, an increase in the molar fraction of DOGS-NTA results in higher fluorescence intensities. In addition, the illumination profile spreads out as the incident angle increases and approaches to the critical angle (see Fig. 3-7 in Chapter 3.2.1). As a consequence, the contribution of the fluorescence signal from the ions close to the surface decreases and is gradually decaying to the bulk level.

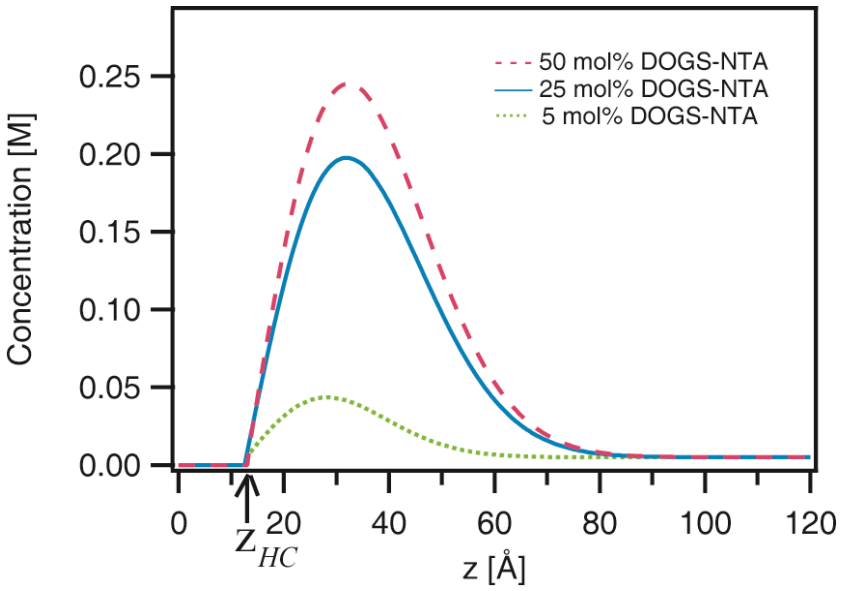

Fig. 4-5: The Ni^{2+} ion concentration profiles normal to the air/water interface, reconstructed from the best fit results. Z_{HC} indicates the onset of the ion concentration profile.

Using the asymmetric Gaussian function introduced in the theoretical part (equation 3-48), the concentration profiles of the Ni^{2+} ions were modeled. Fig. 4-5 shows the concentration profiles corresponding to the best fit results presented as solid lines in Fig. 4-4 is shown. As Ni^{2+} ion bulk concentration c_0 = 5 mM was used. The arrow in Fig. 4-5 indicates the onset of ion concentration profile (z_{HC} in equation 3-48) which corresponds to the thickness of alkyl chains (see table 4-A), since z = 0 is defined as the alkyl chain/air interface in the XRR analysis. The parameters for c_0 and z_{HC} are kept constant during fitting of the experimental data. This enables modeling ion distributions with only two free parameters: (i) the concentration maximum c_{max} and (ii) the z-position z_{max} of this maximum.

For blank buffer, a constant concentration profile was assumed, due to the negligibly small fluorescence signal from ion depletion near the interface.[65]

The obtained concentration profiles pointed out that the combination of XRR and GIXF allows for the localization of target elements in vertical direction within Å accuracy. As visible in Fig. 4-5, the peak position of the Ni^{2+} concentration profile was found at Z_{max} = 29 ± 5 Å for the monolayer with 5 mol% DOGS-NTA. A slight shift to a higher distance at higher molar fractions (z_{max} = 32 ± 5 Å) agrees well with the larger head group thickness obtained by XRR.

Moreover, the lateral density (c_L) of Ni^{2+} ions can be estimated by integrating the excess concentration along the z-axis. For example, a lateral Ni^{2+}-density of $c_L = 7.9 \times 10^4$ ions/µm² can be calculated for a lipid monolayer exhibiting 5 mol% DOGS-NTA. The average area occupied by one NTA-lipid can be assumed to be 1160 $Å^2$ if the average area per lipid molecule of A = 58 $Å^2$ (determined by pressure-area isotherms, appendix A.4) was used. Consequently, by making use of the calculations described in appendix A.5, the number of Ni^{2+} ions associated with one DOGS-NTA molecule can be estimated to be $N_{Ni} = 0.91 \pm 0.25$. This result demonstrates that every NTA group forms a chelating complex within experimental error. The maximum concentration of Ni^{2+}-ions (c_{max}), the stoichiometry of Ni^{2+}-NTA complex (N_{Ni}) and the peak position (z_{max}) are summarized in Table 4-B. The binding stoichiometry of lipid monolayer containing 50 mol% DOGS-NTA ($N_{Ni} = 0.63 \pm 0.05$) was much lower than for monolayers containing 5 mol% or 25 mol%, respectively, suggesting, in certain cases, the formation of a complex consisting of one Ni^{2+} ion and two neighboring DOGS-NTA lipids.

Table 4-B: The lateral density (c_L) of Ni^{2+} ions, the peak position (z_{max}), the maximum concentration of Ni^{2+}-ions (c_{max}) and the stoichiometry of Ni^{2+}-NTA complex (N_{Ni}).

	c_L [x 10^{12} ions/cm²]	z_{max} [Å]	c_{max} [mM]	N_{Ni}
5 mol% DOGS-NTA	7.9	29 ± 5	36.7 ± 3.7	0.91 ± 0.25
25 mol% DOGS-NTA	38.8	32 ± 5	192.6 ± 26.2	0.94 ± 0.17
50 mol% DOGS-NTA	47.9	32 ± 5	240.3 ± 11.0	0.63 ± 0.05

The 1:1 stoichiometry found at 5 and 25 mol%, are in very good agreement with previous studies using atomic absorption spectroscopy[66] and isothermal titration calorimetry.[67] It should be noted that the former study deals with NTA groups covalently coupled to a glass surface and the latter with NTA groups in bulk solution. In contrast, the combination of XRR and GIXF at the air/water interface offers the possibility of quantitatively determining and controlling both the lateral density and binding stoichiometry of the NTA groups.

4.3. Functionalization of the lipid monolayer and supported membrane

As described in the previous chapter, the Ni^{2+}-NTA complex binding stoichiometry in the case of SOPC monolayer doped with 5 mol% DOGS-NTA was demonstrated to be approximately 1:1. This result confirmed a successful loading of the NTA-chelator with Ni^{2+} ions, allowing the investigation of the coupling of histidine-tagged Xcad-11 to NTA-lipids, incorporated in either lipid monolayers or supported membranes.

In the first part of this chapter, the combination of XRR and GIXF at the air/water interface was used to confirm the functionalization of the lipid monolayer with the histidine-tagged adhesion protein *Xenopus* cadherin-11 (Xcad-11). Here, both techniques are performed simultaneously as described in Chapter 3.2.2. A schematic illustration of the experimental setup at the air/water interface is shown in Fig. 4-6.

Because native membranes largely consist of a lipid bilayer that imparts them a fluid character, complex cell membranes can be mimicked by planar lipid bilayer models on solid substrates (also called supported membranes). Therefore, the final application of the chelator lipid DOGS-NTA is to functionalize supported membranes with Xcad-11 in order to create complex experimental cell-surface models. In the last part of this chapter functionalized supported membranes at the solid/liquid interface were characterized by (1) high energy XRR measurements of supported membranes containing 5 mol% NTA lipids before and after coupling of Xcad-11 and (2) QCM-D measurements. A schematic illustration of the functionalized supported membrane is shown in Fig. 4-7.

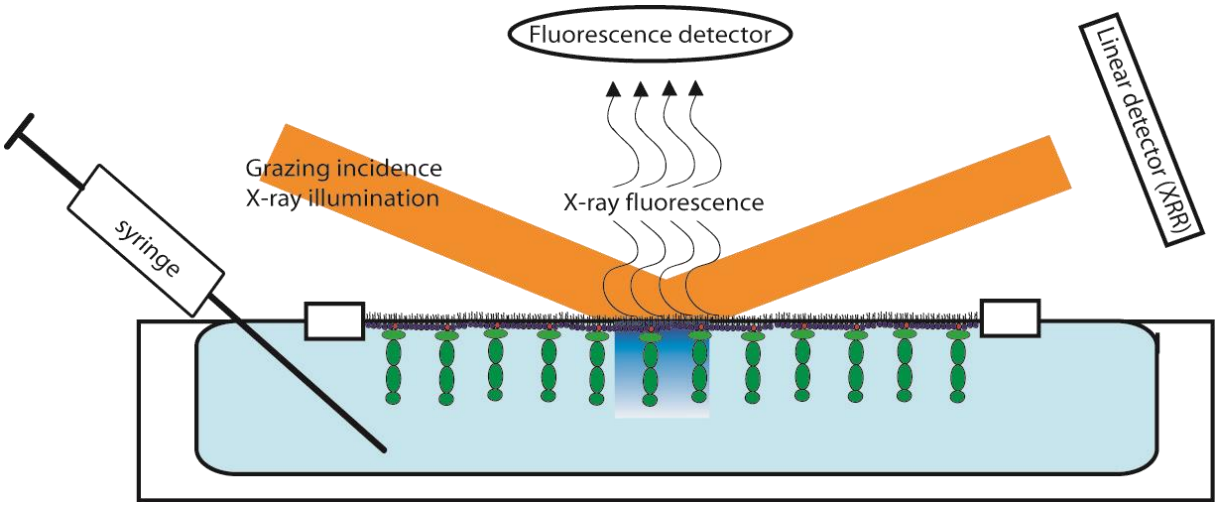

Fig. 4-6: The experimental setup and the scattering geometry used for simultaneous XRR and GIXF at the air/water interface.[63]

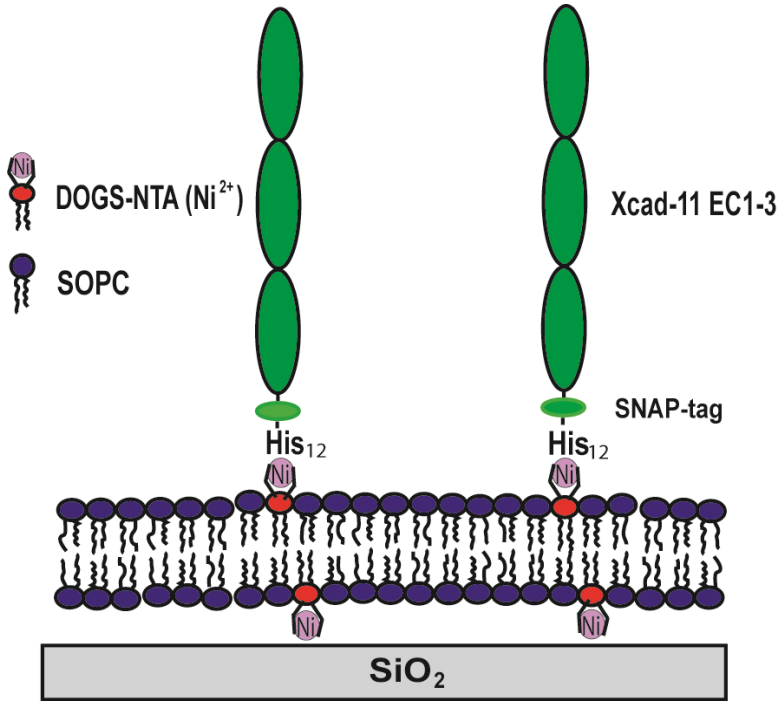

Fig 4-7: Supported membrane at the solid/liquid interface, functionalized with Xcad-11, used for high energy XRR and QCM-D measurements. As lipid anchors, DOGS-NTA was homogenously mixed into matrix lipids (SOPC).[68]

4.3.1. Functionalization of the lipid monolayer with *Xenopus* cadherin-11

4.3.1.1. Specular X-ray reflectivity measurements

As shown in Fig. 4-8, the fine-structure of a lipid monolayer containing 5 mol% NTA lipids at the air/water interface was investigated before (open black circles) and after (open red squares) the binding of histidine-tagged recombinant proteins (Xcad-11).

As described in chapter 2.4.1, the coupling of Xcad-11 to the lipid monolayer was achieved by injecting the protein solution (final concentration: 10 µg/ml) underneath the monolayer. To ensure the thermodynamic equilibrium of the Xcad-11 binding, the monolayer was incubated with the protein for 6 hours prior to the XRR measurement. A non-specific physisorption of Xcad-11 could be ruled out by obtaining a constant surface pressure of the monolayer after the injection and incubation of the protein solutions.

Comparing both XRR curves demonstrated that the position of the minima, which indicate the presence of layers with high electron density contrast, shift towards lower q-values in the presence of Xcad-11 (Fig. 4-8, blue dotted line to green dotted line). This shift indicated an increase in total thickness due to the protein coupling.

The XRR curve of the monolayer with Xcad-11 was modeled with a three-slab model (see Fig. 4-9). The successful coupling can be confirmed by the fitting results shown in Table 4-C.

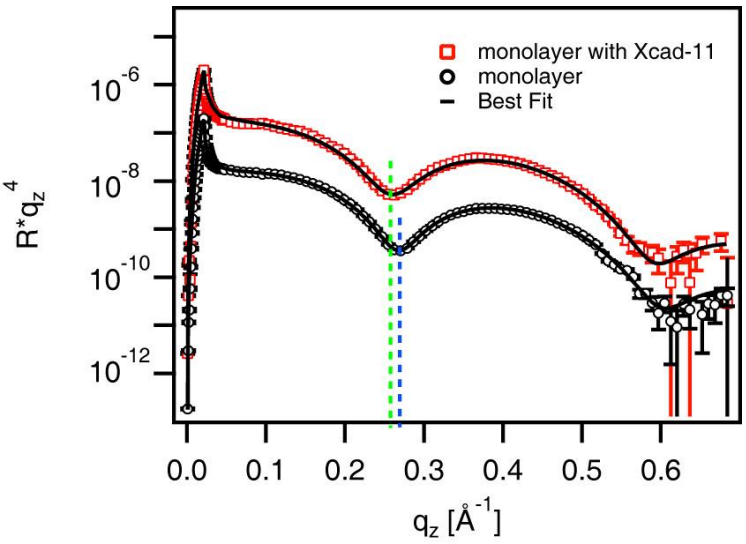

Fig. 4-8: Specular X-ray reflectivity curves of a monolayer doped with 5 mol% DOGS-NTA before (open black circles) and after (open red squares) the binding of Xcad-11, measured on Ni^{2+}-free buffer. The solid lines represent the best fit models matching the experimental results. The dotted line illustrates the first minimum position of the XRR curve of the monolayer (blue dotted line) and the monolayer with Xcad-11 (green dotted line). The shift of the minimum position indicates an increase in the total thickness due to the additional protein layer.[63]

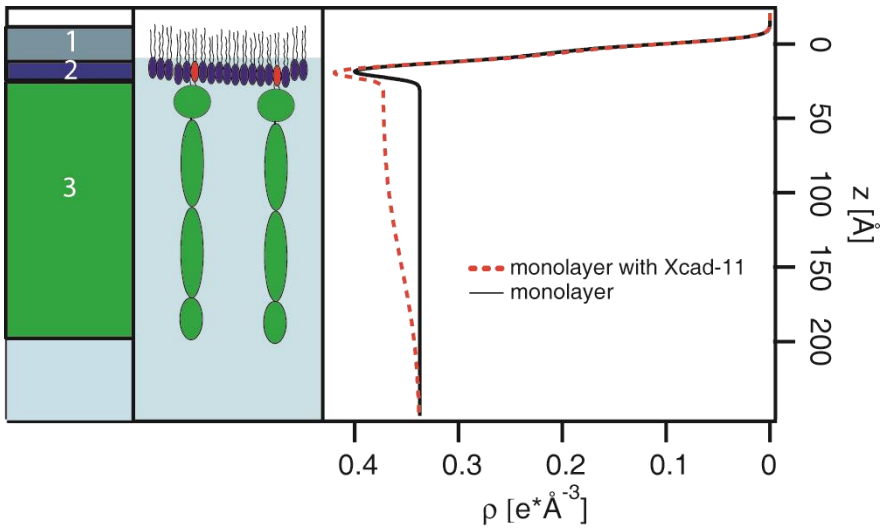

Fig. 4-9: Three-slab model (on the left) and the reconstructed electron density profiles in the direction perpendicular to the air/water interface.[63]

The parameter of the lipid monolayer in the presence and absence of Xcad-11 EC1-3 from the best fits in Fig. 4-8 are summarized in table 4-C. The comparison of the layer parameters of a monolayer (open circles) on Ni^{2+}-free buffer to those on Ni^{2+}-loaded buffer before Xcad-11

binding (Chapter 4.2.1, Table 4-A), resulted in almost identical values. Accordingly, the stoichiometry of chelator complexes can be estimated to be identical to that on Ni^{2+}-loaded buffer.

Table 4-C: Parameter of SOPC/DOGS-NTA in the absence and presence of Xcad-11 EC1-3 from the best fits in Fig. 4-8.

5 mol% DOGS-NTA (monolayer)	d [Å]	ρ [e x Å^{-3}]	σ [Å]
Alkylchain	13.0	0.206	3.8
Head group (SOPC,DOGS-NTA-Ni)	8.3	0.444	4.4
water	-	0.336	3.2

monolayer + Xcad-11 EC 1-3	d [Å]	ρ [e x Å^{-3}]	σ [Å]
Alkylchain	13.1	0.201	3.9
Head group (SOPC,DOGS-NTA-Ni)	8.8	0.454	4.3
X-Cad11 (EC 1-3)	126.5	0.373	3
water	-	0.336	50.0

As shown in table 4-C the binding of Xcad-11 to the monolayer did not cause any remarkable change in the thickness, electron density, and interface roughness for both alkyl chains and head groups. This suggested that Xcad-11 molecules are not integrated into the monolayer core but attached to the anchor lipids within the monolayer.

The calculated thickness of the recombinant Xcad-11 layer at the air/water interface was 127 Å, which is a plausible value, since the molecule used contains only 2 adhesion domains (EC 1-3) of the whole (EC 1-5) cadherin molecule, which has a full length of ~ 220 Å.[69] Furthermore, the electron density (ρ) of the protein layer, 0.373 e x Å^{-3}, is in good agreement with a previous study on C-cadherin.[70] The larger roughness of the Xcad-11/water interface (50.0 Å) as compared to the other interfaces can be attributed to the fact that the Xcad-11 "layer" is composed of a mixture of rod-like cadherin molecules and water filling the space between the proteins.

4.3.1.2. Grazing incidence X-ray fluorescence measurements

The monolayer system was investigated after addition of histidine-tagged Xcad-11 to the buffer to confirm a successful coupling. The resulting relative S Kα fluorescence intensity from a SOPC monolayer doped with 5 mol% DOGS-NTA 6 hours after the injection of Xcad-11 (open circles) is shown in Fig. 4-10. By using the electronic structures obtained from XRR (Chapter 4.3.1.1; Table 4-C) the illumination profile of a lipid monolayer functionalized with Xcad-11 was calculated. The resulting illumination profile was used to obtain the concentration profile of S-atoms.

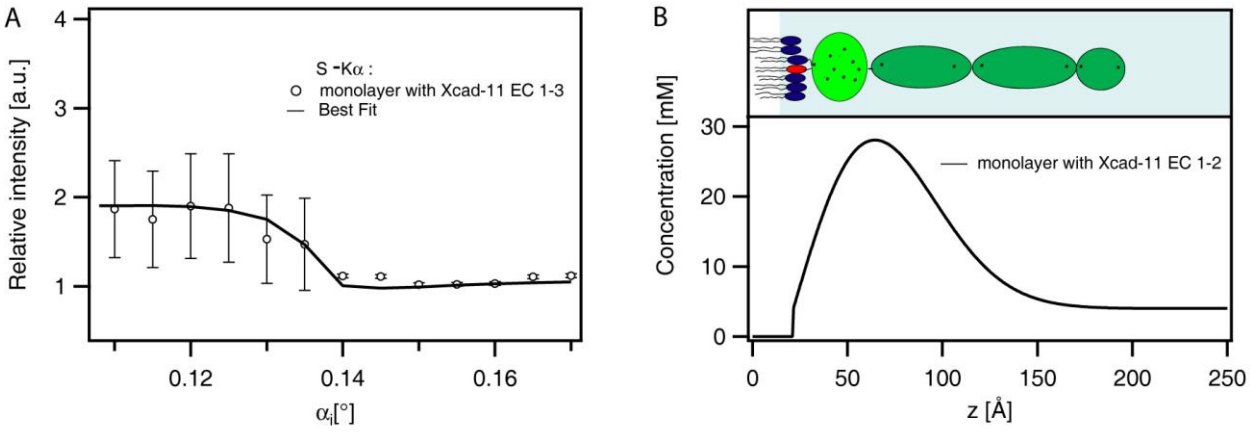

Fig. 4-10: (A) Relative S Kα intensities from SOPC monolayers incorporating 5 mol% DOGS-NTA after the binding of Xcad-11 (open circles) as a function of α_i on Ni^{2+}-free buffer. Vertical error bars are ± standard deviations obtained from Gaussian error propagation during the fitting of the fluorescence spectra. The solid lines indicate the best fit to the experimental data. (B) The Sulfur-atom concentration profile normal to the interface reconstructed from the best fit results. The scheme above illustrates the corresponding recombinant Xcad-11 coupled to the monolayer. The protein part (hAGT) close to histidine-tag is bright green, whereas the dark green parts correspond to the EC 1-3 domain. The dark dots illustrate the number of S-atoms in each part.[63]

Similar to the Ni^{2+} ions in Chapter 4.2.2, the S-atom concentration profile was modeled using the assymetric Gaussian function (equation 3-48). Here, the z_{HC} value is the total thickness of the alkyl chain and the head group obtained by XRR (d = 13.1 + 8.8 Å = 21.9 Å, Table 4-C). The resulting S-atom concentration profile reconstructed from the best fit result (Fig. 4-10A) is presented in Fig. 4-10B. As a result, the maximal concentration of S-atoms can be found at Z_{max}= 68 ± 16 Å. This estimated peak position suggests the specific binding of Xcad-11 via

the histidine-tag from the structure of recombinant Xcad-11,[70] since the protein part adjacent to the histidine-tag (hAGT)[71] contains more S-atoms (9) than the following EC 1-3 domain (6). The spatial location of the peak position was achieved with high accuracy, but it should nevertheless be noted that the obtained fluorescence intensity below the critical angle was only twice that obtained from the bulk level. This observation is in contrast to a previous study on neutravidin, where the intensity below the critical angle (at $\alpha_i < \alpha_c$) was higher by a factor of 4-6 than for bulk.[36] In consequence, the determination of the maximal concentration (c_{max}) value was difficult, since it strongly depends on the intensity level at $\alpha_i < \alpha_c$. By integrating the area below the curve in Fig. 4-10B a lateral concentration of S-atoms of $(2.7 \pm 0.3) \times 10^{-25}$ mol/nm^2 was obtained. Using the total number of S-atoms in recombinant Xcad-11 (15), the area occupied by one recombinant molecule can be estimated to be ~ 90 nm^2. This value is about 8 times smaller than the value expected from the lateral density of lipid anchors (~ 11.6 nm^2). According to this finding, the distinct difference in the sensitivity between Xcad-11 and neutravidin can be explained by the broader distribution near the interface of S-atoms within the recombinant Xcad-11 compared to those of neutravidin.

4.3.2. Functionalization of the supported membrane with *Xenopus* cadherin-11

4.3.2.1. High energy specular X-ray reflectivity measurements

The fine-structures of supported membranes displaying Xcad-11 were resolved by illuminating the samples at high energy (22 keV) and measuring the consequent specular X-ray reflectivity (XRR) at the solid-liquid interface. In Fig. 4-11 shows the XRR curves of the supported membrane doped with 5 mol% DOGS-NTA before (black circles) and after (red diamonds) the binding of Xcad-11. Similar to the results at the air/water interface (Chapter 4.3.1.1) both XRR-curves exhibit two pronounced minima. Moreover, in the presence of Xcad-11 a shift towards lower q values was measured, indicating an increase in total thickness due to the protein coupling.

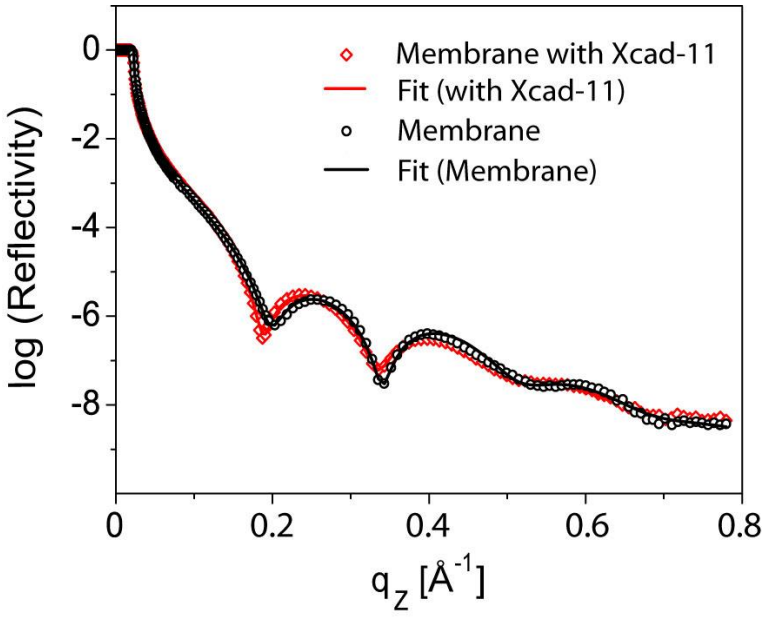

Figure 4-11: Fine-structure of supported membranes probed by X-ray reflectivity. (A) Specular X-ray reflectivity curves of the supported membrane with 5 mol% DOGS-NTA before (black) and after (red) the binding of Xcad-11. The experimental errors are within the symbol size. The solid lines represent the best model fits to the data.[68]

The reflectivity of the solid supported membrane (black) was fitted by using the Parrat formalism (described in Chapter 3.1.1) with 5 slabs (outer head groups, hydrocarbon tails, inner head groups, water reservoir and SiO_2). The layer parameters of the membrane functionalized with Xcad-11 were obtained by analyzing the reflectivity with a six-slab model, shown in Fig. 4-12, right side. The other layers are Ni^{2+}-loaded buffer (layer 6 or layer 7) and Si wafer (layer 0). Both slabs were assumed to be of infinite thickness.

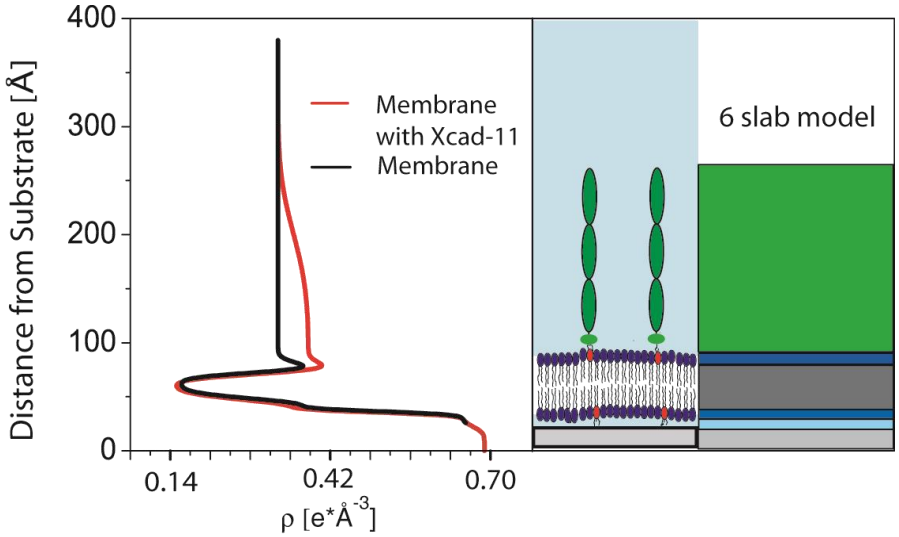

Fig. 4-12: The corresponding electron density ρ profiles demonstrate that the Xcad-11 anchored on the surface at a high density can be treated as a "layer". The six-slab model used for analysis is shown on the right.[68]

In Fig. 4-11 the best fit results are presented as solid lines, and the corresponding electron density ρ profiles are shown in Fig. 4-12. The thickness *d*, electron density ρ, and root mean square (rms) roughness σ of each interface are summarized in Table 4-D (supported membrane) and in Table 4-E (supported membrane displaying Xcad-11).

Table 4-D: The best fit parameters for the reflectivity results for the supported membrane as presented in Fig. 4-11.

	Thickness [Å]	ρ [e x Å^{-3}]	Roughness [Å]
Head group (SOPC, DOGS-NTA-Ni)	7.1	0.433	5.0
Alkyl chain	24.8	0.160	3.8
Head group (SOPC, DOGS-NTA-Ni)	6.9	0.454	5.1
water	4.0	0.333	3.3
SiO_2	15.0	0.660	2.4

Table 4-E: The best parameters for the reflectivity results for the supported membrane displaying Xcad-11 as presented in Fig. 4-11.

	Thickness [Å]	ρ [e x Å^{-3}]	Roughness [Å]
Xcad-11 EC 1-3	126.0	0.386	44.5
Head group (SOPC, DOGS-NTA-Ni)	7.8	0.461	5.4
Alkyl chain	25.5	0.149	4.4
Head group (SOPC, DOGS-NTA-Ni)	6.9	0.433	5.8
water	4.0	0.333	3.4
SiO_2	14.0	0.660	2.4

Comparing the values of thickness, electron density and roughness of hydrocarbon chains layers before and after the protein coupling, demonstrated that almost no change was detected. Furthermore, the obtained structural parameters for (a) the hydrocarbon chains, (b) the proximal and distal head group regions and (c) the water reservoir between the lipid bilayer and the substrate agree well with other published values for fluid membranes.[20,64,72-75]

The calculated thickness and electron density of Xcad-11 layer at the solid/liquid interface were 126 Å and 0.386 e x Å^{-3}, respectively. Both values agree well with the study of Xcad-11 coupled to lipid monolayers at the air/water interface (see Chapter 4.3.1) and thus confirm the reproducibilty of the membrane-protein coupling using different preparation methods. The higher roughness of the Xcad-11/liquid interface (44.5 Å) relative to the other interfaces can be attributed, as already mentioned in Chapter 4.3.1.1, to the fact that the Xcad-11 "layer" is composed of a mixture of rod-like cadherin molecules and water filling the space between them. Moreover the stability of the membrane functionalization with Xcad-11 was confirmed by observing identical reflectivity curves even 10 hours after rinsing with HBS buffer.

4.3.2.2. Quartz crystal microbalance with dissipation measurements

Using the quartz crystal microbalance with dissipation (QCM-D) technique, the binding of recombinant Xcad-11 to supported membranes was further investigated. As described in Chapter 3.3.1, QCM-D can be used to record changes in the resonance frequency and dissipation as functions of time. In Fig. 4-13, the coupling and decoupling of Xcad-11 to the supported membrane was monitored. As the first step, a supported membrane containing 5 mol% DOGS-NTA is formed by injecting the vesicle suspension (I) and a subsequent vesicle fusion on the QCM-D crystal. After reaching the steady state and rinsing with HBS, the resulting frequency change Δf of approximately - 26 Hz and the dissipation change ΔD of almost 0 confirmed the formation of a planar supported membrane, in accordance with previously reported values.[44] The addition of Xcad-11 solution (II) led to a continuous change in both Δf and ΔD. After 70 min of protein incubation, the non-specifically adsorbed Xcad-11 was washed off and a frequency decrease as well as an increase in dissipation was detected. The observed changes in frequency (Δf = - 17.3) and dissipation ($\Delta D = 1.81 \times 10^{-6}$) suggest an increase in the surface mass density by the deposition of a protein layer. By addition of 100 mM EDTA solution (III) and subsequent rinsing with HBS (IV), the Ni^{2+}-NTA complex was dissociated, resulting in the decoupling of histidine-tagged Xcad-11, which could be detected by the frequency increase and a final dissipation close to 0. This result demonstrated the specific binding of Xcad-11 with a histidine tag to the chelator head group (Ni^{2+}-NTA complex).

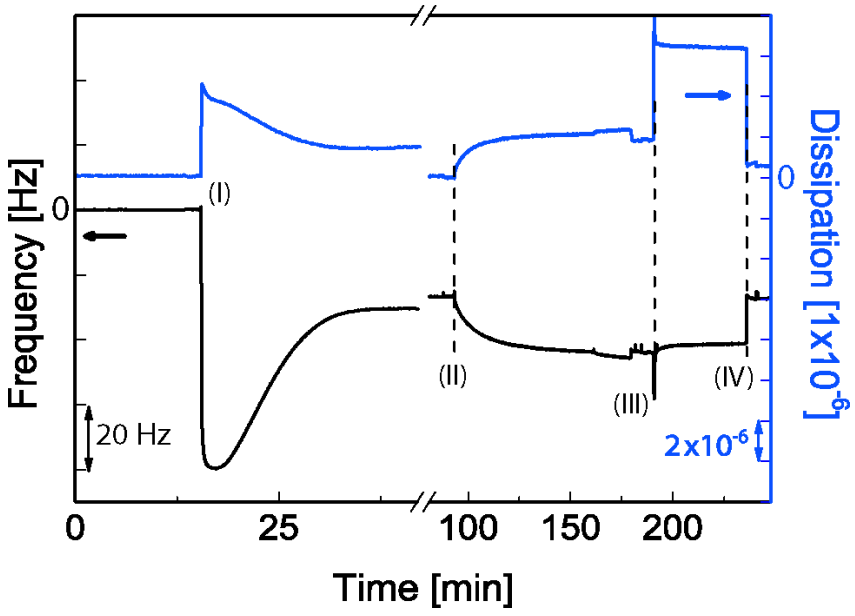

Fig 4-13: Formation and functionalization of supported membranes. Formation of a supported membrane containing 5 mol% DOGS-NTA (I), specific binding of Xcad-11 EC1-3 SNAP His12 (II) and decoupling of Xcad-11 (through incubation with EDTA-solution (III) and subsequent washing (IV)) monitored by QCM-D. The membrane deposition, protein binding and protein decoupling are detected by changes in the resonance frequency Δf and dissipation ΔD.[68]

Since the changes in dissipation ΔD are observed to be on the order of 1×10^{-6} for a frequency change Δf of - 10 Hz, the adsorbed protein layer can be defined as rigid.[25,42,43] Consequently, the Sauerbrey equation (Chapter 3.3.1, equation 2.52) can be utilized to convert the changes in the resonance frequency to the mass densities of Xcad-11 coupled to the membrane. When interpreting the result, it is important to keep in mind that a direct conversion of the calculated mass change Δm Xcad-11 [kg/m^{-2}] to the protein density [mol/m^{-2}] is not possible due to the mass of hydrating water, which is included in the measured mass. Nevertheless, the calculated mass change (Δm Xcad-11) increased linearly with the molar fraction of DOGS-NTA as presented in Table 4-F.

Table 4-F: Calculated changes in mass density caused by the coupling of Xcad-11 (Δm) and the average distance between anchor lipids ($<d>$) at different molar fractions of DOGS-NTA anchors (x_{NTA}).[68]

NTA lipids in SOPC (χ_{NTA})	%	1	2	5
Δm Xcad-11 EC 1-3	ng/cm²	45.5	73.2	304.7
$<d>$	Å	80.6	57.0	36.1

As shown by pressure-area isotherms of the SOPC/DOGS-NTA monolayer, the mixing behavior was confirmed to be ideal (appendix A.4). As a result, the average distance $<d>$ between the DOGS-NTA anchor lipids can be determined from the average area per lipid (here A_{lipid} = 65 Å^2 was used)[76] and the molar fraction of DOGS-NTA χ_{NTA}:

$$< d >= \sqrt{\frac{A_{lipid}}{\chi_{NTA}}} \tag{4.1}$$

Furthermore, the long-term stability of the protein binding via NTA-histidine linkers was checked. The measured change in frequency Δf after the protein coupling was less than 5 % over 5 hours, which confirmed the stability and agrees well with the results of previous experiments with e-GFP and DSRed tetramers with histidine tags.[60] As another control experiment, a supported membrane existing solely of SOPC lipids was studied in the presence of histidine-tagged Xcad-11. No change in frequency or dissipation was observed, confirming that no unspecific protein adsorption occurred.

4.4. Conclusion

In this chapter, the quantitative functionalization of lipid monolayers and supported membranes by coupling histidine-tagged, extracellular domains (EC1-3) of Xcad-11 to DOGS-NTA 'anchor' lipids was confirmed.

First, the Ni^{2+}-NTA chelator complex formation was quantitatively determined by using the combination of specular X-ray reflectivity (XRR) and grazing incidence X-ray fluorescence (GIXF). From XRR measurements, detailed information about the fine-structures of lipid monolayers containing different molar fractions of NTA lipids was obtained. These results were used for the GIXF data analysis to precisely determine the concentration profile of Ni^{2+} ions normal to the air/water interface. In this way, a remarkable accumulation of Ni^{2+} ions near the air/water interface was detected with high sensitivity. Furthermore, the yield of Ni^{2+}-NTA complex formation was demonstrated to be more than 90 % for molar DOGS-NTA lipid ratio of 5 and 25 mol%.

Second, the functionalization of lipid monolayer and supported membranes with Xcad-11 was confirmed by using (1) the combination of XRR and GIXF at the air/water interface, (2) high energy XRR at the solid/water interface, and (3) QCM-D.

To investigate the coupling of Xcad-11 to lipid monolayers doped with DOGS-NTA lipids at the air/water interface, the combination of XRR and GIXF was used. XRR provided information about changes in the fine-structures before and after protein coupling. GIXF monitored the S Kα fluorescence emission of the S-atoms within the recombinant Xcad-11. Consequently, the combination of both techniques yields the lateral density of the coupled protein.

Regarding the functionalization of solid-supported lipid bilayer systems, measurements performed with high energy XRR and QCM-D confirmed the successful coupling of Xcad-11.

High energy XRR provided the structural parameters of supported membranes in the presence and absence of Xcad-11, which could be treated as a uniform layer with a thickness of 126 Å and electron density of 0.386 $e \times Å^{-3}$. Quartz crystal microbalance with dissipation (QCM-D) experiments further confirmed a linear dependance of the protein-dependent mass density changes on the molar fraction of the anchor lipid.

5. Stress-Free Immobilization of Pluripotent Tissue Sheets on Supported Membranes Displaying *Xenopus* Cadherin-11 for Targeted Cell Differentiation

5.1. Introduction

In the previous chapter, supported membranes functionalized with the adhesion molecule *Xenopus* cadherin-11 (Xcad-11) were quantitatively characterized. In this chapter, the applicability of the functionalized supported membranesto study developmental processes will be investigated. In order to study NCC development, a cohesive pluripotent tissue sheet explanted from *Xenopus laevis* embryos (a so-called "animal cap") was placed on the substrate. The animal caps were already induced by the pre-injection of mRNA encoding truncated bone morphogenetic protein receptor (tBR) and *Xenopus* Frizzled 7 (XFz7) into one blastomere of a two-cell stage *Xenopus laevis* embryo. tBR, a truncated isoform of the native BMP receptor, acts as inhibitor of the BMP signaling pathway. XFz7, as frizzled protein, activates the canonical Wnt/ß-catenin pathway. [77-79] Consequently, the pre-injection of mRNA encoding for tBR and XFz7 in well-defined concentrations yields a level of Wnt and BMP factors necessary to divert animal cap cells from their epidermal fate to become neural crest cells.[80]

The interaction between *Xenopus* animal caps that had already been induced to the NCC fate with functionalized supported membranes was systematically studied as a function of various lateral densities of Xcad-11. Initially, the adhesion area and height fluctuation of tissue sheets in contact with substrates was investigated by using the label-free reflection interference contrast microscopy (RICM). Furthermore, the explants additionally labeled with membrane markers were simultaneously observed using fluorescence microscopy to obtain information about the cell-cell (in-plane) interactions within the adherend tissue sheet. Finally, the capability of supported membranes displaying Xcad-11 to support the NCC differentiation of animal caps was investigated. One of the most reliable markers for premigratory NCCs in amphibian embryos is the transcription factor *slug* that controls the transformation of non-motile epithelial cells into migrating cells.[2,81] Therefore, a *slug* promoter reporter construct fused to green fluorescent protein (GFP) can be used as a read-out system for successful NCC development.[82,83]

5.2. Adhesion of animal cap cells

5.2.1. Definition of contact area and adhesive patches

According to the theoretical description of RICM (Chapter 3.4.2), destructive interference of linearly polarized light reflected from a substrate surface and a cell surface at low cell-surface distances leads to dark patches, indicating close cell-substrate contacts.[45,52,84]

In animal cap adhesion studies, the contact area was defined to be enclosed by the first interference fringe of minimal intensity (region of interest in Fig. 5-1B, marked in blue) originating from the curved cell membrane.

Within the contact area I_{max} is the maximal and I_{min} the minimal intensity of the interference signal I (defined by equation 3.60 in Chapter 3.4.2). I_{max} and I_{min} were used to define adhesion patches as regions darker than $I_{\min} + \frac{I_{\max} - I_{\min}}{2}$ (Fig. 5-1B, red area inside region of interest).

The red area outside the region of interest is caused either by the inhomogeneous background or higher order minima and is therefore excluded from definition of the adhesion area. The inhomogeneous background can be explained by the fact that only some adhering cells in the tissue are in close contact with the substrate and thus measurable by RICM, although the animal cap retained a connective structure in the background.

Fig. 5-1 represents the RICM image of an animal cap that remained in contact with a supported membrane displaying Xcad-11 molecules for 4 hours at an average distance of $\langle d \rangle \sim 5.7$ nm (corresponds to 2 mol% DOGS-NTA according to equation 4.1).

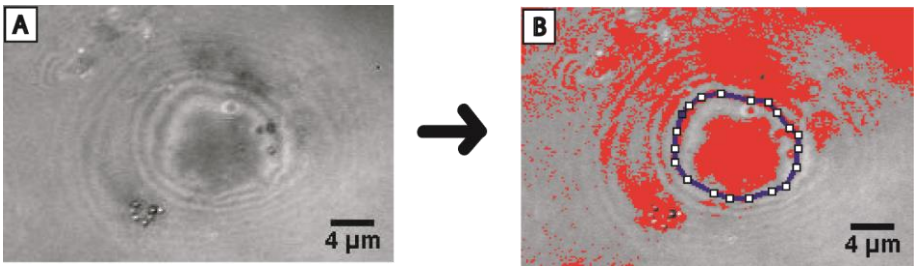

Fig. 5-1: Definition of contact area and adhesive patches. (A) Animal cap on a supported membrane containing 2 mol% DOGS-NTA cultivated for 4 hours. Interference "fringes" surrounding the patch are originated from the higher order of interference and indicate the contact area. (B) Contact area of an animal cap is marked in blue and the adhesion area is labeled in red. The red area outside the region of interest is caused by the inhomogeneous background or higher order intensity minima and is therefore excluded from the adhesion area definition.

5.2.2. Cell adhesion and height fluctuations

Measurements of the pixel intensity *I* along a line across the contact area (defined in previous sub-chapter) of an adhesive cell exhibit spatial intensity fluctuations (see Fig. 5-2).

In principle this fluctuation of pixel intensity can be used to obtain the probability function of the cell-surface distance *P(h)*. The probability function sensitively reflects the effective interaction potential *V(h)* and thereby the superposition of forces governing cell-surface interaction. The potential $V(h)$ is described within the framework of a Boltzmann distribution function: $V(h) \sim -kT \ln P(h)$.[84,85]

In this thesis, quantitative values for *P(h)* or *V(h)* could not be calculated as the information about the cell-to-substrate distance *h(x,y)* was missing (see explanations in Chapter 3.4.2). Nevertheless, in spite of the lack of quantitative information about the cell-surface distance, some estimates from the apparent intensity fluctuations were derived. Therefore, it was assumed that a linear relation between intensity and height variation exists.

A cell with little attraction to the functionalized surface exhibits strong intensity, i.e. height fluctuations within the contact area, since the adhesion is weak. If the cell´s attraction to the substrate increases, the cell starts to adhere to the surface by forming adhesion patches that can be observed by suppression of height fluctuation.

Fig. 5-2A-B shows an RICM image of an animal cap placed on a supported membrane displaying Xcad-11 molecules at an average distance of $\langle d \rangle \sim 8.1$ nm (which corresponds to 1 mol% DOGS-NTA) after 4 hours of cultivation. Here, the height fluctuations across the contact zone were relatively prominent (Fig. 5-2B), indicating a rather weak adhesion. This finding seemed to be consistent with previous reports on synthetic lipid vesicles.[84]

In contrast, on RICM images of animal caps on membranes displaying Xcad-11 at $\langle d \rangle \sim 5.7$ nm (Fig. 5-2C-D), an observed flattening of the cell membrane between the first order maxima ($x = 0.7$ µm and 9.2 µm, indicated with red arrows in Fig. 5-2D) was observed. Such suppression of the height fluctuation was interpreted as an area of close adhesion.[84,85]

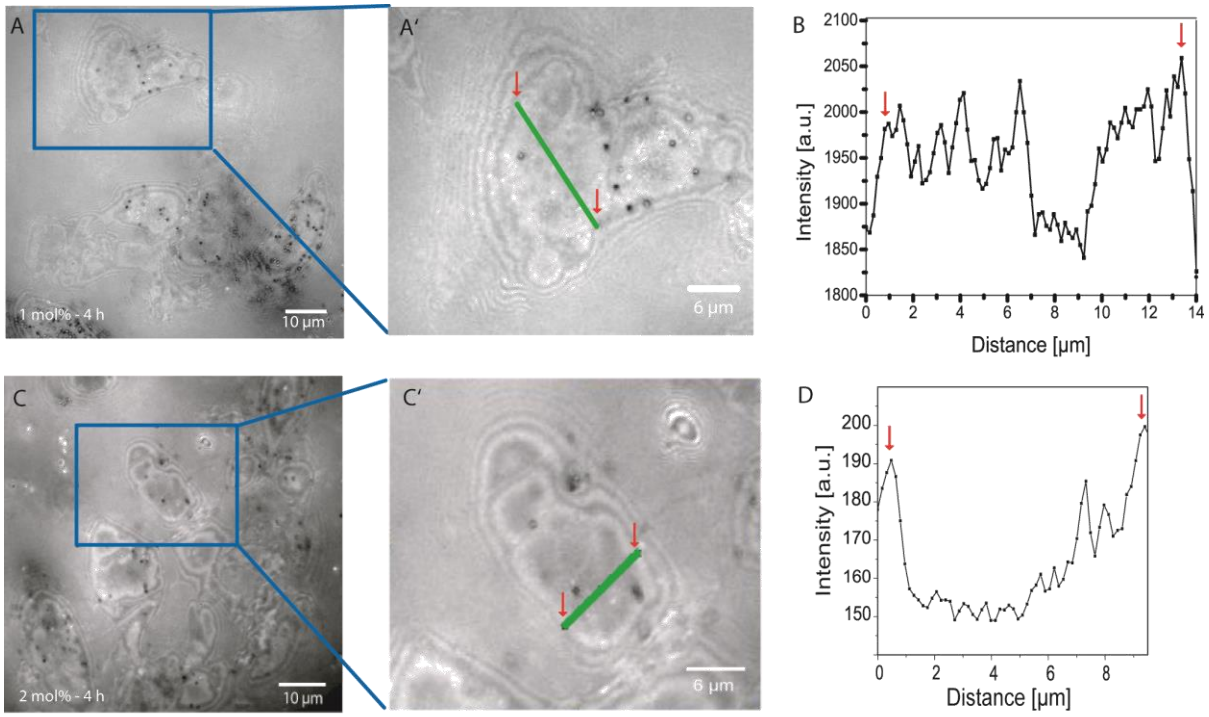

Fig. 5-2: Adhesion study of animal cap tissues on supported membranes displaying Xcad-11, performed by measuring height fluctuations. With the aid of microinterferometry (RICM), the regions of close cell-surface contact was identified as the darker patches. (A, A', C, C') Animal caps on membranes containing 1 mol% DOGS-NTA (panel (A), $\langle d \rangle \sim 8.1$ nm) or 2 mol% DOGS-NTA (panel (C), $\langle d \rangle \sim 5.7$ nm) after 4 h incubation. Panels (A') and (C') show the enlargement of the blue rectangle in panel (A) and (C), respectively. The intensity profiles along a the green line in the panels (A') and (C') are shown in panel (B) and (D), respectively. The first order maxima are indicated by with red arrows and adhesion-dependent height fluctuations. Additionally, the accumulation of apparent adhesion patches towards the cell center were detected. The small black spots in A, A', C and C' are pigment granules inside ectoderm cells and had to be excluded from the analysis.

5.2.3. Quantitative determination of adhesion area and number of adhesive patches per view area

First, the ratio of adhesion area (using the definition described in Chapter 5.2.1) relative to the area of the whole microscope image was quantitatively determined with respect to the cultivation time and the lateral density of Xcad-11 on the substrate.

At the earlier stage of the animal cap cultivation (t = 0 hours) on supported membranes displaying Xcad-11 molecules at an average distance $\langle d \rangle \sim 5.7$ nm, (4.9 ± 1.8) % of the entire microscope image was detected as strong adhesion area. These dark patches were mainly observed close to the cell periphery, which seems plausible, as Xcad-11 was reported to accumulate in cell protrusions during the initial stages of adhesion.[86]

When the animal caps were incubated for longer durations (t = 4 h), the area of strong contact inside a single adhering cell increased, implying that Xcad-11 pairs became coalescent towards the middle of the cells.[84,87,88] Accordingly, the ratio of strong adhesion areas relative to the area of the whole microscope increased to (5.8 ± 2.5) % at t = 4 hours (n = 15 explants).

Secondly, the number of cells with adhesion patches larger than 30 µm² was counted per view area.

As presented in Fig. 5-3, the increase of the lateral density of DOGS-NTA, corresponding to a decrease in the average distance between Xcad-11 molecules, yielded an increase in the number of cells with adhesion patches larger than 30 µm² per view area of 2×10^4 µm².

This observation demonstrated the trans-interaction of Xcad-11 on the supported membrane with the endogenous Xcad-11 on the cell surface.[89,90] Moreover, the compatibility of supported membranes displaying Xcad-11 to sustain the stable immobilization of tissue sheets was verified by the increase in the number of adherent cells from 1 hour to 4 hours.

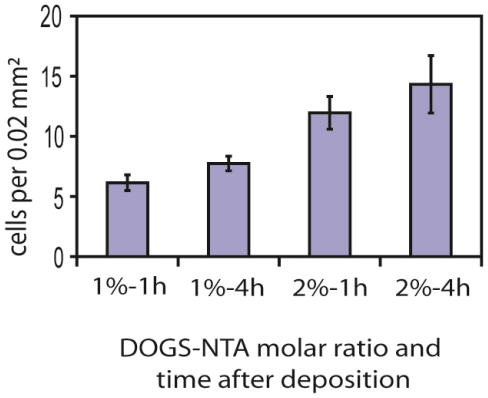

Fig. 5-3: Number of cells with adhesion patches larger than 30 µm² per view area. The cell number density in tissue sheets with adhesion patches larger than 30 µm² within an area of 2×10^4 µm² showed a clear increase with increasing molar ratio of DOGS-NTA and time. This result suggests that the adhesion of animal caps on supported membranes displaying Xcad-11 is specifically mediated by Xcad-11 and develops as a function of time. At least 3 explants per condition were used to make the histograms. Error bars indicate the standard deviation.[68]

5.3. Connectivity of cells in animal caps

As presented in Fig. 5-4 and observed via RICM measurements, only a few portions of the cells in the animal cap tissues adhered to the surface while also retaining a connective tissue structure. In order to verify the connectivity of cells in each animal cap, the same animal cap tissue sheets were imaged using RICM and fluorescence microscopy.

First, induced (as described in Chapter 3.4.3) animal caps cultivated for 4 hours on pure phospholipid membranes (100 mol% SOPC), as well as untreated wildtype animal caps on membranes exposing Xcad-11 at a lateral distance of $\langle d \rangle \sim 5.7$ nm, were investigated as examples for animal caps losing their connectivity (i.e. controls).

Secondly, for the case of an induced animal cap on a pure phospholipid membrane, no dark patches as signs for close adhesion were observed by RICM (Fig. 5-4A) and the corresponding fluorescence image (Fig. 5-4B) showed no extension of any cell protrusion. Further incubation for 4 hours led to the disintegration of cohesive cells within the tissue and thus subsequent cell death. The observations with RICM after 4 hours of cultivation of untreated wildtype animal caps on supported membranes displaying Xcad-11 at a lateral distance of $\langle d \rangle \sim 5.7$ nm suggested the adhesion of some cells in tissue (Fig. 5-4D). In contrast, the fluorescence image of the same tissue sample (Fig. 5-4E) showed that the cells were not able to form filopodia and lamellipodia. Furthermore, the formation of numerous membrane buds (Fig. 5-4E, F) was observed suggesting the loss of structural integrity of cell membranes and thus cell death (Fig. 5-4E).

In contrast, in induced animal caps placed on membranes functionalized with Xcad-11 ($\langle d \rangle \sim 5.7$ nm), the cells showed connectivity for at least 4 hours of incubation. Here the RICM image exhibited dark adhesion patches as a consequence of the strong damping of the height fluctuation and, hence, as a clear sign of adhesion (Fig. 5-4G). Whereas, in the corresponding fluorescence image (Fig. 5-4H) the formation of filopodia and lamellipodia (highlighted with white arrows) was observed, which can be interpreted as the first sign of neural crest cell formation.[91]

It is important to point out that the suppression of the fluctuation of cell-substrate distance and the formation of filopodia and lamellipodia were observed only for induced tissues on membranes functionalized with Xcad-11. Moreover, an increase in the number of filopodia per mm^2 in the induced tissue from an average of 3.9 at t = 0 hours up to 6.5 after 4 hours was

observed. This finding confirms that induced tissue sheets adhere to, remain viable on and properly shape the cells on supported membranes functionalized with Xcad-11.

In conclusion, supported membranes displaying Xcad-11 at <*d*> ~ 5.7 nm were demonstrated to serve as compatible and sustainable surfaces for the immobilization of animal caps without disrupting intercellular connections in tissue sheets.

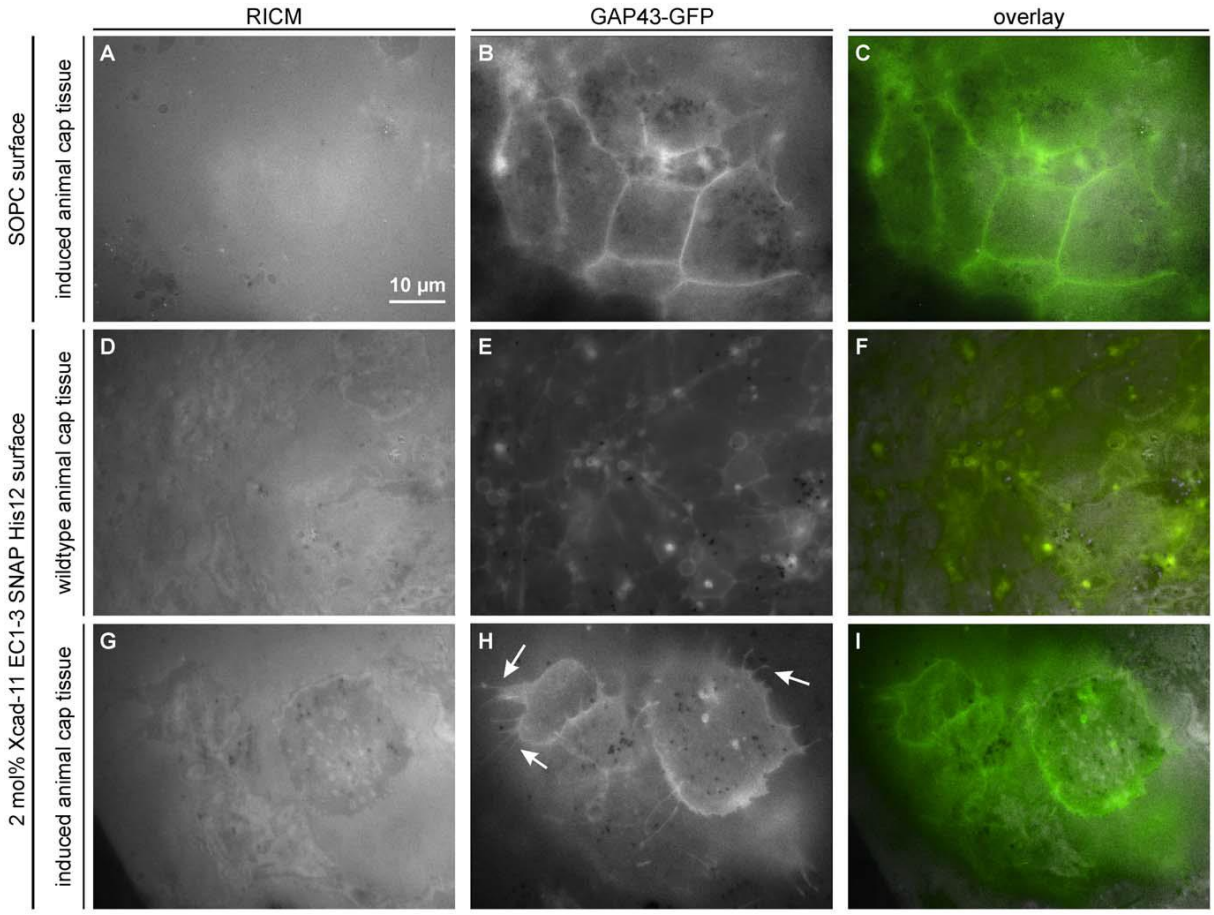

Fig. 5-4: Induced and wildtype animal cap tissues on supported membranes with and without Xcad-11 (t = 4 hours). The animal cap cells were labeled with GAP43-GFP for visualization of the membrane. (A–C) Induced tissue did not adhere on non-functionalized SOPC membranes, showing no adhesion patch (A) and no filopodia (B). Image B was taken at z ≈ 2 µm above A. (D–F) Wildtype tissue cultivated on a supported membrane functionalized with Xcad-11 EC1–3 at <d> = 5.7 nm. Although some cells in the tissue sheets adhered to the supported membrane, the height fluctuations near the cell center were still remarkable (D). The tissue exhibited membrane budding (E, F), which is characteristic for disintegrated tissues. Images D and E were taken at the same z-position. (G–I) NCC induced animal cap on a Xcad-11 functionalized membrane (<d> = 5.7 nm). As presented in panel (G), the height fluctuation corresponding to the cell-surface distance was strongly damped compared to wildtype tissues on the same surface (D). The formation of filopodia and lamellipodia was characteristic for neural crest cells (H and I, indicated by arrows) which demonstrated that induced tissues remain viable and can properly shape the cells on membranes functionalized with Xcad-11. Images G and H are taken at the same z-position. Scale bar applies to all images.[68]

5.4. Specificity of tissue-membrane interaction

In order to verify that interactions between the induced tissue sheets and functionalized membranes are specifically mediated by homophilic Xcad-11 binding, animal cap tissues were cultured on membranes displaying different adhesion molecules.

First, the behavior of induced and wildtype animal caps cultured on membranes displaying E-cadherin EC 1-5 SNAP His12 (Ecad) at a lateral distance of $\langle d \rangle \sim 5.7$ nm was investigated. NC-induced animal caps expressing Xcad-11 were unable to adhere (Fig. 5-5A-C), [14] whereas wildtype tissue sheets displayed strong adhesion and formed cell protrusions (Fig. 5-5D-F). This result was expected since wildtype animal caps differentiate into atypical epidermis and express E-cadherin.[92]

Secondly, it was observed that induced animal caps did not survive on supported membranes that displayed RGD peptides, which are specific to integrin receptors, at an average distance of $\langle d \rangle \sim 5.7$ nm. Here, the cells lost their connective structural integrity and died after 2 h even though strong adhesion of individual cells to the surface could be detected.

The importance of Xcad-11-expression is shown by Fig. 5-5H-I. Here the tissue sheets were not able to adhere to the Xcad-11 functionalized membranes when Xcad-11 synthesis was blocked by the injection of antisense Xcad-11 morpholinos (Xcad-11 MO).

These findings suggest that the use of inadequate adhesion motifs to functionalize supported membranes disturbs cell-cell (in-plane) interactions within the tissue, most likely by altering mechanical forces or intercellular communication within the animal cap. Similar effects of cohesiveness were discussed in a previous report studying cell polarization at tissue boundaries. By combining cohesive tissues rather than single cells of different origin the successful cell polarization was observed.[13]

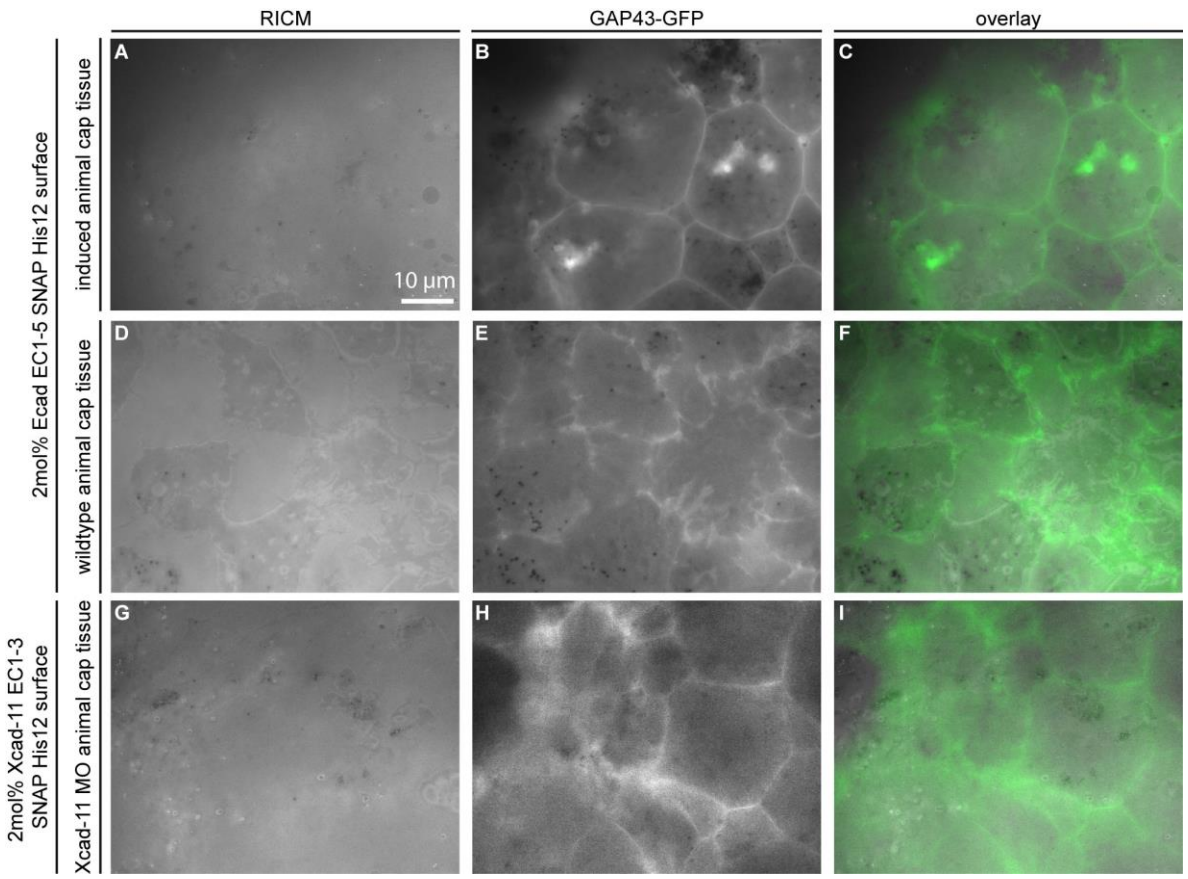

Fig. 5-5: Specificity of tissue-membrane interaction. (A-F) Cultivation of animal caps on Ecad EC1-5 SNAP His12 (Ecad) functionalized membranes. While neural crest induced animal caps (A-C) display expression of Xcad-11 and therefore show no adhesion to Ecad (resulting in no formation of adhesion patches or cell protrusions), wildtype animal caps (D-F) with expression of Ecad show clear adhesion patches and the formation of filopodia. This indicates the specificity of the observed membrane-tissue interaction. (G-I) Cultivation of antisense Xcad-11 morpholinos (Xcad-11 MO) animal caps on Xcad-11 EC1-3 SNAP His12 (Xcad-11) functionalized supported membranes. Animal caps with reduced expression of Xcad-11 due to treatment with Morpholino oligonucleotides that repress the translation of specific mRNA are unable to adhere to Xcad-11 functionalized membranes. Scale bar applies to all images.[68]

An overview on the behavior of induced and wildtype animal caps on differently modified surfaces (Xcad and Ecad functionalized lipid membranes (d ~ <5.7 nm>, non-functionalized lipid membrane and RGD functionalized lipid membrane (d ~ <5.7 nm>)) is given in table 5-A. Here, the numbers refer to the fraction of animal caps adhering to the surface after 0 and 4 hours, out of the total number of explants examined in each case.

Table 5-A. An overview on the behavior of induced and wildtype animal caps on differently modified surfaces

	Induced tissue		Wildtype tissue	
Incubation time	0 h	4 h	0 h	4 h
Behavior on **Xcad-11** substrates	Adhesion, cohesive tissue, filopodia		No adhesion, tissue dissociation, cell death	
Nr. of tissue sheets adhering to the surface / Nr. of explants examined (on **Xcad-11**)	13/18	13/18	11/20	5/20
Behavior on **Ecad** substrates	No adhesion, tissue dissociation, cell death		Adhesion, cohesive tissue, filopodia	
Nr. of tissue sheets adhering to the surface / Nr. of explants examined (on **Ecad**)	3/15	3/15	15/18	4/18
Behavior on **SOPC** substrates	No adhesion, tissue dissociation, cell death		No adhesion, tissue dissociation, cell death	
Nr. of tissue sheets adhering to the surface / Nr. of explants examined (on **SOPC**)	2/10	2/10	2/10	0/10
Behavior on **RGD** substrates	Strong initial adhesion, loss of cohesiveness after 2 h		Adhesion	
Nr. of tissue sheets adhering to the surface / Nr. of explants examined (on **RGD**)	6/9	3/9	2/5	3/5

5.5. Applicability of lipid membranes displaying adhesive molecules for controlled differentiation of cohesive pluripotent tissue sheets

The cell differentiation of cohesive pluripotent tissue sheets to neural crest cells (NCC) in induced animal caps can be monitored by the activation of the NCC marker gene *slug*, which is one of the earliest specifiers of NCC fate.[93,94] To confirm the induction of NCC, a reporter fusion construct consisting of the minimal *slug* promoter and GFP was co-injected at the two-cell stage of the *Xenopus* embryo. In Fig. 5-6, animal caps explanted at developmental stage 9 and incubated for 4 hours on supported membranes with and without Xcad-11 functionalization are shown.

As presented in Fig. 5-6B, induced explants on supported membranes displaying Xcad-11 consisted of a cohesive tissue exhibiting close cell-cell contacts and the activation of the *slug* reporter could be detected by GFP signals. Since *slug* is expressed only at early stages of NCC differentiation, the obtained result confirmed the successful induction of NCC in explanted *Xenopus* animal cap cells on supported membranes functionalized with Xcad-11.

As control experiments, NCC induced animal cap explants were incubated on pure SOPC (not functionalized) membranes (Fig. 5-6A) and non-induced (wildtype) animal caps on Xcad-11 functionalized membranes (Fig. 5-6C).

It was observed that NCC-induced tissue started to dissociate and cells lost cell-cell contact (Fig. 5-6A, gaps are highlighted by asterisks) on pure SOPC membranes. Non-induced, wildtype animal cap tissues were disintegrated and started to die (Fig. 5-6C) on Xcad-11 functionalized membranes.

The observation of stable cultivation of induced animal caps was only possible on supported membranes displaying Xcad-11 (Fig. 5-6B) can be attributed to the fact that a change in the cadherin profile accompanies the induction of NCC formation. While non-induced (wildtype) animal caps contain the maternally provided classical (C-) and XB-cadherin[95-97], neural crest cells (NCC) express Xcad-11 and neuronal (N-) cadherin instead.[98,99] Furthermore, it is important to consider that not only the cell-cell adhesion is mediated by Xcad-11, but also the formation of cell protrusions.[100] This finding suggests that to immobilize animal caps on supported membrane functionalized with Xcad-11, a successful induction of NCC is required.

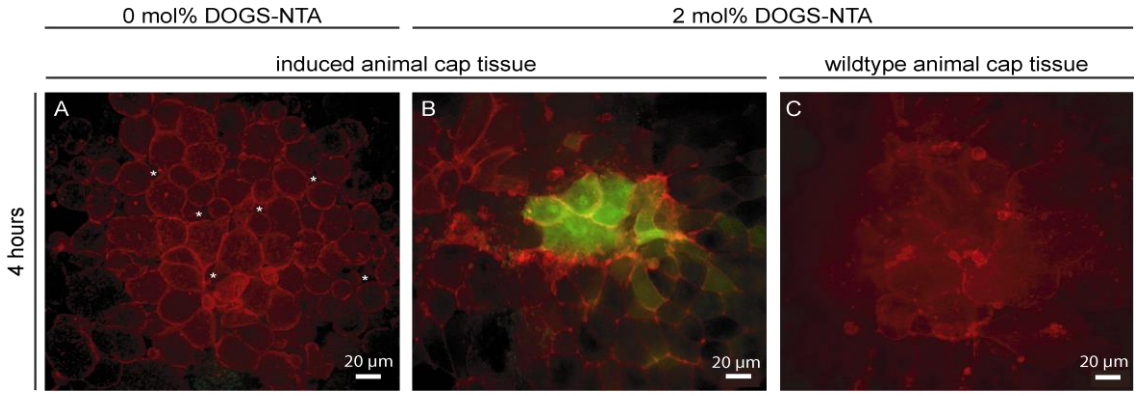

Fig. 5-6: Neural crest-induced and wild-type animal caps incubated on lipid membranes with and without Xcad-11. Animal cap explants were taken at stage 9, placed on the surface and imaged after 4 hours of cultivation. Activation of *slug*-promoter-GFP reporter (green) indicates successful neural crest induction. (A) NCC induced tissue started to dissociate and cells lost cell-cell contact (gaps are highlighted by asterisks) on pure SOPC membranes. (B) Induced explants on Xcad-11 functionalized surface (2 mol% DOGS-NTA) consisted of a cohesive tissue that showed close cell-cell contacts. A clear expression of the *slug* transcription factor was detected by the positive GFP signal. (C) Wildtype animal cap tissue disintegrated and started dying on functionalized membranes (2 mol% DOGS-NTA).[68]

5.6. Conclusion

In this chapter, the stress-free immobilization of pluripotent animal cap tissue sheets isolated from embryos of *Xenopus laevis* on supported membranes, quantitatively functionalized with recombinant Xenopus cadherin-11 (Xcad-11), was demonstrated.

First, planar animal caps were cultivated on the functionalized supported membranes and it was demonstrated that the adhesion behavior of animal cap tissue sheets, preinduced to neural crest cells (NCC), are strongly dependent on the lateral density of Xcad-11. Furthermore, the formation of filopodia and lamellipodia in the cohesive tissue verified the viability of the animal caps over several hours.

Secondly, the specific regulation of NCC induction was confirmed by cultivating different animal cap tissues (wildtype tissues and tissues treated with Cad-11 morpholino oligonucleotide) (1) on membranes functionalized with Xcad-11, (2) on pure phospholipid membranes, or (3) on membranes functionalized with recombinant E-cadherin.

Finally, the expression of the transcription factor *slug* in externally induced tissue demonstrated the applicability of lipid membranes displaying adhesive molecules for controlled differentiation of cohesive pluripotent tissue sheets.

6. Fine-Adjustable Opposite Concentration Gradients of Two Proteins on Supported Membranes

6.1. Introduction

It is well known that complex tissue structures evolve from uniform cell ensembles due to the appearance of spatial patterns of morphogen (e.g. BMP or Wnt) concentration gradients.[101,102] Therefore, developmental processes should be regulated in model systems with adjustable protein gradients. In the previous chapters, the simplified model system consisted of a solid supported membrane solely or functionalized with homogenously distributed adhesion molecule Xcad-11. The challenge now is to create a supported membrane functionalized with two different proteins, exhibiting opposite concentration gradients.

Supported membranes exhibit a high lateral fluidity (e.g. lateral diffusion of SOPC ~ 2-3 $\mu m^2/s$) [103,104] which allows the manipulation of linked molecules (e.g. proteins) by external forces such as electric fields. Therefore, the so-called membrane electrophoresis was used to accumulate charged molecules, which was demonstrated in supported bilayers by Stelze et al. [58] and combined with patterns of lateral diffusion barriers by Groves et al..[105] More recently, some studies reported the electrophoretic motion of proteins and how it can be adjusted.[60,106,107] However, up to now, there is no publication dealing with two oppositely oriented protein gradients on patterned supported membranes. For this purpose, a model system consisting of DMPC lipids and a different molar ratio of Biotinyl Cap DOPE and DOGS-NTA lipids was used. Biotinyl Cap DOPE has a strong affinity to Streptavidin proteins whereas DOGS-NTA serves as anchor lipid for histidine-tagged proteins.

In the first part of this chapter the mobility as well as the passive lateral diffusion of Alexa Fluor 633 streptavidin, linked to Biotinyl Cap DOPE, and DOGS-NTA were investigated by fluorescence recovery after photobleaching (FRAP). In the second part, an electric field was applied to generate two opposite concentration gradients of two proteins on micro-patterned supported membranes. First, a supported membrane, consisting of Alexa Fluor 633 streptavidin and DOGS-NTA, was electrically manipulated. Due to their different mobility in the electric field, the resulting gradients are oriented in opposite directions. Second, the subsequent coupling of His-GFP to DOGS-NTA yields two oppositely oriented protein gradients. In the last part, the steepness of the one-dimensional protein gradient can be sensitively controlled by using different lipid compositions.

6.2. Docking of recombinant proteins and passive lateral diffusion

In Fig. 6-1 a fluorescence image of Alexa Fluor 633 streptavidin linked to a patterned supported membrane is shown. Here, the supported lipid membrane consists of 98.5 mol% DMPC, 1 mol% DOGS-NTA, and 0.5 mol% Biotinyl Cap DOPE and was prepared by vesicle fusion on a patterned glass substrate (Chapter 2.2.2). The average area per Biotinyl Cap DOPE anchor, serving as anchoring point for the streptavidin, can be estimated from the average area per lipid in fluid phase A_{lipid} = 65 Å^2 and molar fraction of Biotinyl Cap DOPE to be ~ 130 nm².[76] Although this estimated average area per molecule should be small enough to avoid nonspecific protein adsorption onto the surface or lateral crystallization of proteins, a clustering of Alexa Fluor 633 streptavidin was observed (light red dotes in Fig 6-1). This clustering could not be prevented even by using very low concentrations of protein solution (5 µg/ml) or lower incubation times.

Nevertheless, fluorescence recovery after photobleaching (FRAP) measurements could be carried out to investigate the mobility as well as the passive lateral diffusion of the protein attached to Biotinyl Cap DOPE. A resulting FRAP curve is shown in Fig. 6-2A. The FRAP experiments demonstrated that (83 ± 7) % of Alexa Fluor 633 streptavidin were mobile on the membrane and exhibiting a passive lateral diffusion coefficient of 1.3 ± 0.4 µm²s^{-1}. The immobile fraction of streptavidin could be related to the protein clustering. However, it also demonstrated that the passive protein mobility is high enough to proceed with membrane electrophoresis experiments.

Furthermore, the passive lateral diffusion coefficient of DOGS-NTA was investigated in order to calculate the mean drift velocity of DOGS-NTA during membrane electrophoresis (as described in Chapter 3.5.1). DOGS-NTA was not labelled with a fluorescent marker thus FRAP of NBD-DHPE (assumed to have a comparable cross-section and therefore the same diffusion behavior) in a supported membrane, consisting of 98.5 mol% DMPC, 1 mol% NBD-DHPE, and 0.5 mol% Biotinyl Cap DOPE, was measured instead. A resulting FRAP curve is shown in Fig. 6-2B. Here, a passive lateral diffusion coefficient of 3.0 ± 0.4 µm²s^{-1} and a mobility of 96 ± 4 % were obtained.

The resulting diffusion coefficient and mobile fraction of the attached Alexa Fluor 633 streptavidin as well as those of NBD-DHPE are presented in Table 6-A.

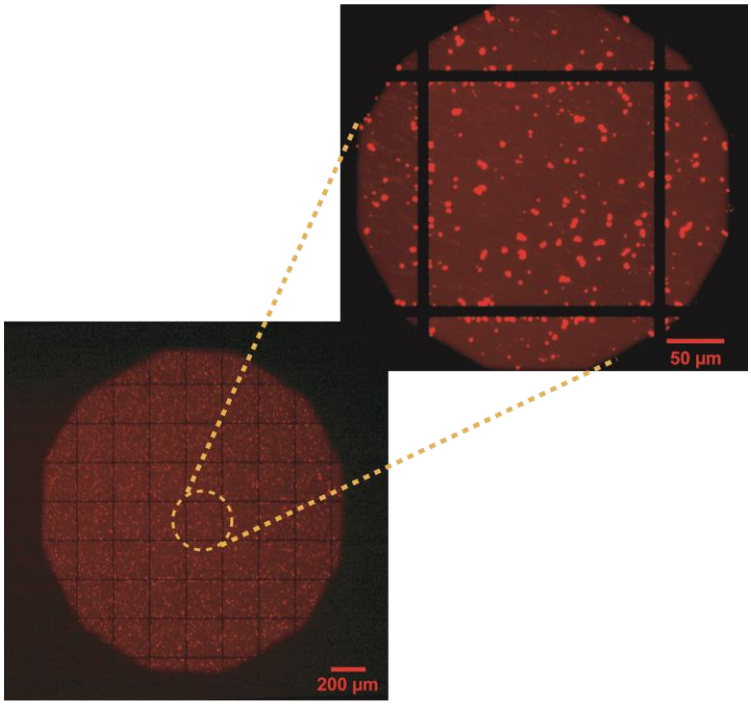

Fig. 6-1: Fluorescence microscopy image of a patterned supported membrane consisting of 98.5 mol% DMPC, 1 mol% DOGS-NTA and 0.5 mol% Biotinyl Cap DOPE functionalized with Alexa Fluor 633 streptavidin. The 200 x 200 µm² squares are bordered by diffusion barriers consisting of Cr/Ni with a height of 13 ± 2 nm and a width of 10 µm. The bright red dots correspond to protein clusters.

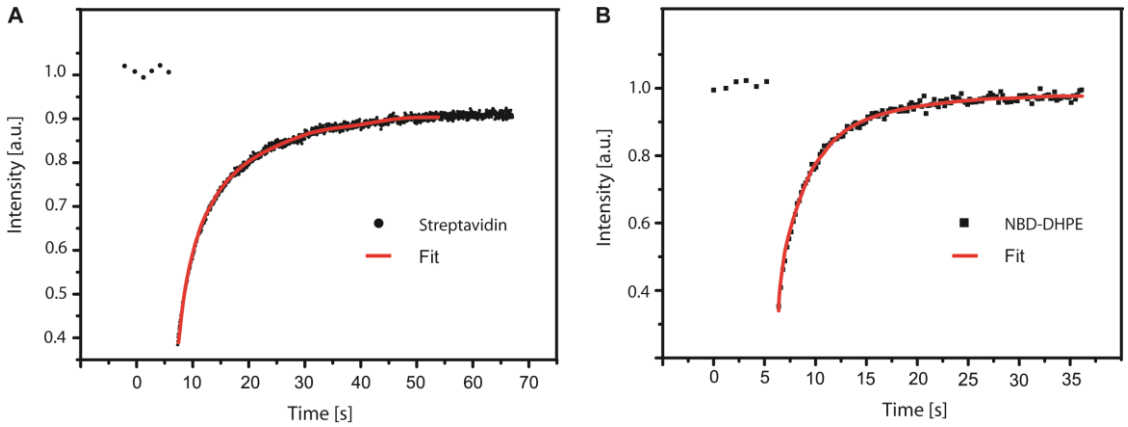

Fig. 6-2: Recovery of fluorescence intensity after photobleaching of (A) Alexa Fluor 633 streptavidin linked to Biotinyl Cap DOPE and (B) NBD-DHPE measured as substitute for non-fluorescent DOGS-NTA. Here, the supported membrane consists of 98.5 mol% DMPC, 1 mol% NBD-DHPE, and 0.5 mol% Biotinyl Cap DOPE.

Table 6-A: Diffusion coefficient and mobile fraction of Alexa Fluor 633 streptavidin linked to Biotinyl Cap DOPE and NBD-DHPE

	Diffusion coefficient D [µm²/s]	mobile fraction
Alexa Fluor 633 streptavidin linked to 0.5 mol% Biotinyl Cap DOPE	1.3 ± 0.4	0.83 ± 0.07
NBD-DHPE (1 mol%)	3.0 ± 0.4	0.96 ± 0.04

The diffusion coefficient of Alexa Fluor 633 streptavidin D_{Strept}: 1.3 ± 0.4 $\mu m^2 s^{-1}$ is comparable to the value of FITC labelled streptavidin (1.04 $\mu m^2 s^{-1}$) obtained by Han et al. [107] and the values of bound His-EGFP and His-DsReD (1.5 ± 0.1 $\mu m^2 s^{-1}$ and 1.4 ± 0.05 $\mu m^2 s^{-1}$, respectively) obtained by Tanaka et al..[60]

The FRAP result of NBD-DHPE was similar to the value of NBD-PE doped into a polymer-supported monolayer investigated by Tanaka et al..[60] The comparable diffusion coefficient and the high mobility of almost 100 % confirmed that there is no clustering to other lipids or streptavidin and the lipid mixing behaviour can be estimated to be ideal.

6.3. Electrical manipulation of membrane-anchored proteins

A patterned supported membrane containing 98.5 mol% DMPC, 1 mol% DOGS-NTA and 0.5 mol% Biotinyl Cap DOPE exhibiting Alexa Fluor 633 streptavidin was exposed to a lateral electrical field of 10 V/cm.

After 30 min, the concentration gradient reached steady state, as shown in Fig 6-3. Here, only the resulting steady-state concentration gradient of fluorescently labeled streptavidin is visualized due to the fact that DOGS-NTA is not fluorescent.

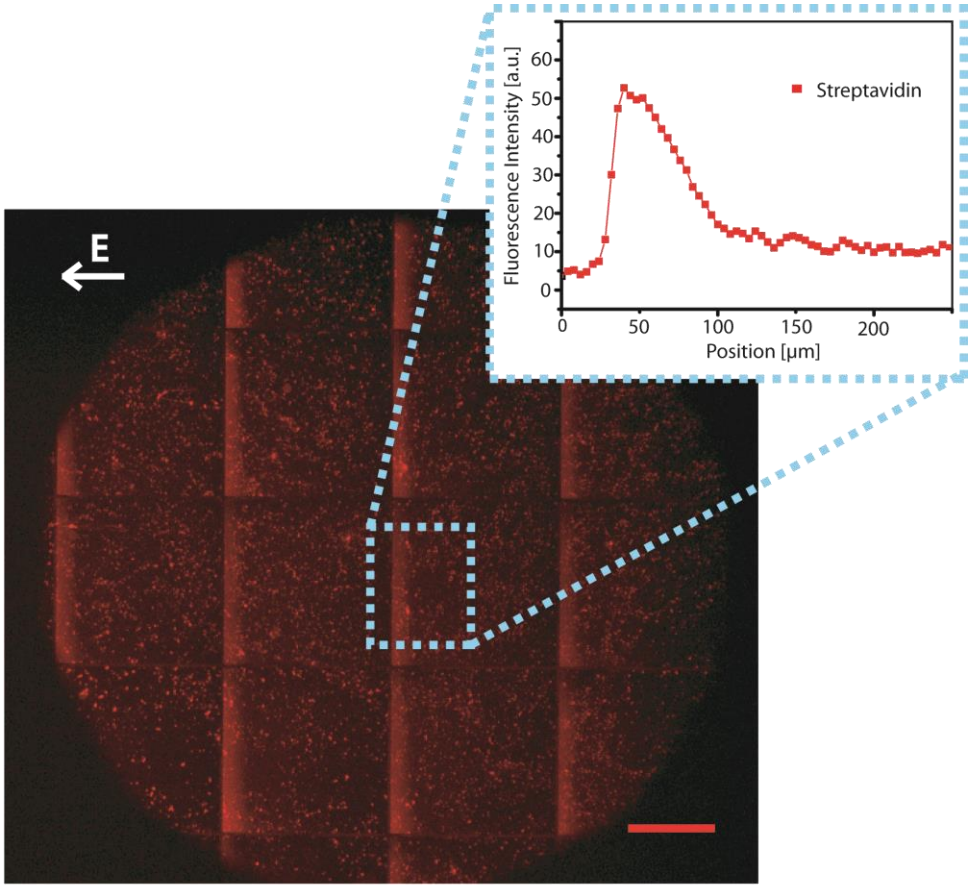

Fig. 6-3: A patterned supported membrane containing 98.5 mol% DMPC, 1 mol% DOGS-NTA and 0.5 mol% Biotinyl Cap DOPE exhibiting Alexa Fluor 633 streptavidin after applying an electric field of 10 V/cm for 30 min. The direction of the applied electric field (E) is indicated by a white arrow. The scale bar corresponds to 250 µm. The inset shows the two-dimensional intensity profile in the area of interest (blue dotted rectangle) which corresponds to the steady-state concentration gradient of streptavidin.

After the electric field was turned off the gradients were "frozen" by cooling the sample to temperatures (i.e. 4 °C) below the transition temperature T_m of the matrix lipid DMPC (T_m ~ 23°C). Subsequently, the supported membrane was incubated with His-GFP.

The resulting patterned supported membrane functionalized with two oppositely oriented protein gradients is shown in Fig. 6-4A. Alexa Fluor 633 streptavidin is shown in red and His-GFP in green. Fig. 6-4B shows the two-dimensional intensity profile of both membrane-anchored proteins in the region of interest, indicated by the blue dotted rectangle in Fig. 6-4A. The obtained steady state concentration gradients were analyzed empirically as described in the theoretical part (Chapter 3.6.1) to yield the characteristic decay length ξ. The resulting characteristic decay length for Alexa Fluor 633 streptavidin and DOGS-NTA (visualized with His-GFP) was 34.0 µm and 175.9 µm, respectively.

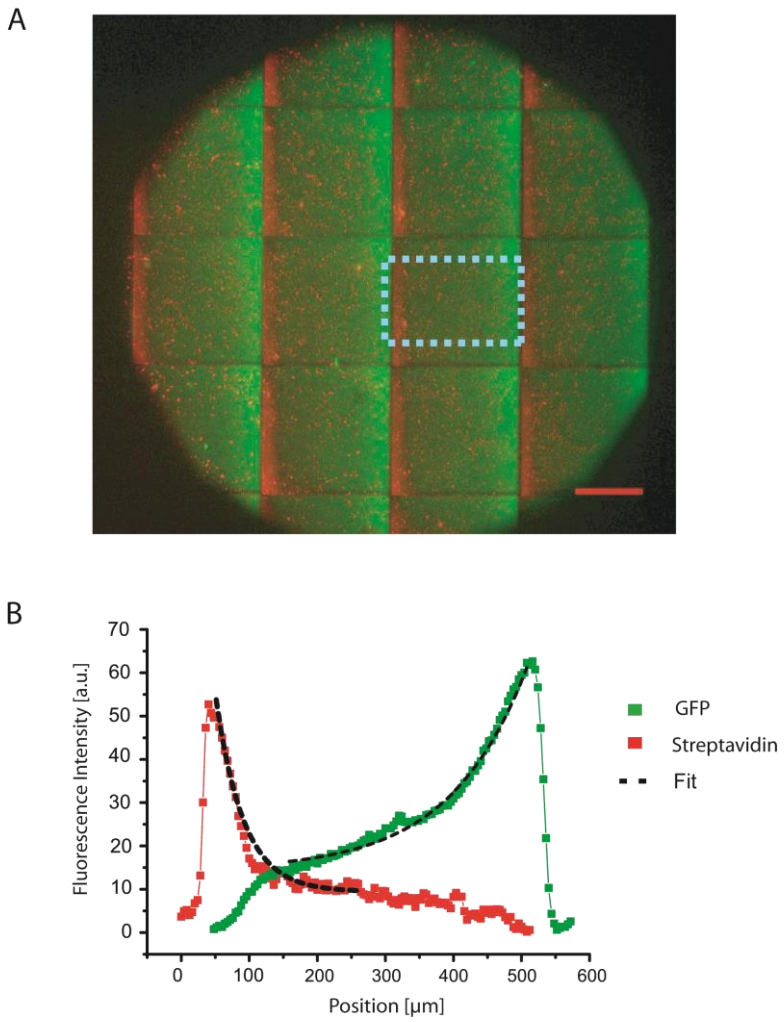

Fig 6-4: Two oppositely oriented protein gradients on patterned supported membranes. (A) Merged fluorescence microscopy image of the oppositely oriented static concentration gradients of membrane-anchored Alexa Fluor 633 streptavidin (red) and His-GFP (green). The scale bar corresponds to 250 µm. (B) Empirical analysis of the 2D intensity profile in the area of interest (blue dotted rectangle in A) leading to the characteristic decay lengths ξ.

Dividing the passive diffusion coefficients, obtained by FRAP measurements, D_{Strept} = 1.3 µm²s^{-1} and $D_{NBD \approx DOGS\text{-}NTA}$ = 3.0 µm²s^{-1}, by the corresponding characteristic decay lengths ξ, according to equation 3.75, resulted in the mean drift velocities of $\langle v \rangle_{Strept}$ = 38.2 nm/s and $\langle v \rangle_{DOGS\text{-}NTA}$ = 17.1 nm/s, respectively. The mean drift velocity of Alexa Fluor 633 streptavidin is comparable to the findings in other publications dealing with anchored proteins moved by the electroosmotic effect (described in Chapter 3.6.1).[60,106] In contrast $\langle v \rangle_{DOGS\text{-}NTA}$ is lower than the mean drift velocities obtained for fluorescent lipids NBD-DHPE ($\langle v \rangle_{NBD}$ = 39.9 nm/s) and TexasRed-DHPE ($\langle v \rangle_{Txred\text{-}DHPE\ (2\ mol\%)}$ = 58 nm/s)[60] which are driven by the electrophoretic effect (described in Chapter 3.6.1).

This lower drift velocity could be explained by the lower charge density of the Ni^{2+}-NTA complex (one negative charge distributed over the whole complex) of the DOGS-NTA compared to the other negatively charged lipids.

6.4. Fine-adjustable gradients: Interplay of electrophoresis and electroosmosis

Alexa Fluor 633 streptavidin consists of approximately three negatively charged Alexa Fluor 633 dyes covalently attached to streptavidin. The additional negative charges decrease the natural isoeletric point of streptavidin (pI_{Strept} = 5 - 5.5).[108] Consequently, Alexa Fluor 633 streptavidin carries a negative net charge at the condition (pH = 5.2) used in these experiments. The fact that negatively charged proteins are driven towards the negative electrode suggests that the contribution of electrophoresis is rather minor compared to the force from the bulk flow of positively charged ions (electroosmosis).

The magnitude of the electroosmotic flow scales linearly with the ζ-potential of the supported membrane surface (see equation 3.80 in Chapter 3.6.1). Therefore, the mean drift velocities of Alexa Fluor 633 streptavidin on the supported membranes should be adjustable by changing the fraction of charged lipids. To investigate this hypothesis, a set of experiments were carried out with different ratios of the negatively charged anchor lipid DOGS-NTA incorporated in the supported membrane (0 mol%, 1 mol% and 2 mol%). These different ratios yielded the characteristic decay length ξ of Alexa Fluor 633 streptavidin to be 42.6 µm, 34.0 µm, and 30.4 µm, respectively. The corresponding mean drift velocities were calculated as described in Chapter 3.6.1 by using the diffusion coefficient of Alexa Fluor 633 streptavidin D_{Strept}: 1.3 ± 0.4 $\mu m^2 s^{-1}$ (obtained by FRAP, Chapter 6.2). The obtained results, summarized in Table 6-B, show that the higher the mole fraction of negatively charged DOGS-NTA in the supported membrane is, the higher the mean drift velocity of streptavidin.

Table 6-B: Characteristic decay lengths and calculated mean drift velocities of supported membranes containing Alexa Fluor 633 streptavidin linked to Biotinyl Cap DOPE and 0 mol%, 1 mol% and 2 mol% DOGS-NTA.

	D [µm²/s]	ξ [µm]	v [nm/s]
Alexa Fluor 633 streptavidin linked to Biotinyl Cap DOPE	1.3	42.6	30.6
Alexa Fluor 633 streptavidin linked to Biotinyl Cap DOPE + DOGS-NTA (1 mol%)	1.3	34.0	38.2
Alexa Fluor 633 streptavidin linked to Biotinyl Cap DOPE + DOGS-NTA (2 mol%)	1.3	30.4	42.8

Furthermore, the gradient of DOGS-NTA (visualized with His-GFP) was investigated in membranes consisting of either DMPC and 1 mol% DOGS-NTA only, or with the addition of 0.5 mol% Biotinyl Cap DOPE and Alexa Fluor 633 streptavidin. By taking the diffusion coefficient of NBD-DHPE, as a comparable lipid, the mean drift velocities of 17.1 nm/s and 20.8 nm/s were calculated for membranes with and without Alexa Fluor 633 streptavidin, respectively. The results are summarized in table 6-C.

Table 6-C: Characteristic decay lengths and calculated mean drift velocities for supported membranes containing DMPC with 1 mol% DOGS-NTA only and with Alexa Fluor 633 streptavidin linked to 0.5 mol% Biotinyl Cap DOPE.

	D [µm²/s] (from NBD)	ξ [µm]	v [nm/s]
DOGS-NTA (1 mol%)	3.0	143.9	20.8
DOGS-NTA (1 mol%) + Alexa Fluor 633 streptavidin linked to 0.5 mol% Biotinyl Cap DOPE	3.0	175.9	17.1

The mean drift velocities of Alexa Fluor 633 streptavidin attached to supported membranes are higher if the ratio of negatively charged DOGS-NTA is increased (Table 6-B). In other words, the increasing amount of negatively charged lipids decreases the ζ-potential of the supported membrane and leads to a rise in the electroosmotic bulk of positively charged ions. This flow finally drives the protein towards the negative electrode.[60]

On the other hand, it is known that the electroosmotic flow of positive buffer ions leads to a frictional force which slows down negatively charged lipids in the membrane.[58,109] Consequently, the lower mean drift velocity of DOGS-NTA alone (20.8 nm/s) compared to membranes with Alexa Fluor 633 streptavidin linked to Biotinyl Cap DOPE (17.1 nm/s) is reasonable, assuming that the addition of 0.5 mol% Biotinyl Cap DOPE, possessing a negative net charge, changes the ζ-potential of the supported membrane to be more negative and thus increases the electroosmotic flow.

These findings confirm that the regulation of the drift velocity of Alexa Fluor 633 streptavidin and DOGS-NTA (coupled after membrane electrophoresis to His-GFP) can be regulated by adjusting the interplay between electrophoresis and electroosmosis.

6.5. Conclusion

In this chapter, a new method was developed to create fine-adjustable oppositely oriented concentration gradients of two proteins. As model system, a supported membrane exhibiting lipid anchors with biotin head group (Biotinyl Cap DOPE) or with NTA head group (DOGS-NTA), allowing for the coupling of the recombinant protein Alexa Fluor 633 streptavidin or His-GFP, respectively, was used.

First, the docking of Alexa Fluor 633 Streptavidin to the membrane, its subsequent mobility and passive lateral diffusion coefficient were investigated with fluorescence recovery after photobleaching (FRAP). The high mobility and the passive lateral diffusion coefficient of 1.3 ± 0.4 $\mu m^2 s^{-1}$ for streptavidin and 3.0 ± 0.4 $\mu m^2 s^{-1}$ for the anchor lipid DOGS-NTA were in good agreement with comparable results for mobile lipids or proteins linked to anchor lipids, ensuring a passive diffusion within the supported membrane.

Second, an electric field (membrane electrophoresis) was applied to form two oppositely directed static gradients of streptavidin and the anchor lipid DOGS-NTA. Here, the negatively charged Alexa Fluor 633 streptavidin was driven by the flow of positively charged buffer ions (electroosmosis) towards the negative electrode while the electrophoretic effect moved the negatively charged lipid DOGS-NTA in the opposite direction. Two stable, oppositely oriented protein gradients were finally achieved by decreasing the temperature below the transition temperature of the matrix lipid DMPC (< 23°C) and subsequent incubation with His-GFP.

Finally, these two gradients were demonstrated to be fine-adjustable by the interplay of electroosmotic flow of counter ions and electrophoresis.

7. Conclusions

The overall goal of this thesis is to develop a novel *in vitro* model system that allows for the quantitative control of cell differentiation processes in pluripotent tissue sheets.

In this study, pluripotent tissue sheets explanted from *Xenopus laevis*, called animal caps, were used as an example of tissue undergoing a change in cell polarity. As presented in Chapters 4 and 5, planar lipid membranes deposited on solid substrates were functionalized by the extracellular domain of *Xenopus* cadherin-11 Xcad 11), which plays key roles during the differentiation of neural crest cells (NCC).

In Chapter 4, the quantitative functionalization of supported membranes with Xcad-11 was carefully checked by specular X-ray reflectivity (XRR) and grazing incidence X-ray fluorescence (GIXF) experiments at the air/water interface. Using the electron density profiles and structural parameters obtained from XRR, the Ni^{2+} ion concentration profiles could be calculated from the Ni^{2+} Kα fluorescence emission measured by GIXF. The obtained Ni^{2+} ion-concentration profiles showed a remarkable accumulation of Ni^{2+} ions close to the lipid head groups, suggesting the yield of complex formation was more than 90 %. Moreover, GIXF was also utilized to detect the lateral density of Xcad-11 from S Kα fluorescence emission. The position of the maximal S-atom concentration was found at a distance of 68 ± 16 Å from the air/water interface, and the lateral concentration of S-atoms was obtained as $(2.7 \pm 0.3) \times 10^{-25}$ mol/nm^2.

Moreover, fine-structures of supported membranes in the presence and absence of Xcad-11 were characterized by high energy XRR, which could be treated as a uniform layer with a thickness of 126 Å and an electron density of 0.386 e × Å^{-3}. Quartz crystal microbalance with dissipation (QCM-D) experiments further confirmed that changes in mass density caused by the protein coupling were linearly proportional to the molar fraction of NTA lipids.

In Chapter 5, the interaction of *Xenopus* animal cap explants with supported membranes displaying Xcad-11 was systematically investigated as a function of the surface density of Xcad-11. A label-free micro-interferometry technique, reflection interference contrast microscopy (RICM), was utilized to investigate the vertical height fluctuation of tissue sheets in contact with substrates. According to the increase in the lateral density of Xcad-11, a distinct suppression of the height fluctuations and an increase in the adhesion area was observed. Simultaneous investigation of the explants labelled with membrane markers with fluorescence microscopy provided with complementary information if explants could sustain

lateral connections between cells. The combination of two microscopy techniques demonstrated that functionalized supported membranes with a lateral density of Xcad-11 of $<d> \sim 5.7$ nm serve as optimal surfaces for the stress-free immobilization of animal cap explants. Furthermore, the influence of cell-substrate adhesion (“out of plane”-interaction) on the sustainability of cell-cell connections (“in plane”) was verified by comparing "induced" tissues, wildtype tissues, and Xcad-11 knockout mutant tissues on membranes displaying different adhesion molecules. The specific NCC induction of the induced tissues (injected with Xfz7 and tBR) on supported membranes was confirmed using a GFP-labelled *slug*-promoter, which is expressed only during NCC differentiation.

In Chapter 6, a new method to create two opposite concentration gradients of two proteins (e.g. Wnt and BMP) was developed. The model system consists of a supported membrane containing lipid anchors with biotin head group (Biotinyl Cap DOPE) or with NTA head group (DOGS-NTA), allowing for the coupling of the recombinant protein streptavidin or His-GFP, respectively. In the first step, the two-dimensional fluidity of the supported membrane and linked proteins was measured by fluorescence recovery after photobleaching (FRAP) experiments, yielding the lateral diffusion coefficient of $1.3 \pm 0.4\ \mu m^2 s^{-1}$ for streptavidin. Two stable oppositely oriented, one-dimensional protein gradients could be achieved by applying a tangential electric field (membrane electrophoresis). After reaching to the steady-state, the concentration gradient could be stabilized by decreasing the temperature below the phase transition temperature of the matrix lipid. Furthermore, the opposite concentration gradients of two proteins can be fine-adjusted by the interplay of electrophoresis and electroosmotic flows of counter ions, suggesting that membranes displaying different protein gradients can potentially be used to spatially control the change in cell polarity.

The obtained results demonstrated a large potential of *in vitro* models based on supported membranes towards precise control of the fate of cells and tissues with distinct cues.

8. Outlook

The model systems established in this work are promising candidates to study and regulate the behavior of cohesive tissue sheets without disrupting their connective structure. To date, this achievement was not obtained in other studies on lipid membrane-based model systems.

In particular, supported membranes displaying two opposite concentration gradients of two proteins might be convenient tools to regulate many biological developmental steps (e.g. neural crest development) which occur as result of successive or simultaneous activation or inhibition molecule (e.g. Wnt, BMP) gradients. In this thesis, the supported membranes were patterned by means of barriers to the thermal diffusion and electrical drift of lipids. Here, the lipid composition and membrane functionalization in every square was identical for the entire substrate. In the future, cohesive tissue sheets might be immobilized and investigated on patterned substrate exhibiting different contents in every square. In this way, the influence of different protein concentrations or gradient slopes can be investigated simultaneously on the same cohesive tissue sheet. Three examples for patterned substrates with different lipid and protein contents in various squares are illustrated in Fig. 8-1: (A) Squares of homogenously functionalized membranes showing different ligand concentrations, (B) supported membranes functionalized with one protein, exhibiting different gradients in each square and (C) supported membranes functionalized with two different proteins, exhibiting different gradients in every square.

The obtained results will give more detailed information about the influence of different ligands coupled to supported membranes.

Furthermore, the established cell-surface models could be used for the investigation of single cells or tissues of many other biological systems (such as human, mouse, etc...). For this purpose, the protein gradients of the models would have to be kept constant for several hours at higher temperatures (≈ 37 °C). To increase the stability of the gradient, the matrix-lipid DMPC (with a transition temperature (T_m) of 23 °C) would be exchanged by DPPC which exhibits a higher T_m (= 42 °C).

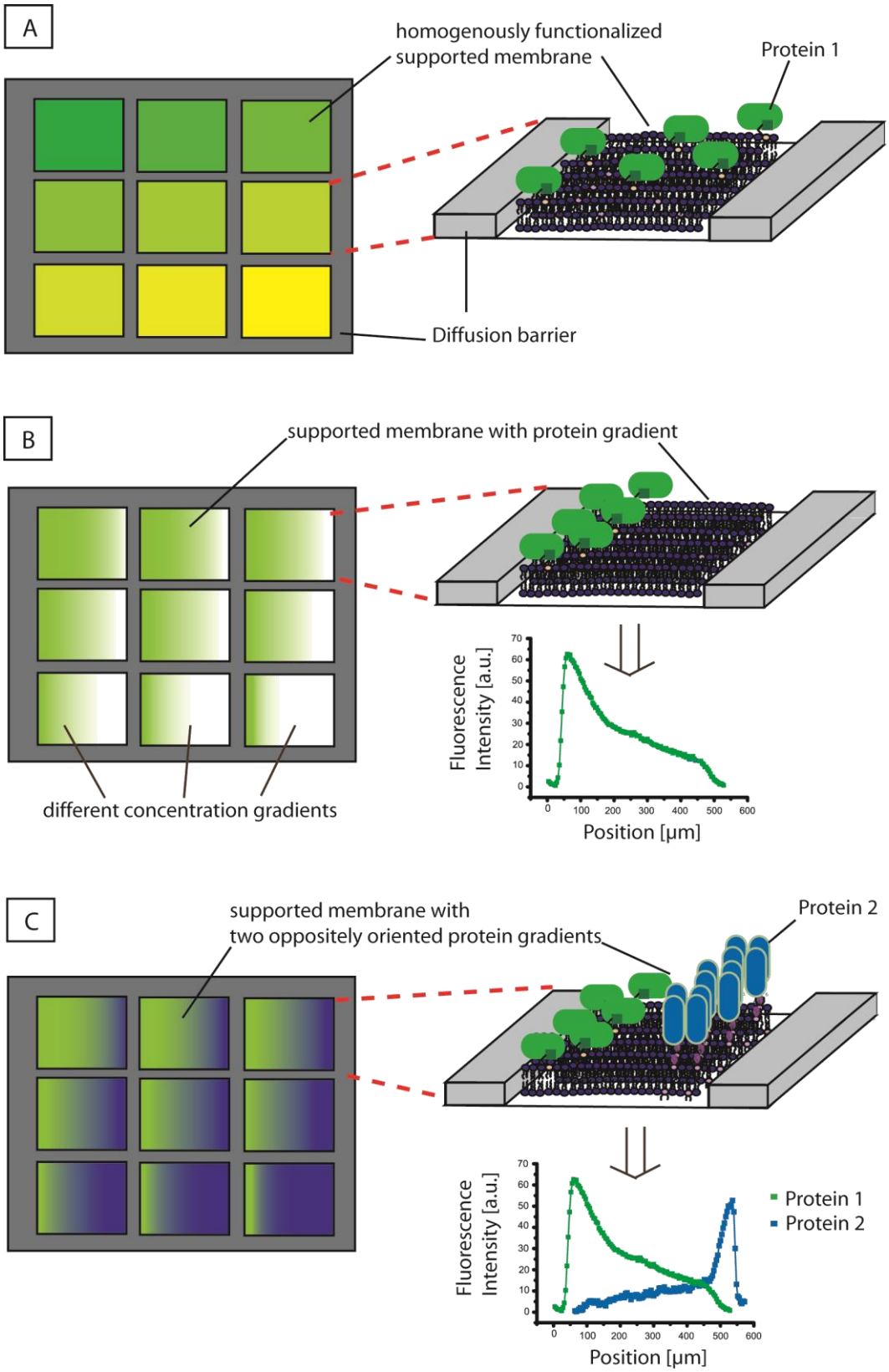

Fig. 8-1: Schematic illustration of three examples for patterned substrates with (A) squares of homogenously functionalized membranes with different protein concentration, (B) supported membranes functionalized with one protein exhibiting different gradients in each square and (C) supported membranes functionalized with two proteins which are exhibiting different gradients in every square. The lipid composition determines the slope of the protein gradients (B,C).

Appendix

A.1 Structure of the corrals on patterned substrates

A scanning electron microscope (SEM) was used to visualize the barriers on patterned glass substrates created as described in Chapter 2.2.2. As illustrated in Fig. A.1-1, the patterns are squares with clear edges and without remarkable defects.

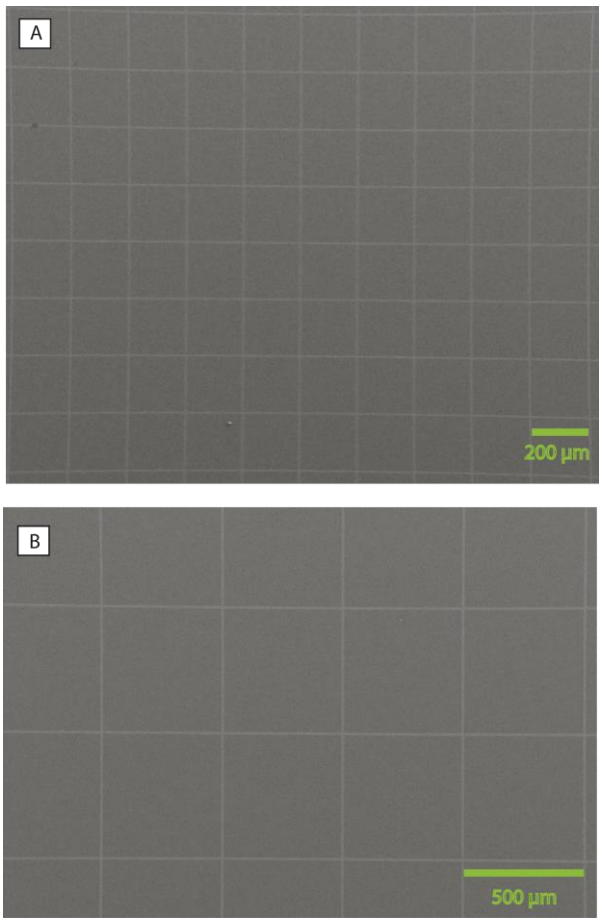

Fig. A.1-1: Scanning electron microscopy (SEM) image of patterned substrates. Squares with the corral size of 200 × 200 µm (A) and 500 × 500 µm (B) are demonstrated to exhibit clear edges without defects.

A.2 Structure of Cr/Ni-barriers

Atomic force microscopy (AFM) experiments were performed to obtain detailed information about the structure of the Cr/Ni-barriers. As illustrated in Fig. A.2-1, a line profile across the barrier (blue line in Fig A.2-2B) pointed out the sharp edge of the barriers (see red arrows in Fig. A.2-1C). Moreover, the width and height of the barrier are demonstrated to be 10 µm and 13 ± 2 µm, respectively.

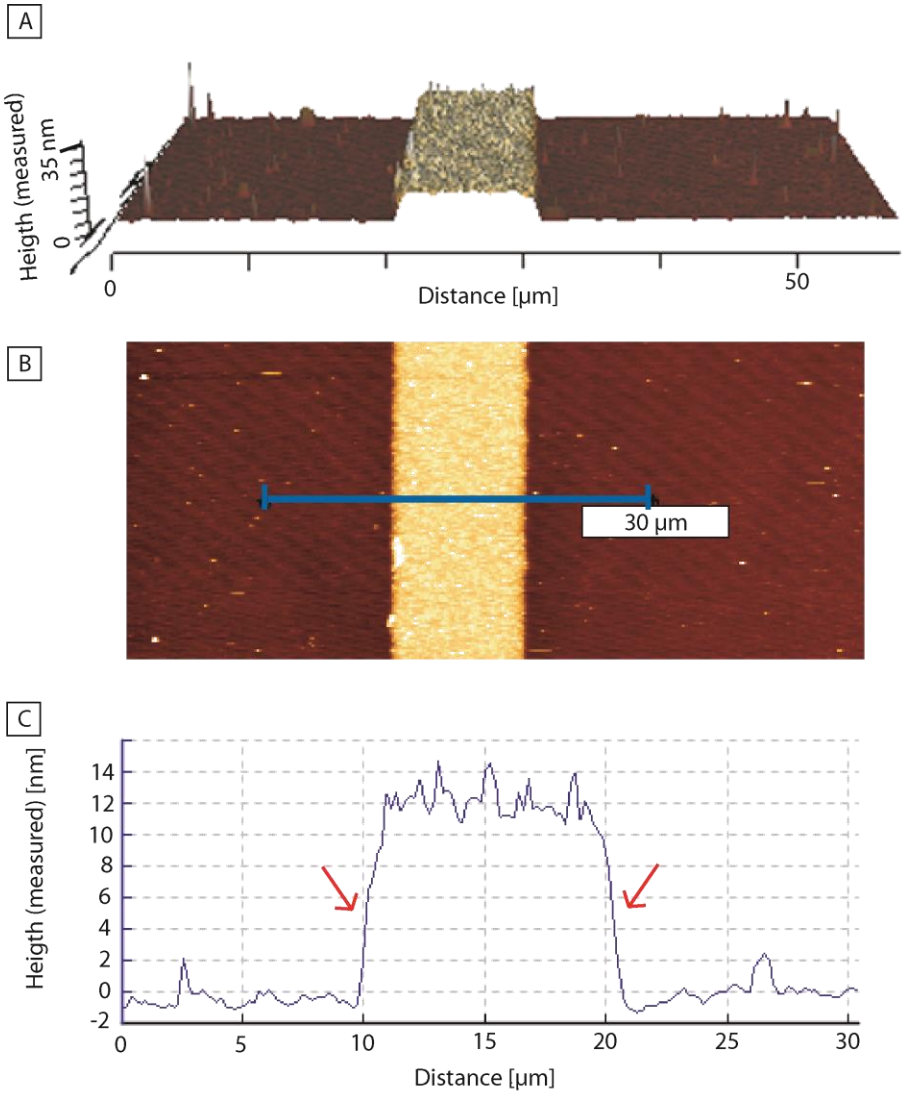

Fig. A.2-1: Atomic force microscopy (AFM) image of Cr/Ni-barrier. (A) Three-dimensional view of measured height profile. (B) Two-dimensional image of the measured height profile. The blue line across the barrier corresponds to a length of 30 µm. (C) Measured height corresponding to the profile of the blue line across in (B). The width of the Cr/Ni-barrier is clear defined (= 10 µm) and their edges (see red arrows) are sharp. The height of the barrier is 13 ± 2 µm.

A.3 Background subtraction

The specular reflectivity was obtained by integrating the pixel intensity near the specular plane (between the black lines, Fig. A.3-1). The background is obtained by averaging the integrated off-specular intensity (between the gray and black lines, Fig. A.3-1) and then subtracted from the specular intensity.

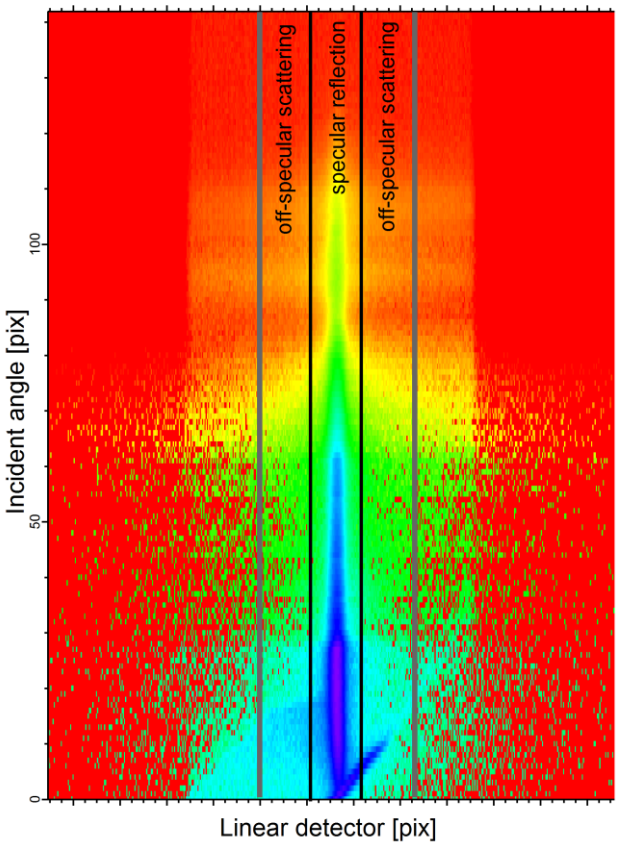

Fig. A.3-1: XRR raw data of a SOPC monolayer doped with 50 mol% DOGS-NTA corresponding to Fig. 4-2 in Chapter 4.2.1.

A.4 Pressure-area isotherms of SOPC/DOGS-NTA monolayers

To gain the average area per molecule isotherms of SOPC/DOGS-NTA monolayers with different molar fractions of DOGS-NTA (Φ_{DGS}) were measured (Fig. A.4-1). The dotted line in Fig. A.4-1 indicates the average area per molecule at a surface pressure of 20 mN/m corresponding to the molar fraction. The obtained mean areas per molecule for different mole fractions at different surface pressures are shown in Fig. A.4-1B. Since the average area per molecule in mixed monolayers linearly scales with Φ_{DGS} at different surface pressure, $A_{mixed} = \Phi_{DGS} \times A_{DGS} + (1 - \Phi_{DGS}) \times A_{SOPC}$, mixed monolayers can be treated as ideal mixtures.

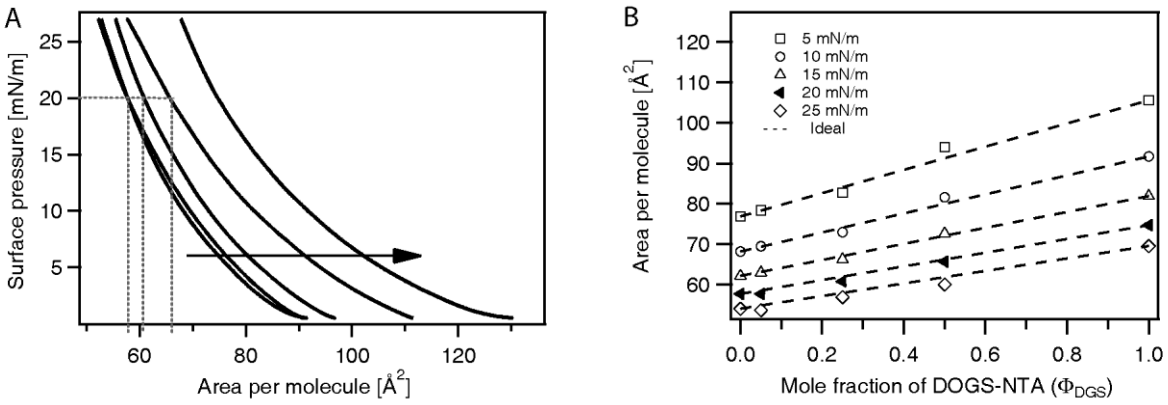

Fig. A.4-1 (A) Isotherms of SOPC/DOGS-NTA monolayers with increasing molar fractions of DOGS-NTA (Φ_{DGS}) from left to right (0; 0.05; 0.25; 0.5; 1). The dotted line indicates the average area per molecule corresponding to the molar fraction at a surface pressure of 20 mN/m. (B) The mean area per molecule for different molar fractions at a surface pressure of 5 mN/m (open squares), 10 mN/m (open circles), 15 mN/m (open triangles), 20 mN/m (solid triangles) and 25 mN/m (open diamonds). The dotted line corresponds to the case of an ideal mixture.

A.5 Quantitative determination of the Ni^{2+}-NTA complex binding stoichiometry

To estimate the number of Ni^{2+} ions associated with one DOGS-NTA lipid, the fluorescence signal from the Ni-loaded buffer was utilized as the reference. The fluorescnce intensity in the presence of a SOPC/DOGS-NTA monolayer on Ni^{2+}-free buffer can be given as:

$$I_M = k \times A \times I_0 \times c_{lat} \times \int_0^d e^{-\frac{z}{D(\alpha)}} dz\,, \tag{A.5-1}$$

where *k is* a proportionality constant, *A* the detector area, I_0 the incident beam intensity, c_{lat} is the lateral concentration of Ni^{2+} ions near the interface and D (α) is the penetration depth. If one assumes the re-absorption, equation A.5-1 can be modified as:

$$I_M = k \times A \times I_0 \times c_{lat} \times \int_0^d e^{-z\left(\frac{1}{D(\alpha)}+\frac{1}{L_i}\right)} dz\,, \tag{A.5-2}$$

where L_i is the attenuation length of water at the characteristic fluorescence line.

The fluorescence intensity of the blank buffer is:

$$\begin{aligned} I_B &= k \times A \times I_0 \times c_0 \times \int_0^\infty e^{-z\left(\frac{1}{D(\alpha)}+\frac{1}{L_i}\right)} dz \\ &= k \times A \times I_0 \times c_0 \times D(\alpha) \times \frac{L_i}{(D(\alpha)+L_i)} \end{aligned} \tag{A.5-3}$$

From equation A.5-2 and A.5-3 the ratio of I_M / I_B is

$$\frac{I_M}{I_B} = \frac{c_{lat}\left\{1 - e^{-d\left(\frac{1}{D(\alpha)}+\frac{1}{L_i}\right)}\right\}}{c_0} \tag{A.5-4}$$

Thus, the fluorescence intensities from Fig. A.5-1A and the values of d, c_0 and $L_{i,}$ given in the thesis, can be used to calculate c_{lat}. Finally the the number of Ni^{+2} ions associated with one DOGS-NTA N can be given by:

$$N = \frac{A_{per} \times d \times c_{lat}}{\chi}, \qquad \text{(A.5-5)}$$

where A_{per} is the area per lipid molecule and χ is the molar fraction of DOGS-NTA. This yields N = 0.91 ± 0.25 Ni^{2+} ions per DOGS-NTA molecule.

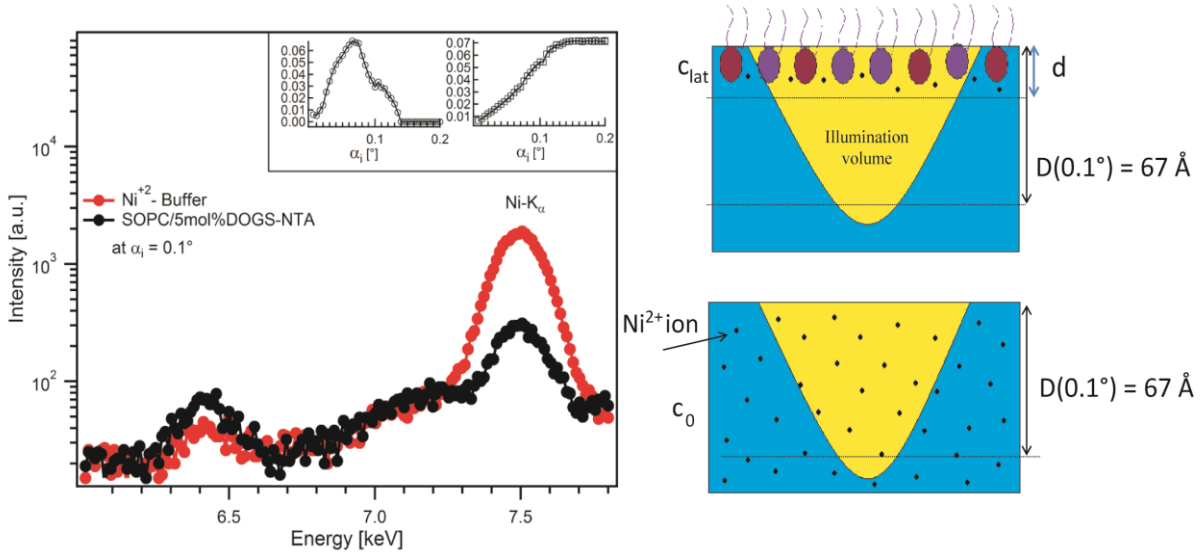

Fig. A.5-1 (A) GIXF spectra of Ni^{2+}-loaded buffer in the presence (black) and absence (red) of a SOPC monolayer doped with 5 mol% DOGS-NTA, measured at α_i = 0.1°. The inset shows a comparison of Ni Kα signals (7.5keV) from Ni^{2+}-free (left) and Ni^{2+}-loaded (right) buffer. (B) A schematic presentation of Ni^{2+} ions in the illumination volume in the presence (top) and absence (bottom) of a lipid monolayer.

Abbreviations

Biotinyl Cap DOPE	1,2-dioleoyl-sn-glycero-3-phosphoethanolamine-N-(cap biotinyl)
BMP	bone morphogenic protein
DMPC	1,2-dimyristoyl-sn-glycero-3-phosphocholine
DOGS-NTA	1,2-dioleoyl-sn-glycero-3-[(N-(5-amino-1-carboxypentyl)-iminodiacetic acid)succinyl]
EC	extracellular domain
Ecad	epithelial cadherin
EMT	epithelial-to-mesenchymal transition
ESRF	European Synchrotron Radiation Facility
FGF	fibroblast growth factor
FRAP	fluorescence recovery after photobleaching
GIXF	grazing incidence X-ray fluorescence
h	hours
hAGT	O6-alkylguanine-DNA alkyl transferase
HBS	hepes buffered saline
His-GFP	histidine-tagged green fluorescent protein
INA	illumination numerical aperture
MBSH	modified Barth solution holding
min	minutes
NA	numerical aperture
NBD-DHPE	N-(7-nitrobenz-2-oxa-1,3-diazol-4-yl)-1,2-dihexadecanoyl-sn-glycero-3-phosphoethanolamine
NCC	neural crest cell
NTA	nitrilotriacetic acid
QCM-D	quartz crystal microbalance with dissipation
RICM	reflection interference contrast microscopy
RGD	tripeptide composed of L-arginine, glycine, and L-aspartic acid
sec	seconds
SOPC	1- stearoyl-2-oleoyl-sn-glycero-3-phosphocholine

SUV	small unilamellar vesicles
SLD	scattering length density
tBR	truncated bone morphogenetic protein receptor
Wnt	Wingless/INT-related
Xcad-11	*Xenopus* cadherin-11
Xcad-11 MO	antisense Xcad-11 morpholinos
XRR	specular X-ray reflectivity
XFz7	*Xenopus* Frizzled 7

d	thickness
ρ	electron density
σ	root mean square (rms) roughness
D	dissipation factor
Δf	frequency change
T_m	transition temperature
ξ	characteristic decay length
$<v>$	mean drift velocity

Bibliography

(1) Huang, X.; Saint-Jeannet, J. P. Induction of the Neural Crest and the Opportunities of Life on the Edge *Dev Biol* **2004**, *275*, 1-11.

(2) Mayor, R.; Morgan, R.; Sargent, M. G. Induction of the Prospective Neural Crest of Xenopus *Development* **1995**, *121*, 767-77.

(3) LaBonne, C.; Bronner-Fraser, M. Neural Crest Induction in Xenopus: Evidence for a Two-Signal Model *Development* **1998**, *125*, 2403-2414.

(4) Staveley, B. E.; http://www.mun.ca/biology/desmid/brian/BIOL3530/DEVO_03/ch03f03.jpg, Ed. 2013.

(5) Guille, M.; Green, J. In *Molecular Methods in Developmental Biology*; Humana Press: 1999; Vol. 127, p 1-13.

(6) Thiery, J. P.; Sleeman, J. P. Complex Networks Orchestrate Epithelial-Mesenchymal Transitions *Nature Reviews Molecular Cell Biology* **2006**, *7*, 131-142.

(7) Theveneau, E.; Mayor, R. Neural Crest Delamination and Migration: From Epithelium-to-Mesenchyme Transition to Collective Cell Migration *Developmental Biology* **2012**, *366*, 34-54.

(8) Wheelock, M. J.; Johnson, K. R. Cadherins as Modulators of Cellular Phenotype *Annu Rev Cell Dev Biol* **2003**, *19*, 207-35.

(9) Nagar, B.; Overduin, M.; Ikura, M.; Rini, J. M. Structural Basis of Calcium-Induced E-Cadherin Rigidification and Dimerization *Nature* **1996**, *380*, 360-4.

(10) Overduin, M.; Harvey, T. S.; Bagby, S.; Tong, K. I.; Yau, P.; Takeichi, M.; Ikura, M. Solution Structure of the Epithelial Cadherin Domain Responsible for Selective Cell Adhesion *Science* **1995**, *267*, 386-9.

(11) Shapiro, L.; Fannon, A. M.; Kwong, P. D.; Thompson, A.; Lehmann, M. S.; Grubel, G.; Legrand, J. F.; Als-Nielsen, J.; Colman, D. R.; Hendrickson, W. A. Structural Basis of Cell-Cell Adhesion by Cadherins *Nature* **1995**, *374*, 327-37.

(12) Gumbiner, B. M. Regulation of Cadherin-Mediated Adhesion in Morphogenesis *Nat Rev Mol Cell Biol* **2005**, *6*, 622-34.

(13) Shindo, A.; Hara, Y.; Yamamoto, T. S.; Ohkura, M.; Nakai, J.; Ueno, N. Tissue-Tissue Interaction-Triggered Calcium Elevation Is Required for Cell Polarization During Xenopus Gastrulation *PLoS One* **2010**, *5*.

(14) Hadeball, B.; Borchers, A.; Wedlich, D. Xenopus Cadherin-11 (Xcadherin-11) Expression Requires the Wg/Wnt Signal *Mechanisms of Development* **1998**, *72*, 101-113.

(15) Shindo, A.; Yamamoto, T. S.; Ueno, N. Coordination of Cell Polarity During Xenopus Gastrulation *PLoS One* **2008**, *3*, 8.

(16) Schmitt, L.; Dietrich, C.; Tampe, R. Synthesis and Characterization of Chelator-Lipids for Reversible Immobilization of Engineered Proteins at Self-Assembled Lipid Interfaces *J. Am. Chem. Soc.* **1994**, *116*, 8485-8491.

(17) Dorn, I. T.; Pawlitschko, K.; Pettinger, S. C.; Tampe, R. Orientation and Two-Dimensional Organization of Proteins at Chelator Lipid Interfaces *Biological Chemistry* **1998**, *379*, 1151-1159.

(18) Brian, A. A.; McConnell, H. M. Allogeneic Stimulation of Cytotoxic T Cells by Supported Planar Membranes *Proceedings of the National Academy of Sciences of the United States of America* **1984**, *81*, 6159-6163.

(19) Grakoui, A.; Bromley, S. K.; Sumen, C.; Davis, M. M.; Shaw, A. S.; Allen, P. M.; Dustin, M. L. The Immunological Synapse: A Molecular Machine Controlling T Cell Activation *Science* **1999**, *285*, 221-227.

(20) Miller, C. E.; Majewski, J.; Gog, T.; Kuhl, T. L. Characterization of Biological Thin Films at the Solid-Liquid Interface by X-Ray Reflectivity *Phys. Rev. Lett.* **2005**, *94*.

(21) Schubert, T.; Seitz, P. C.; Schneck, E.; Nakamura, M.; Shibakami, M.; Funari, S. S.; Konovalov, O.; Tanaka, M. Structure of Synthetic Transmembrane Lipid Membranes at the Solid/Liquid Interface Studied by Specular X-Ray Reflectivity *Journal of Physical Chemistry B* **2008**, *112*, 10041-10044.

(22) Yun, W. B.; Bloch, J. M. X-Ray near Total External Fluorescence Method: Experiment and Analysis *Journal of Applied Physics* **1990**, *68*, 1421-1428.

(23) Novikova, N. N.; Yurieva, E. A.; Zheludeva, S. I.; Kovalchuk, M. V.; Stepina, N. D.; Tolstikhina, A. L.; Gaynutdinov, R. V.; Urusova, D. V.; Matkovskaya, T. A.; Rubtsov, A. M.; Lopina, O. D.; Erko, A. I.; Konovalov, O. V. X-Ray Fluorescence Methods for Investigations of Lipid/Protein Membrane Models *J Synchrotron Radiat* **2005**, *12*, 511-6.

(24) Schneck, E.; Schubert, T.; Konovalov, O. V.; Quinn, B. E.; Gutsmann, T.; Brandenburg, K.; Oliveira, R. G.; Pink, D. A.; Tanaka, M. Quantitative Determination of Ion Distributions in Bacterial Lipopolysaccharide Membranes by Grazing-Incidence X-Ray Fluorescence *PNAS* **2010**, *107*, 9147-51.

(25) Keller, C. A.; Kasemo, B. Surface Specific Kinetics of Lipid Vesicle Adsorption Measured with a Quartz Crystal Microbalance *Biophysical Journal* **1998**, *75*, 1397-1402.

(26) Rossetti, F. F.; Bally, M.; Michel, R.; Textor, M.; Reviakine, I. Interactions between Titanium Dioxide and Phosphatidyl Serine-Containing Liposomes: Formation and Patterning of Supported Phospholipid Bilayers on the Surface of a Medically Relevant Material *Langmuir* **2005**, *21*, 6443-6450.

(27) Borchers, A.; David, R.; Wedlich, D. Xenopus Cadherin-11 Restrains Cranial Neural Crest Migration and Influences Neural Crest Specification *Development* **2001**, *128*, 3049-3060.

(28) Kashef, J.; Köhler, A.; Kuriyama, S.; Alfandari, D.; Mayor, R.; Wedlich, D. Cadherin-11 Regulates Protrusive Activity in Xenopus Cranial Neural Crest Cells Upstream of Trio and the Small Gtpases *Genes & Development* **2009**, *23*, 1393-1398.

(29) Juillerat, A.; Gronemeyer, T.; Keppler, A.; Gendreizig, S.; Pick, H.; Vogel, H.; Johnsson, K. Directed Evolution of O6-Alkylguanine-DNA Alkyltransferase for Efficient Labeling of Fusion Proteins with Small Molecules in Vivo *Chemistry & Biology* **2003**, *10*, 313-317.

(30) Nieuwkoop, P. D.; Faber, J. *Normal Table of Xenopus Laevis-Daudin. A Systematical and Chronological Survey of the Development from the Fertilized Egg Till the End of Metamorphosis. Edited by P.D. Nieuwkoop and J. Faber. Issued by the Hubrecht Laboratory, Utrecht. [with a Bibliography.]*; North-Holland Publishing Company, 1956.

(31) Kern, W.; Puotinen, D. A. Cleaning Solutions Based on Hydrogen Peroxide for Use in Silicon Semiconductor Technology *RCA Review* **1970**, *31*, 187-206.

(32) Russel, T. P. X-Ray and Neutron Reflectivity for the Investigation of Polymers *Materials Science Reports* **1990**, *5*, 171-271.

(33) Parratt, L. G. Surface Studies of Solids by Total Reflection of X-Rays *Physical Review* **1954**, *95*, 359-369.

(34) Névot, L.; Croce, P. Caractérisation Des Surfaces Par Réflexion Rasante De Rayons X. Application À L'étude Du Polissage De Quelques Verres Silicates *Rev. Phys. Appl. (Paris)* **1980**, *15*, 761-779.
(35) Nelson, A. Co-Refinement of Multiple-Contrast Neutron/X-Ray Reflectivity Data Using Motofit *Journal of Applied Crystallography* **2006**, *39*, 273-276.
(36) Abuillan, W.; Vorobiev, A.; Hartel, A.; Jones, N. G.; Engstler, M.; Tanaka, M. Quantitative Determination of the Lateral Density and Intermolecular Correlation between Proteins Anchored on the Membrane Surfaces Using Grazing Incidence Small-Angle X-Ray Scattering and Grazing Incidence X-Ray Fluorescence *The Journal of Chemical Physics* **2012**, *137*, 204907-8.
(37) Ohta, K.; Ishida, H. Matrix Formalism for Calculation of Electric Field Intensity of Light in Stratified Multilayered Films *Appl. Opt.* **1990**, *29*, 1952-1959.
(38) Abeles, F. Recherche Sur La Propagation Des Ondes Electromagnetiques Sinusoidales Dans Les Milieux Stratifies. Applications Aux Couches Minces *Ann. Phys. Paris* **1950**, *5*, 596-640, 706-782.
(39) Boggs, P. T.; Donaldson, J. R.; Byrd, R. H.; Schnabel, R. B. Odrpack - Software for Weighted Orthogonal Distance Regression *Acm Transactions on Mathematical Software* **1989**, *15*, 348-364.
(40) Sauerbrey, G. Verwendung Von Schwingquarzen Zur Wägung Dünner Schichten Und Zur Mikrowägung *Zeitschrift für Physik A Hadrons and Nuclei* **1959**, *155*, 206-222.
(41) Rodahl, M.; Hook, F.; Krozer, A.; Brzezinski, P.; Kasemo, B. Quartz-Crystal Microbalance Setup for Frequency and Q-Factor Measurements in Gaseous and Liquid Environments *Review of Scientific Instruments* **1995**, *66*, 3924-3930.
(42) Hook, F.; Rodahl, M.; Brzezinski, P.; Kasemo, B. Energy Dissipation Kinetics for Protein and Antibody-Antigen Adsorption under Shear Oscillation on a Quartz Crystal Microbalance *Langmuir* **1998**, *14*, 729-734.
(43) Larsson, C.; Rodahl, M.; Hook, F. Characterization of DNA Immobilization and Subsequent Hybridization on a 2d Arrangement of Streptavidin on a Biotin-Modified Lipid Bilayer Supported on Sio2 *Anal. Chem.* **2003**, *75*, 5080-5087.
(44) Keller, C. A.; Glasmastar, K.; Zhdanov, V. P.; Kasemo, B. Formation of Supported Membranes from Vesicles *Phys. Rev. Lett.* **2000**, *84*, 5443-5446.
(45) Abercrombie, M.; Ambrose, E. J. Interference Microscope Studies of Cell Contacts in Tissue Culture *Exp. Cell Res* **1958**, *15*, 332-345.
(46) Curtis, A. S. G. The Mechanism of Adhesion of Cells to Glass. A Study by Interference Reflection Microscopy *Jour Cell Biol* **1964**, *20*, 199-215.
(47) Ploem, J. S. *Reflection-Contrast Microscopy as a Tool for Investigation of the Attachment of Living Cells to a Glass Surface*; Blackwell Scientific Oxford, 1975.
(48) Gingell, D.; Todd, I. Interference Reflection Microscopy a Quantitative Theory for Image Interpretation and Its Application to Cell Substratum Separation Measurement *Biophysical Journal* **1979**, *26*, 507-526.
(49) Rädler, J.; Sackmann, E. Imaging Optical Thicknesses and Separation Distances of Phospholipid-Vesicles at Solid-Surfaces *Journal De Physique II* **1993**, *3*, 727-748.
(50) Wiegand, G.; Neumaier, K. R.; Sackmann, E. Microinterferometry: Three-Dimensional Reconstruction of Surface Microtopography for Thin-Film and

Wetting Studies by Reflection Interference Contrast Microscopy (Ricm) *Applied Optics* **1998**, *37*, 6892-6905.

(51) Born, M.; Wolf, E. *Principles of Optics*; 7 th ed.; Cambridge University Press Cambridge; UK, 1999.

(52) Limozin, L.; Sengupta, K. Quantitative Reflection Interference Contrast Microscopy (Ricm) in Soft Matter and Cell Adhesion *Chemphyschem* **2009**, *10*, 2752-2768.

(53) Einstein, A. Über Die Von Der Molekularkinetischen Theorie Der Wärme Geforderte Bewegung Von in Ruhenden Flüssigkeiten Suspendierten Teilchen *Annalen der Physik* **1905**, *322*, 549-560.

(54) Saffman, P. G.; Delbrück, M. Brownian Motion in Biological Membranes *Proceedings of the National Academy of Sciences* **1975**, *72*, 3111-3113.

(55) Evans, E.; Sackmann, E. Translational and Rotational Drag Coefficients for a Disk Moving in a Liquid Membrane Associated with a Rigid Substrate *Journal of Fluid Mechanics* **1988**, *194*, 553-561.

(56) Axelrod, D.; Koppel, D. E.; Schlessinger, J.; Elson, E.; Webb, W. W. Mobility Measurement by Analysis of Fluorescence Photobleaching Recovery Kinetics *Biophysical Journal* **1976**, *16*, 1055-1069.

(57) Soumpasis, D. M. Theoretical Analysis of Fluorescence Photobleaching Recovery Experiments *Biophysical Journal* **1983**, *41*, 95-97.

(58) Stelzle, M.; Miehlich, R.; Sackmann, E. 2-Dimensional Microelectrophoresis in Supported Lipid Bilayers *Biophysical Journal* **1992**, *63*, 1346-1354.

(59) McLaughlin, S.; Poo, M. M. The Role of Electro Osmosis in the Electric Field Induced Movement of Charged Macro Molecules on the Surfaces of Cells *Biophysical Journal* **1981**, *34*, 85-94.

(60) Tanaka, M.; Hermann, J.; Haase, I.; Fischer, M.; Boxer, S. G. Frictional Drag and Electrical Manipulation of Recombinant Proteins in Polymer-Supported Membranes *Langmuir* **2007**, *23*, 5638-5644.

(61) Bayer, E. A.; Rivnay, B.; Skutelsky, E. On the Mode of Liposome Cell Interactions Biotin Conjugated Lipids as Ultrastructural Probes *Biochimica et Biophysica Acta* **1979**, *550*, 464-473.

(62) Blankenburg, R.; Meller, P.; Ringsdorf, H.; Salesse, C. Interaction between Biotin Lipids and Streptavidin in Monolayers - Formation of Oriented Two-Dimensional Protein Domains Induced by Surface Recognition *Biochemistry* **1989**, *28*, 8214-8221.

(63) Körner, A.; Abuillan, W.; Deichmann, C.; Rossetti, F. F.; Köhler, A.; Konovalov, O. V.; Wedlich, D.; Tanaka, M. Quantitative Determination of Lateral Concentration and Depth Profile of Histidine-Tagged Recombinant Proteins Probed by Grazing Incidence X-Ray Fluorescence *The Journal of Physical Chemistry B* **2013**, *117*, 5002-5008.

(64) Malkova, S.; Long, F.; Stahelin, R. V.; Pingali, S. V.; Murray, D.; Cho, W. H.; Schlossman, M. L. X-Ray Reflectivity Studies of Cpla(2)Alpha-C2 Domains Adsorbed onto Langmuir Monolayers of Sopc *Biophysical Journal* **2005**, *89*, 1861-1873.

(65) Padmanabhan, V.; Daillant, J.; Belloni, L.; Mora, S.; Alba, M.; Konovalov, O. Specific Ion Adsorption and Short-Range Interactions at the Air Aqueous Solution Interface *Physical Review Letters* **2007**, *99*, 086105.

(66) Hochuli, E.; Döbeli, H.; Schacher, A. New Metal Chelate Adsorbent Selective for Proteins and Peptides Containing Neighbouring Histidine Residues *Journal of Chromatography A* **1987**, *411*, 177-184.

(67) Stora, T.; Hovius, R.; Dienes, Z.; Pachoud, M.; Vogel, H. Metal Ion Trace Detection by a Chelator-Modified Gold Electrode: A Comparison of Surface to Bulk Affinity *Langmuir* **1997**, *13*, 5211-5214.

(68) Körner, A.; Deichmann, C.; Rossetti, F. F.; Köhler, A.; Konovalov, O. V.; Wedlich, D.; Tanaka, M. Cell Differentiation of Pluripotent Tissue Sheets Immobilized on Supported Membranes Displaying Cadherin-11 *PLoS One* **2013**, *8*, 12.

(69) Pokutta, S.; Herrenknecht, K.; Kemler, R.; Engel, J. Conformational Changes of the Recombinant Extracellular Domain of E-Cadherin Upon Calcium Binding *Eur. J. Biochem.* **1994**, *223*, 1019-26.

(70) Patel, S. D.; Ciatto, C.; Chen, C. P.; Bahna, F.; Rajebhosale, M.; Arkus, N.; Schieren, I.; Jessell, T. M.; Honig, B.; Price, S. R.; Shapiro, L. Type Ii Cadherin Ectodomain Structures: Implications for Classical Cadherin Specificity *Cell* **2006**, *124*, 1255-68.

(71) Daniels, D. S.; Mol, C. D.; Arvai, A. S.; Kanugula, S.; Pegg, A. E.; Tainer, J. A. Active and Alkylated Human Agt Structures: A Novel Zinc Site, Inhibitor and Extrahelical Base Binding *EMBO J* **2000**, *19*, 1719-1730.

(72) Seitz, P. C.; Reif, M. D.; Konovalov, O. V.; Jordan, R.; Tanaka, M. Modulation of Substrate-Membrane Interactions by Linear Poly(2-Methyl-2-Oxazoline) Spacers Revealed by X-Ray Reflectivity and Ellipsometry *Chemphyschem* **2009**, *10*, 2876-2883.

(73) Marra, J.; Israelachvili, J. Direct Measurements of Forces between Phosphatidylcholine and Phosphatidylethanolamine Bilayers in Aqueous Electrolyte Solutions *Biochemistry* **1985**, *24*, 4608-4618.

(74) Marsh, D. *Crc Handbook of Lipid Bilayers*, 1990.

(75) Marsh, D. Polarity and Permeation Profiles in Lipid Membranes *Proceedings of the National Academy of Sciences of the United States of America* **2001**, *98*, 7777-7782.

(76) Sackmann, E. *Biological Membranes Architecture and Function*, 1995.

(77) Medina, A.; Reintsch, W.; Steinbeisser, H. Xenopus Frizzled 7 Can Act in Canonical and Non-Canonical Wnt Signaling Pathways: Implications on Early Patterning and Morphogenesis *Mech Dev* **2000**, *92*, 227-37.

(78) Medina, A.; Steinbeisser, H. Interaction of Frizzled 7 and Dishevelled in Xenopus *Dev Dyn* **2000**, *218*, 671-80.

(79) Swain, R. K.; Medina, A.; Steinbeisser, H. Functional Analysis of the Xenopus Frizzled 7 Protein Domains Using Chimeric Receptors *Int J Dev Biol* **2001**, *45*, 259-64.

(80) Abu-Elmagd, M.; Garcia-Morales, C.; Wheeler, G. N. Frizzled7 Mediates Canonical Wnt Signaling in Neural Crest Induction *Dev Biol* **2006**, *298*, 285-98.

(81) Nieto, M. A.; Sargent, M. G.; Wilkinson, D. G.; Cooke, J. Control of Cell Behavior During Vertebrate Development by Slug, a Zinc Finger Gene *Science* **1994**, *264*, 835-9.

(82) Vallin, J.; Thuret, R.; Giacomello, E.; Faraldo, M. M.; Thiery, J. P.; Broders, F. Cloning and Characterization of Three Xenopus Slug Promoters Reveal Direct Regulation by Lef/Beta-Catenin Signaling *Journal of Biological Chemistry* **2001**, *276*, 30350-30358.

(83) Morgan, M. J.; Woltering, J. M.; Rieden, P.; Durston, A. J.; Thiery, J. P. Yy1 Regulates the Neural Crest-Associated Slug Gene in Xenopus Laevis *Journal of Biological Chemistry* **2004**, *279*, 46826-46834.

(84) Albersdörfer, A.; Feder, T.; Sackmann, E. Adhesion-Induced Domain Formation by Interplay of Long-Range Repulsion and Short-Range Attraction Force: A Model Membrane Study *Biophysical Journal* **1997**, *73*, 245-257.
(85) Bruinsma, R.; Sackmann, E. Bioadhesion and the Dewetting Transition *Comptes Rendus De L Academie Des Sciences Serie Iv Physique Astrophysique* **2001**, *2*, 803-815.
(86) Becker, S. F.; Langhe, R.; Huang, C.; Wedlich, D.; Kashef, J. Giving the Right Tug for Migration: Cadherins in Tissue Movements *Archives of Biochemistry and Biophysics*, *524*, 30-42.
(87) Brochard-Wyart, F.; de Gennes, P. G. Adhesion Induced by Mobile Binders: Dynamics *Proceedings of the National Academy of Sciences of the United States of America* **2002**, *99*, 7854-7859.
(88) Bruinsma, R.; Behrisch, A.; Sackmann, E. Adhesive Switching of Membranes: Experiment and Theory *Physical Review E* **2000**, *61*, 4253-4267.
(89) Martel, L.; Johnson, C.; Boutet, S.; Al-Kurdi, R.; Konovalov, O.; Robinson, I.; Leckband, D.; Legrand, J. F. X-Ray Reflectivity Investigations of Two-Dimensional Assemblies of C-Cadherins: First Steps in Structural and Functional Studies *Journal De Physique Iv* **2002**, *12*, 365-377.
(90) Leckband, D.; Prakasam, A. In *Annual Review of Biomedical Engineering* 2006; Vol. 8, p 259-287.
(91) Kuriyama, S.; Mayor, R. Molecular Analysis of Neural Crest Migration *Philos. Trans. R. Soc. B-Biol. Sci.* **2008**, *363*, 1349-1362.
(92) Brieher, W. M.; Gumbiner, B. M. Regulation of C-Cadherin Function During Activin Induced Morphogenesis of Xenopus Animal Caps *Journal of Cell Biology* **1994**, *126*, 519-527.
(93) Vallin, J.; Thuret, R.; Giacomello, E.; Faraldo, M. M.; Thiery, J. P.; Broders, F. Cloning and Characterization of Three *Xenopus* Slug Promoters Reveal Direct Regulation by Lef/ß-Catenin Signaling *J. Biol. Chem.* **2001**, *276*, 30350-30358.
(94) Mayor, R.; Morgan, R.; Sargent, M. G. Induction of the Prospective Neural Crest of Xenopus *Development* **1995**, *121*, 767-777.
(95) Müller, H. A. J.; Kühl, M.; Finnemann, S.; Schneider, S.; van der Poel, S. Z.; Hausen, P.; Wedlich, D. Xenopus Cadherins: The Maternal Pool Comprises Distinguishable Members of the Family *Mech. Dev.* **1994**, *47*, 213-223.
(96) Tao, Q.; Nandadasa, S.; McCrea, P. D.; Heasman, J.; Wylie, C. G-Protein-Coupled Signals Control Cortical Actin Assembly by Controlling Cadherin Expression in the Early Xenopus Embryo *Development* **2007**, *134*, 2651-61.
(97) Herzberg, F.; Wildermuth, V.; Wedlich, D. Expression of Xbcad, a Novel Cadherin, During Oogenesis and Early Development of Xenopus *Mech. Dev.* **1991**, *35*, 33-42.
(98) Borchers, A.; David, R.; Wedlich, D. *Xenopus* Cadherin-11 Restrains Cranial Neural Crest Migration and Influences Neural Crest Specification *Development* **2001**, *128*, 3049-60.
(99) Theveneau, E.; Marchant, L.; Kuriyama, S.; Gull, M.; Moepps, B.; Parsons, M.; Mayor, R. Collective Chemotaxis Requires Contact-Dependent Cell Polarity *Dev. Cell* **2010**, *19*, 39-53.
(100) Kashef, J.; Köhler, A.; Kuriyama, S.; Alfandari, D.; Mayor, R.; Wedlich, D. Cadherin-11 Regulates Protrusive Activity in *Xenopus* Cranial Neural Crest Cells Upstream of Trio and the Small Gtpases *Genes Dev.* **2009**, *23*, 1393-8.
(101) Crick, F. Diffusion in Embryogenesis *Nature (London)* **1970**, *225*, 420-422.
(102) Driever, W.; Nusslein-Volhard, C. A Gradient of Bicoid Protein in Drosophila Embryos *Cell* **1988**, *54*, 83-93.

(103) Fenz, S. F.; Merkel, R.; Sengupta, K. Diffusion and Intermembrane Distance: Case Study of Avidin and E-Cadherin Mediated Adhesion *Langmuir* **2009**, *25*, 1074-85.
(104) Horton, M. R.; Reich, C.; Gast, A. P.; Radler, J. O.; Nickel, B. Structure and Dynamics of Crystalline Protein Layers Bound to Supported Lipid Bilayers *Langmuir* **2007**, *23*, 6263-9.
(105) Groves, J. T.; Boxer, S. G.; McConnel, H. M. Electric Field-Induced Reorganization of Two-Component Supported Bilayer Membranes *Proceedings of the National Academy of Sciences of the United States of America* **1997**, *94*, 13390-13395.
(106) Monson, C. F.; Pace, H. P.; Liu, C.; Cremer, P. S. Supported Bilayer Electrophoresis under Controlled Buffer Conditions *Anal. Chem.* **2011**, *83*, 2090-2096.
(107) Han, X.; Cheetham, M. R.; Sheikh, K.; Olmsted, P. D.; Bushby, R. J.; Evans, S. D. Manipulation and Charge Determination of Proteins in Photopatterned Solid Supported Bilayers *Integrative Biology* **2009**, *1*, 205-211.
(108) Sivasankar, S.; Subramaniam, S.; Leckband, D. Direct Molecular Level Measurements of the Electrostatic Properties of a Protein Surface *Proceedings of the National Academy of Sciences of the United States of America* **1998**, *95*, 12961-12966.
(109) Groves, J. T.; Boxer, S. G. Electric Field-Induced Concentration Gradients in Planar Supported Bilayers *Biophysical Journal* **1995**, *69*, 1972-1975.